ABSTRACT

VALLABHUNENI, SRAVANTHI. Slippery Surfaces: Design & Applications. (Under the direction of Dr. Arun K. Kota).

Slippery surfaces (i.e., surfaces that display high mobility with liquid droplets) have gained significant attention for their advantages in a wide variety of applications like self-cleaning, drag reduction, enhanced condensation, fouling resistance, biomedical implants etc. Slippery surfaces can be broadly classified as: i) textured slippery surfaces, wherein the underlying substrate is rough (both surface texture and surface chemistry play a critical role in obtaining slipperiness); and ii) non-textured slippery surfaces, wherein the underlying substrate is non-textured (surface homogeneity plays a critical role in obtaining slipperiness). Depending on wettability (i.e., hydrophilicity or hydrophobicity), slippery surfaces can prove to be extremely beneficial for specific practical applications. In this work, we delve into the design principles of slippery surfaces and emphasize their potential for various applications relevant to thermofluidics and biofluidics. Utilizing textured slippery surfaces (i.e., superomniphobic surfaces), we demonstrated: i) on-demand, remote and lossless manipulation of biofluidic droplets by developing biofluid manipulators for minimizing the risk of exposure to healthcare workers and clinical laboratory personnel. Using our biofluid manipulators, first, we demonstrated in-plane (simultaneous and sequential) transport and mixing of liquid droplets, as well as out-of-plane grip, transport, and release of liquid droplets and later, highlighted their potential for colorimetric assays and blood coagulation assays by manipulating biofluids, including blood and virus; and ii) enhanced chemical shielding on soft robots for retaining their functionality and performance under corrosive liquid environments. Using our superomniphobic coatings, first, we demonstrated excellent chemical resistance with corrosive acids and solvents. Later, we highlighted the practical utility of superomniphobic soft robots by fabricating soft

pneumatic robots (gripper, fish, and jellyfish) and liquid crystal elastomeric and magnetic actuators and showing no surface damage while functioning in acidic environments or in the presence of solvents. In relevance with non-textured slippery surfaces, we designed a novel class of slippery hydrophilic (SLIC) surfaces and elucidated the underlying physics for slipperiness. Utilizing SLIC surfaces, first, we demonstrated their excellent performance in condensation heat transfer highlighting their potential for thermofluidic applications. Second, we demonstrated their exceptional fouling resistance highlighting their practical utility for novel open miniaturized fouling-free lab-on-a-chip platforms. Third, we investigated the interaction of blood components (fibrinogen, platelets & leukocytes) on SLIC surfaces by studying fibrinogen adsorption and platelet & leukocyte adhesion to demonstrate their potential for blood-contacting medical devices. Overall, our insights from the fundamental design principles of slippery surfaces and their applications will have significant implications in multiple fields ranging from thermofluidics to biofluidics.

© Copyright 2023 by Sravanthi Vallabhuneni

All Rights Reserved

Slippery Surfaces: Design & Applications

by
Sravanthi Vallabhuneni

A dissertation submitted to the Graduate Faculty of
North Carolina State University
in partial fulfillment of the
requirements for the degree of
Doctor of Philosophy

Mechanical Engineering

Raleigh, North Carolina
2023

APPROVED BY:

_____	_____
Dr. Arun K. Kota Committee Chair	Dr. Jie Yin
_____	_____
Dr. Marie Muller	Dr. Ashley Brown

DEDICATION

To my beloved father, Mr. Yanadi Rao,

who has been my inspiration and motivation in pursuing my passion for science.

He has always been my role model and the only reason for all my accomplishments.

Thank you, nanna, for being the best father I could ever ask for!

BIOGRAPHY

Sravanthi Vallabhuneni was born in Andhra Pradesh, India and acquired her bachelor's degree in mechanical engineering from Andhra University, Visakhapatnam, India in 2013. In 2015, she moved to the USA and acquired her master's degree in mechanical engineering from Colorado State University. During her masters, she worked on her thesis titled 'Superhydrophobic coatings for electrical insulators', under the guidance of Dr. Arun K. Kota. After graduation, she moved to North Carolina with the Kota research group and continued her research on wetting & adhesion towards her PhD degree in mechanical engineering at North Carolina State University. Her research primarily focuses on designing surface coatings for various thermofluidic and biofluidic applications like condensation heat transfer, lossless droplet manipulation, chemical shielding, anti-fouling, lab-on-a-chip platforms etc.

ACKNOWLEDGMENTS

First and foremost, I would like to express my heartfelt gratitude to my advisor, Dr. Arun K. Kota, for his exceptional guidance and support throughout my doctoral journey. His expertise, unwavering support and constructive criticism have been instrumental in shaping my dissertation. His patience, understanding and compassion were pivotal in the ups and downs of this journey.

I would like to thank the exceptional members of my committee - Dr. Jie Yin, Dr. Marie Muller, and Dr. Ashley Brown, for their invaluable insights, expertise, and feedback, which have been critical in improving the quality of my dissertation.

I extend my sincere appreciation to Dr. Hamed Vahabi, Dr. Wei Wang, Dr. Yinding Chi, Dr. Kimberly Nellenbach and Dr. Roberta Maia Sabino, for their assistance with my experiments and for the prolonged discussions about my results, which were crucial in completing my work.

I would like to express my appreciation to all the members of Kota research group for their invaluable assistance and camaraderie, which helped me develop my research skills.

I would like to express my appreciation to all the staff at North Carolina State University, for their timely and efficient assistance with the necessary resources to carry out my research.

Finally, I am immensely grateful to my dearest family and friends for their unconditional love and support, which has been a constant source of strength for me through both personal and professional successes and setbacks.

TABLE OF CONTENTS

LIST OF TABLES

LIST OF FIGURES

OVERVIEW

Slippery surfaces are surfaces that display high mobility with liquid droplets. Such surfaces have gained significant attention for their advantages in a wide variety of applications like self-cleaning, drag reduction, enhanced condensation, fouling resistance, biomedical implants etc.[1,2] This is because slippery surfaces enable easy droplet sliding (i.e., high droplet mobility) due to low surface adhesion, which is highly desirable in several applications in thermofluidics and biofluidics. For example, in condensation heat transfer, slipperiness is essential for condensate removal to expose the underlying solid surface for further nucleation. This facilitates sustainable dropwise condensation resulting in enhanced condensation heat transfer.[3,4] As another example, slippery surfaces are exceptional for self-cleaning applications.[1] This is because when liquid droplets impinge on a slippery surface with contamination or dirt, they roll-off/slide past the surface carrying the contamination or dirt from the surface leaving it clean. Yet another example, slippery surfaces are extremely useful for marine applications such as boat hulls and submarines. In marine applications, slippery surfaces reduce skin friction (i.e., liquid drag) and consequently, increase fuel efficiency.[5,6] Slippery surfaces can also prevent fouling (i.e., buildup of algae and other marine organisms), which further helps in the speed and maneuverability of the structure. This is also applicable to biomedical implants and other medical devices (e.g., stents, catheters, blood storage containers etc.), where biofouling (i.e., adsorption of blood proteins and adhesion of blood and blood components) is highly undesirable.[7,8]

Slippery surfaces can be broadly classified as: i) textured slippery surfaces, wherein the underlying substrate is rough (both surface texture and surface chemistry play a critical role in slipperiness); and ii) non-textured slippery surfaces, wherein the underlying substrate is non-

textured (surface homogeneity plays a critical role in slipperiness). In this dissertation, we delve into the design principles of such textured and non-textured slippery surfaces and emphasize their potential in multiple applications of thermofluidics and biofluidics.

In chapter 1, we review the fundamentals of wettability and slipperiness on solid surfaces. We also discuss the design criteria for obtaining slipperiness using textured and non-textured surfaces. In chapter 2, we discuss the application of textured slippery surfaces for on-demand, remote, and lossless manipulation of biofluids, which can potentially reduce manual operations and minimize exposure time to infectious biofluids and consequently, minimizing their risk of exposure to clinical laboratory personnel and healthcare workers. In chapter 3, we discuss the potential of textured slippery surfaces in the chemical shielding of soft robots to retain their functionality and performance under corrosive liquid (e.g., acids, bases, solvents etc.) environments. In chapter 4, we discuss the design principles of an emerging class of slippery hydrophilic (SLIC) surfaces and demonstrate their potential for relevant applications in thermofluidics and biofluidics. In chapter 5, building on our prior work on SLIC surfaces, we discuss the fabrication of slippery surfaces using polymeric substrates (silicone rubber, polyurethane, polycarbonate) and investigate the interaction of blood with such surfaces for developing fouling resistant biomedical devices. In chapter 6, we discuss the contributions of our work to fundamental science and applied science and emphasize their prospects and implications in thermofluidic and biofluidic applications.

CHAPTER 1. FUNDAMENTALS OF WETTING AND SLIPPERINESS

1.1 Introduction

Slippery surfaces (i.e., surfaces that display high mobility with liquid droplets) have gained significant attention for their advantages in a wide variety of applications like self-cleaning, drag reduction, enhanced condensation, fouling resistance, biomedical implants etc.[1,2] This is because slippery surfaces enable easy droplet sliding (i.e., high droplet mobility) due to low surface adhesion, which is highly desirable in several applications in thermofluidics and biofluidics. Depending on the surface wettability (i.e., hydrophilicity or hydrophobicity), slippery surfaces can prove to be extremely beneficial in specific practical applications. For example, in condensation heat transfer, slippery hydrophilic surfaces display higher efficiency with aqueous liquids because the hydrophilicity enables higher droplet nucleation and slipperiness enables quick condensate remove facilitating sustained dropwise condensation. However, slippery hydrophilic surfaces are not slippery towards non-aqueous low surface tension liquids (e.g., solvents and hydrocarbon oils like hexadecane) and are inefficient in condensation heat transfer with such low surface tension oils. For condensation heat transfer with low surface tension oils, slippery oleophilic surfaces (which are typically hydrophobic) can render high efficiency. In this chapter, we review the fundamentals of wettability and slipperiness and discuss the underlying principles for designing slippery surfaces (textured and non-textured). Utilizing these design principles, we discuss the fabrication of slippery surfaces and emphasize their potential for several practical applications in the following chapters.

1.2 Contact angle

The primary measure of wetting of a liquid droplet on a non-textured (i.e., smooth) solid surface (see Fig. 1.1) is the Young's contact angle θ_Y, given by Young's equation:[9]

$$\cos\theta_Y = \frac{\gamma_{sv} - \gamma_{sl}}{\gamma_{lv}} \tag{1.1}$$

Here, γ_{sv}, γ_{sl} and γ_{lv} are the solid surface energy, the solid-liquid interfacial tension, and the liquid surface tension, respectively. Typically, a solid surface is classified as hydrophilic, when it displays θ_Y < 90° and hydrophobic, when θ_Y > 90° with water. Similarly, a solid surface is classified as oleophilic, when it displays θ_Y < 90° and oleophobic, when θ_Y > 90° with oils.

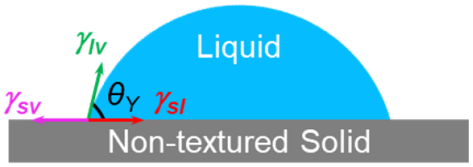

Figure 1.1. Young's contact angle. A Schematic depicting the Young's contact angle θ_Y displayed by a liquid droplet on a non-textured solid.

As evident from Eq. 1.1, Young's contact angle θ_Y increases with increasing liquid surface tension γ_{lv} and decreases with increasing solid surface energy γ_{sv}. This implies that liquids with high surface tension γ_{lv} (e.g., water) will display higher θ_Y and surface chemistries with low solid surface energy γ_{sv} (e.g., fluorocarbons and hydrocarbons) will display higher θ_Y.

1.3 Contact angle on a textured solid

When a liquid droplet contacts a textured solid surface, it displays an apparent contact angle θ^*. Apparent contact angle θ^* depends on the two configurations a liquid droplet can adopt on a textured solid: i) the Wenzel state[10] and ii) the Cassie-Baxter state[11]. In the Wenzel state, the liquid completely wets the solid surface (see Fig. 1.2a), whereas in the Cassie-Baxter state, the texture traps air pockets resulting in a composite solid-liquid and liquid-air interface (see Fig. 1.2b). Cassie-Baxter state is preferred to obtain high apparent contact angles θ^*.

In the Cassie-Baxter state, the apparent contact angle θ^* displayed by a liquid is a weighted-average between θ_Y (i.e., local contact angle displayed by the liquid) and π (i.e.,

contact angle displayed by the liquid in air). The apparent contact angle θ^* is calculated using Cassie-Baxter relation:[11]

$$\cos\theta^* = f_{sl}\cos\theta_Y + f_{lv}\cos\pi \tag{1.2}$$

Here, f_{sl} and f_{lv} refer to area fractions of solid-liquid interface and liquid-air interface, respectively, below the liquid droplet. As evident from Eq 1.2, larger area fraction of liquid-air interface f_{lv} will result in higher apparent contact angles θ^*.

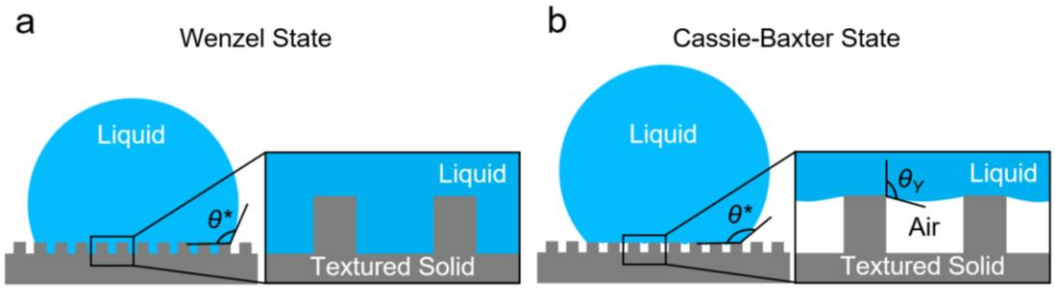

Figure 1.2. Droplet configurations on a textured solid. (a) & (b) Schematics depicting liquid droplets in Wenzel state and Cassie-Baxter state, respectively, on a textured solid surface.

1.4 Contact angle hysteresis

The primary measure of slipperiness on a solid surface is contact angle hysteresis $\Delta\theta$, which is defined as the difference between the advancing contact angle θ_{adv} and the receding contact angle θ_{rec} displayed by a liquid droplet.[6,12] Advancing contact angle θ_{adv} is the maximum contact angle and receding contact angle θ_{rec} is the minimum contact angle displayed by a liquid droplet at the advancing and trailing edges, respectively, while sliding past a solid surface (see Fig. 1.3).

Contact angle hysteresis $\Delta\theta$ arises from the physical inhomogeneities (i.e., surface roughness) and chemical inhomogeneities (i.e., non-uniformity in surface chemistry) on a solid surface.[6,13,14] Typically, a smooth solid surface (e.g., polished silicon wafers) displays low physical inhomogeneity and a surface with uniform surface chemistry displays low chemical

inhomogeneity. Physically, contact angle hysteresis $\Delta\theta$ indicates the energy dissipated by a liquid droplet while sliding on a solid surface.[15-17] Low contact angle hysteresis $\Delta\theta$ indicates low adhesion between the liquid and solid, which further results in high mobility of liquid droplets on a solid surface.

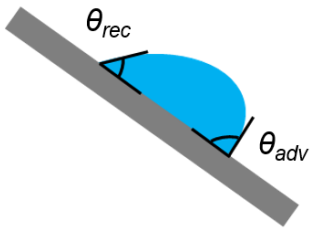

Figure 1.3. Advancing and receding contact angles. A schematic depicting the advancing contact angle and the receding contact angle displayed by a liquid droplet (blue) while sliding on a tilted solid surface.

1.5 Roll-off/Sliding angle

Another measure of slipperiness on a solid surface is roll-off/sliding angle ω, which is defined as the minimum tilt angle of a solid surface relative to horizontal required for a liquid droplet to start sliding or rolling off on a solid surface (see Fig. 1.4). The roll-off or sliding angle can be estimated by balancing work done in adhesion against the work done under gravity using Furmidge relation as:[18]

$$\sin\omega = \frac{\gamma_{lv} w(\cos\theta_{rec} - \cos\theta_{adv})}{\rho g V} \tag{1.3}$$

Here, ω is the roll-off/sliding angle, γ_{lv} is the liquid surface tension, w is the width of a liquid droplet at triple-phase contact line perpendicular to its motion, θ_{rec} is the receding contact angle, θ_{adv} is the advancing contact angle, ρ is the density of the liquid, g is the acceleration due to gravity, and V is the volume of the liquid droplet. As evident from Eq. 1.3, low contact angle

hysteresis (i.e., low $\Delta\theta$) results in low roll-off/sliding angles (i.e., low ω), which further enables high mobility of liquid droplets on a solid surface.

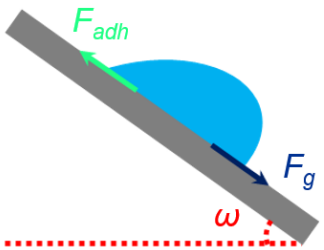

Figure 1.4. Roll-off/sliding angle. A schematic depicting the roll-off/sliding angle of a liquid droplet (blue) on a solid surface. Here, F_{adh} and F_g refer to the adhesion force and the gravitational force, respectively.

1.6 Slipperiness on textured surfaces

In the past two decades, textured slippery surfaces have been fabricated using two approaches, both of which rely on fluid-film lubrication.[19] The first approach employs super-repellent surfaces, which use texture to trap air pockets at the solid-liquid interface, reducing the solid-liquid interfacial area and inducing slip at the liquid-air interface.[20] The second approach employs lubricant-infused surfaces, which use texture to trap pockets of a liquid (immiscible with the contacting liquids) on the solid surface, reducing the solid-liquid interfacial area and inducing slip at the liquid-liquid interface.[21] In this dissertation, we primarily focus on super-repellent surfaces and their applications for lossless droplet manipulation and enhancing chemical resistance of soft robots.

Super-repellent surfaces can be broadly classified as superhydrophobic and superomniphobic. A surface is considered superhydrophobic if it displays extreme repellency towards high surface tension liquids like water, whereas a surface is considered superomniphobic if it displays extreme repellency towards virtually any liquid, irrespective of surface tension,

viscosity, polarity, pH, etc. Typically, super-repellent surfaces display apparent contact angles θ^* > 150° and contact angle hysteresis $\Delta\theta$ < 10° or roll-off angles ω < 10°.[6,12] Superhydrophobic surfaces can be fabricated by imparting low solid surface energy with surface texture that can result in the Cassie-Baxter state with high liquid-air interfacial area. However, superomniphobic surfaces require a special texture called re-entrant texture (see Fig. 1.5) to maintain the Cassie-Baxter state, especially with low surface tension liquids (e.g., hydrocarbon oils like hexadecane). Typically, re-entrant textures consist of convex textures like inverse trapezoids, or features with undercuts or overhangs (see Fig. 1.5). For example, surface textures obtained by coating with spherical particles and non-spherical particles with undercuts or overhangs can offer re-entrant texture; when such surface textures are imparted solid surface energy via fluorocarbon surface chemistries, they can render the surface superomniphobic (explained in-detail in the following chapters).

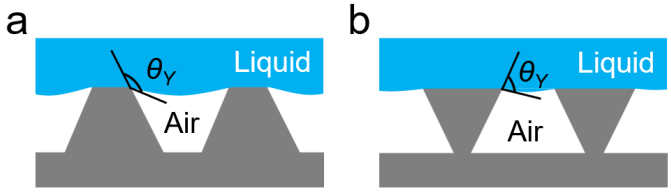

Figure 1.5. Cassie-Baxter state with high & low surface tension liquids. (a) & (b) Schematics depicting Cassie-Baxter state with high surface tension liquid (θ_Y > 90°) without re-entrant texture and with low surface tension liquid (θ_Y < 90°) with re-entrant texture, respectively, on a surface with low solid surface energy.

1.7 Slipperiness on non-textured surfaces

Despite the appeal of the textured slippery surfaces (i.e., super-repellent surfaces & lubricant-infused surfaces), they are prone to lose slipperiness due to damage of texture, depletion of air via dissolution or external pressure, or depletion of lubricant via evaporation or

repeated use.[22,23] Non-textured (i.e., smooth), all-solid, slippery surfaces mitigate such texture-related concerns with textured slippery surfaces. Non-textured, all-solid slippery surfaces can be fabricated by covalently grafting brushes (i.e., tethering oligomers or polymers to surfaces) at a sufficiently high grafting density σ on to smooth solid surfaces (see Fig. 1.6).

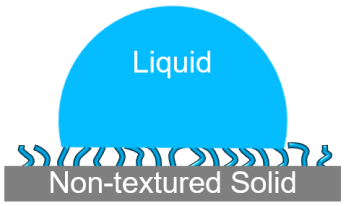

Figure 1.6. Non-textured slippery surface. A schematic depicting a liquid droplet on a smooth solid surface covalently grafted with oligomeric brushes (blue).

Non-textured and all-solid surfaces can display slipperiness when contact angle hysteresis $\Delta\theta$ (i.e., the difference between advancing contact angle θ_{adv} and receding contact angle θ_{rec}) is low. Low contact angle hysteresis $\Delta\theta$ can be achieved when a surface has low physical and chemical inhomogeneities. Non-textured surfaces with very low surface roughness (e.g., silicon wafers and glass coverslips) display low physical inhomogeneity. High grafting density σ leads to low chemical inhomogeneity. However, most non-textured, all-solid, slippery surfaces are hydrophobic. Non-textured, all-solid, slippery hydrophilic (SLIC) surfaces are rare and challenging to fabricate. In our work, we focus on elucidating the design principles of an emerging class of SLIC surfaces and their potential for thermofluidic and biofluidic applications in the following chapters.

CHAPTER 2. ON-DEMAND, REMOTE AND LOSSLESS MANIPULATION OF BIOFLUID DROPLETS

2.1 Introduction

Exposure to infectious agents (e.g., pathogens like bacteria, viruses etc.) present in non-Newtonian or active biofluids (e.g., blood, saliva, urine etc.) poses a severe risk to clinical laboratory personnel and healthcare workers,[24-26] resulting in hundreds of millions of hospital-acquired and laboratory-acquired infections each year.[24,27-29] The recent global outbreaks of epidemics and pandemics (e.g., HIV/AIDS, MERS-CoV, Ebola, SARS-CoV-2 etc.) and the increased exposure of clinical laboratory personnel and healthcare workers to the highly infectious specimens, further emphasizes this risk. Novel technologies that can mitigate such risk by reducing manual operations and minimizing exposure time through remote and automated handling of infectious biofluids are indispensable.[30,31]

In this work, we present biofluid manipulators, which allow on-demand, remote and lossless manipulation of a wide range of liquids, including biofluids (e.g., blood). Our biofluid manipulators are designed by integrating thermo-responsive soft actuators with superomniphobic surfaces (i.e., surfaces that are extremely repellent to virtually all liquids) through a simple and versatile multi-layer design. While prior reports have engineered soft manipulators that can maneuver solid objects,[32-34] there are no reports of soft manipulators that can maneuver biofluid droplets. Furthermore, while there are several reports on droplet manipulation methods (e.g., electric fields, magnetic fields, light, heat, sound, guiding tracks, and surface patterning),[35-41] they suffer from one or more of the following shortcomings – liquid loss or single-use or in-plane movement only or expensive fabrication or non-portable or not on-demand. For example, electric field induced droplet manipulation (e.g., electrowetting based) techniques suffer from

expensive fabrication costs/methods (e.g., photolithography) and liquid losses, and do not allow out-of-plane droplet manipulation.[42,43] Magnetic field induced droplet manipulation techniques suffer from expensive fabrication costs/methods (e.g., photolithography) or liquid losses or dispersion of magnetic particles in the liquid that can result in contamination.[44,45] Light induced droplet manipulation techniques suffer from liquid losses and do not allow out-of-plane droplet motion.[46,47] Heat induced droplet manipulation techniques can damage biofluids and suffer from liquid losses.[36,48] Sound based techniques like acoustic tweezers suffer from expensive fabrication/methods (e.g., photolithography and complex transducer arrays) or low spatial resolution and/or require skilled labor.[41,49] Surface patterning-based droplet manipulation techniques suffer from expensive fabrication costs/methods (e.g., photolithography), liquid losses and do not allow on-demand manipulation.[37,38]

Utilizing our biofluid manipulators, we overcome these shortcomings and demonstrate in-plane (simultaneous and sequential) transport and mixing of liquid droplets, as well as out-of-plane grip, transport, and release of liquid droplets. While simultaneous in-plane manipulation of droplets enables automation of simple single-step processes, sequential in-plane manipulation enables automation of multi-step processes, which involve sequential mixing of droplets at different time intervals. The out-of-plane manipulation enables automation of more sophisticated processes that require pickup, transport, and release of droplets across hurdles or obstacles on the surface. Furthermore, to illustrate the practical utility of our manipulators, we demonstrate on-demand, remote and lossless manipulation of biofluid droplets, including blood and virus replicons. We envision that our biofluid manipulators will not only reduce manual operations and minimize exposure to infectious agents, but also pave the way for developing inexpensive,

simple, and portable robotic systems, which can allow point-of-care operations, particularly in developing nations.

2.2 Biofluid manipulators for on-demand and remote manipulation

To achieve on-demand and remote manipulation of liquid droplets, we fabricated manipulators by embedding a heterochiral twisted and coiled actuator (TCA)[50-52] between softer and stiffer elastomer layers. We used a heterochiral TCA because it can be easily fabricated with commercially available materials, it can be remotely actuated (i.e., elongated due to thermally induced untwisting) on-demand by Joule heating with a low voltage (< 5 V), it does not require additional bulky hardware, and it generates appreciable and reversible elongation,[50] which can generate considerable forces (about 100 times larger than a human muscle of same mass and length).[51]

2.2.1 Fabrication of heterochiral twisted-and-coiled actuators (TCAs)

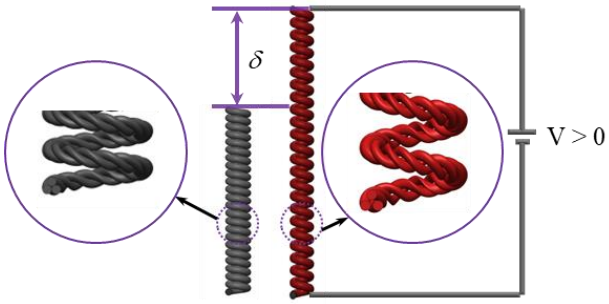

Figure 2.1. Twisted and coiled actuator (TCA). A Schematic illustrating the elongation of a TCA (δ) by applying a voltage (V > 0).

We fabricated heterochiral TCAs using silver coated nylon sewing threads (Shieldex Trading, 235/35 4ply). Two nylon threads were first twisted together by generating twists from one end of the thread with a step motor, while exerting a load of 380 g on the other end of the thread. The twisted nylon threads were then coiled around a copper wire with a diameter of 0.4 mm using a custom-built apparatus. The opposite directions of coiling and twisting resulted in

the heterochiral TCAs. Subsequently, the TCAs were annealed at 180°C for 1 hour in an oven (Quincy Lab, 10GCE) to stabilize the structure of the TCAs. The copper wire was removed after the TCAs were cooled down to room temperature. By applying a voltage remotely, the TCA can display elongation reversibly due to thermal expansion and untwisting of the thread coils (see Fig. 2.1).

2.2.2 Fabrication of biofluid manipulators

A TCA arranged in a U shape (for droplet gripper and sequential droplet manipulation) or an elliptical shape (for simultaneous droplet manipulation) was sandwiched between two layers of soft adhesive tape (3M Inc., VHB tape 4905). To create asymmetric stiffness, a soft elastomer layer fabricated by folding a self-fusing silicone tape (Loctite Inc., Go2 wrap) was attached to one side of the soft body. The two ends of the TCA were connected to copper wires that acted as electrical leads.

Figure 2.2. Biofluid manipulator. (a) Schematic illustrating the fabrication of soft manipulator by embedding a single heterochiral TCA between softer and stiffer elastomer layers. (b) Schematic illustrating the fabrication of soft manipulator after embedding a single heterochiral TCA between softer and stiffer elastomer layers. (c) & (d) Pictures showing the bending of the soft manipulator when a voltage is applied.

We embedded a single heterochiral TCA (with a U shape) between a softer elastomer layer consisting of just a soft adhesive tape (Young's modulus of ~104 kPa) and a stiffer

elastomer layer consisting of the soft adhesive tape along with a stiffer tape (Young's modulus of ~338 kPa; see Fig. 2.2a and b). We used softer and stiffer elastomer layers because the softer side exhibits larger elongation than the stiffer side upon actuation (i.e., Joule heating with a voltage) of the heterochiral TCA. In order to accommodate this asymmetric elongation, the soft manipulator bends toward the stiffer side (see Fig. 2.2c & d). Our soft manipulator can reversibly bend with large bending angles and recover quickly.

2.2.3 Characterization of biofluid manipulators

We characterized the actuation of biofluid manipulators by measuring the output blocking force F_b (i.e., the force required to restrict further bending)[53-55] of the actuated soft manipulator. The blocking force generated by the manipulator at each bending curvature was measured by placing the probe of a force gauge (M3-012, Mark-10 Inc.) in the bending path of the manipulator. The probe was positioned to ensure that it contacted the tip of the manipulator. Three measurements were performed for each bending curvature.

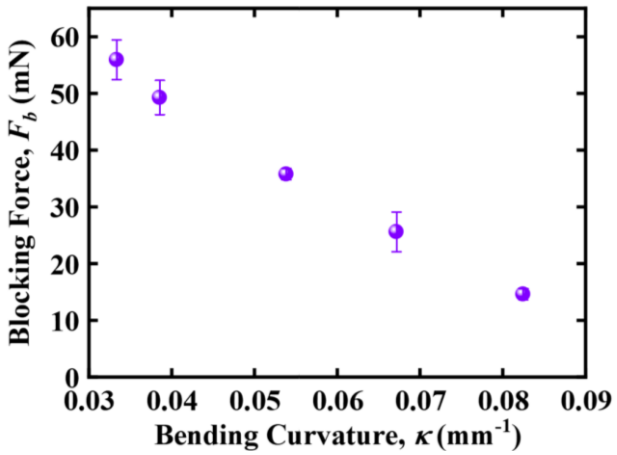

Figure 2.3. Blocking force of soft manipulator. Plot showing the blocking force generated by a soft manipulator at different bending curvatures.

Our results indicate that the blocking force decreases with increasing bending curvature of the actuated soft manipulator (see Fig. 2.3). This is because at larger bending curvatures, the

force generated by the actuated TCA is increasingly used to induce larger elastic deformations. However, even at a large bending curvature of ~0.08 mm^{-1} (which is higher than the bending curvatures used in our experiments), the blocking force of our soft manipulator is ~15 mN (sufficient to lift ~1.5 g of liquid), which is more than an order of magnitude higher than the force required for handling millimeter-sized droplets of common liquids.

2.3 Lossless droplet manipulation with biofluid manipulators

To design manipulators for lossless manipulation of liquid droplets, the adhesion between the liquid droplet and the surface of the manipulator should be minimized. One strategy for significantly reducing the adhesion is to fabricate manipulators with super-repellent surfaces.[56,57] Super-repellent surfaces are broadly classified as superhydrophobic and superomniphobic. Superhydrophobic surfaces display extreme repellency (i.e., low adhesion) to aqueous liquids,[58] while superomniphobic surfaces display extreme repellency to virtually any liquid (aqueous or organic; acids, bases or solvents; Newtonian or non-Newtonian etc.).[12,20,59-61] Superomniphobic surfaces can be designed by combining materials possessing low solid surface energy with appropriate re-entrant surface texture (i.e., convex or overhang structures).[62-65] While low solid surface energy results in high contact angles, appropriate re-entrant surface texture results in a stable Cassie-Baxter state[11] for a wide range of liquids.[20,63,65] Manipulators with such superomniphobic surfaces can be used for lossless handling of a wide range of liquid droplets, including biofluids.

2.3.1 Superomniphobic biofluid manipulators

We imparted superomniphobicity on our biofluid manipulators by spray-coating fluorinated fumed silica particles on the manipulator surfaces. The fluorinated particles were prepared through liquid phase silanization of 500 mg of 7 nm fumed silica particles (Sigma-

Aldrich) in 20 mL hexane containing 0.5 mL heptadecafluoro-1,1,2,2-tetrahydrodecyl trichlorosilane (Gelest Inc.) for three days. The solution was then spray coated onto the manipulator surfaces using an air brush held at 15 cm from the surface at a pressure of 30 psi. The surfaces were then dried at room temperature before use.

We characterized the surface morphology of our biofluid manipulators using a scanning electron microscope (JEOL JSM-6500F) at 10 kV. The manipulator surfaces were sputter coated with gold/palladium target to make the surface conductive (to avoid charging) for SEM imaging. The spray coated fumed silica particle morphology provided the re-entrant structure (see Fig. 2.4) and the fluorination of these fumed silica particles provided the low solid surface energy, which together rendered the surface superomniphobic.

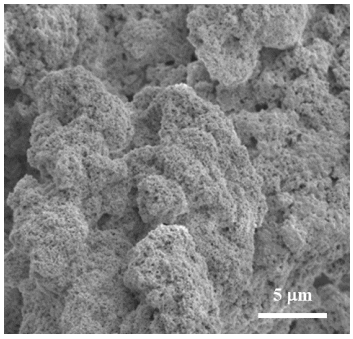

Figure 2.4. Surface morphology. An SEM image displaying the re-entrant morphology of fluorinated silica particles on our superomniphobic surfaces.

We characterized superomniphobicity by measuring the apparent advancing θ^*_{adv} and apparent receding θ^*_{rec} contact angles of a wide range of liquids with surface tensions ranging from 27.5 mN m^{-1} to 72.1 mN m^{-1} (see Fig. 2.5a) using a contact angle goniometer (Ramé-Hart 200-F1). For each liquid, three measurements were performed. All tested liquids displayed apparent contact angles $\theta^* \geq 150°$ and low contact angle hysteresis $\Delta\theta = \theta^*_{adv} - \theta^*_{rec}$ on our superomniphobic surfaces. The low contact angle hysteresis led to high mobility (or low

adhesion) of droplets, as evidenced by the low roll off angles $\omega < 10°$ (see Fig. 2.5b). The ultra-low liquid adhesion was also evident from the complete rebound of droplets upon impacting the superomniphobic surfaces. Our biofluid manipulators can easily handle liquid volumes from 5 μL to 5 mL.

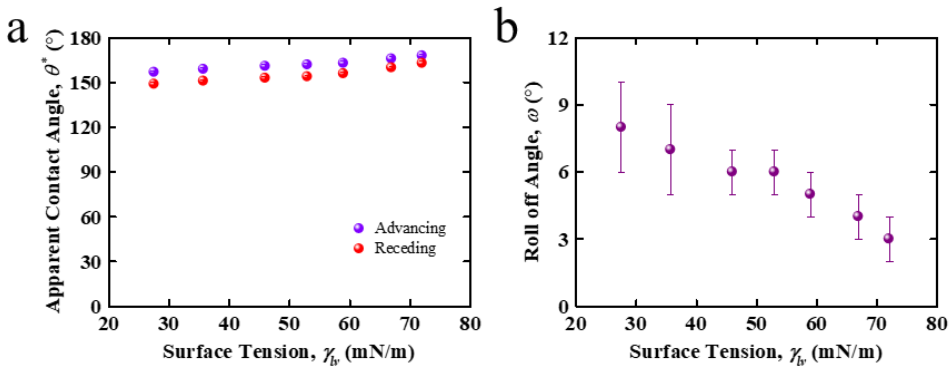

Figure 2.5. Superomniphobicity. (a) & (b) Apparent contact angles and roll off angles, respectively, of liquid droplets with different surface tensions on our superomniphobic surfaces. Roll off angles were measured with 20 μL droplets.

2.3.2 Lossless droplet manipulation

We evaluated the lossless nature of droplet manipulation and cross-contamination on our biofluid manipulators by measuring the droplet volume, actuator mass and droplet roll off angle as a function of the droplet rastering cycles. In order to do this, we prepared multiple liquids (hexadecane, water, Bradford reagent, BSA, milk, virus replicon particle laden solution, thrombin, whole blood, fibrinogen and PRP) and performed droplet rastering on biofluid manipulators.

Bovine serum albumin (BSA) droplets were prepared by diluting BSA (2 mg ml^{-1}; Fisher Scientific) to 2 ng ml^{-1} with water. Virus replicon particle-laden droplets were prepared by suspending virus in 10% fetal bovine serum (FBS) buffer. Instead of using infectious virus, for safety reasons, we chose to use single-cycle infectious virus replicon particles (VRPs). To

produce VRPs, a trans-packaging system for WNV replicons was used. Briefly, a BHK packaging cell line (VEEV-WNV C-E-Pac) harboring a Venezuelan Encephalitis virus replicon expressing the structural coding region of WNV (VEEV-WNV C-E-Pac)[66] was infected with previously produced WNV replicon particles, whose genome contains a deletion in the capsid protein C coding region. These replicon particles are able to infect regular cells, but due to the mutation in the C protein, they are not able to package their genome and produce progeny particles after the initial infection (single cycle infectious particles). However, full-length C protein expressed from VEEV- WNV C-E-Pac in the packaging cell line complements the defective C protein in the WNV replicon, leading to packaging of replicon genomes and secretion of WNV VRPs.[67] VRPs were produced in Dulbecco's Modified Eagle medium (DMEM), supplemented with antibiotics and 10% FBS. Whole blood (porcine) obtained from two-year-old female swine from North Carolina State University's tissue sharing program. Plasma was separated from blood by centrifugation twice at 15,000 g for 15 mins. Thrombin droplets were prepared by diluting thrombin (100 mg mL^{-1}, Enzyme Research Laboratories) to 20 mg mL^{-1}. Fibrinogen droplets were prepared by diluting fibrinogen (20 mg mL^{-1}, Fib3 Fibrinogen with fibronectin, von Willebrand Factor, and Factor XIII depleted, Enzyme Research Laboratories) to 3 mg mL^{-1}.

First, we measured the droplet volume and visually inspected the droplets as a function of droplet rastering cycles, sequentially with multiple liquids (hexadecane, water, Bradford reagent, BSA, milk, virus replicon particle laden solution, thrombin, whole blood, fibrinogen and PRP), on a single biofluid manipulator. In each cycle, a 30 μL pendant droplet of the desired liquid was rastered across the surface of the same biofluid manipulator using a linear translation stage. The droplet appearance was inspected, and the droplet image was captured after every 50 cycles and

analyzed with ImageJ to determine the droplet volume. Even after 1000 droplet rastering cycles with each liquid, sequentially on the same manipulator, there is neither a significant change in the volume of any droplet (see Fig. 2.6a) nor a discernible change in the appearance of any droplet. These results confirm that there is neither liquid loss nor noticeable cross-contamination associated with our droplet manipulations.

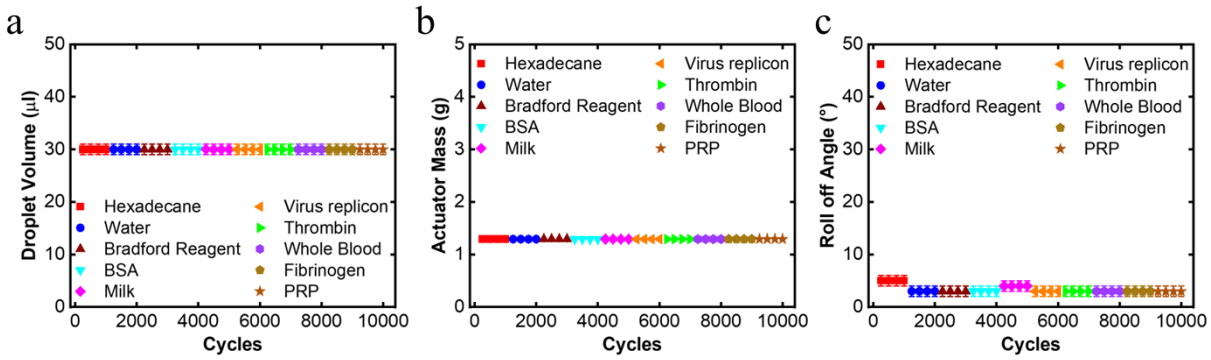

Figure 2.6. Lossless droplet manipulation. (a) Droplet volume as a function of droplet rastering cycles. (b) Actuator mass as a function of droplet rastering cycles. (c) Droplet roll off angle as a function of droplet rastering cycles.

Second, we measured the manipulator mass and visually inspected the manipulator surface as a function of droplet rastering cycles, sequentially with multiple liquids (hexadecane, water, Bradford reagent, BSA, milk, virus replicon particle laden solution, thrombin, whole blood, fibrinogen and PRP), on a single biofluid manipulator. In each cycle, a 30 μL pendant droplet of the desired liquid was rastered across the surface of the same biofluid manipulator using a linear translation stage. The manipulator's surface appearance was inspected, and the manipulator mass was measured after every 50 cycles. Even after 1000 droplet rastering cycles with each liquid, sequentially on the same manipulator, there is neither a significant change in the manipulator mass (see Fig. 2.6b) nor any change in manipulator surface appearance. These

results also confirm that there is neither liquid loss nor noticeable cross-contamination associated with our droplet manipulations.

Third, we measured the roll off angles as a function of droplet rastering cycles, sequentially with multiple liquids (hexadecane, water, Bradford reagent, BSA, milk, virus replicon particle laden solution, thrombin, whole blood, fibrinogen and PRP), on a single biofluid manipulator. In each cycle, a 30 μL pendant droplet of the desired liquid was rastered across the surface of the same biofluid manipulator using a linear translation stage. The roll off angle of the liquid (which is very sensitive to surface inhomogeneity) was measured after every 50 cycles. Even after 1000 droplet rastering cycles with each liquid, sequentially on the same manipulator, there is no significant change in the roll off angle of any droplet (see Fig. 2.6c). These results further confirm that there is neither liquid loss nor noticeable cross-contamination associated with our droplet manipulations.

2.4 In-plane droplet manipulation

To demonstrate on-demand, remote and loss-less, in-plane manipulation of droplets with our biofluid manipulators, we designed two different manipulators – one for simultaneous manipulation of droplets and another for sequential manipulation of droplets. While simultaneous in-plane manipulation of droplets enables automation of simple single-step processes (e.g., colorimetric assays, where a single indicator is used to detect a single analyte), sequential in-plane manipulation enables automation of multi-step processes, which involve sequential mixing of droplets at different time intervals (e.g., colorimetric enzymatic assays, where multiple indicators are utilized to detect a single/multiple analytes that require sequential droplet manipulation).

2.4.1 In-plane simultaneous droplet manipulation

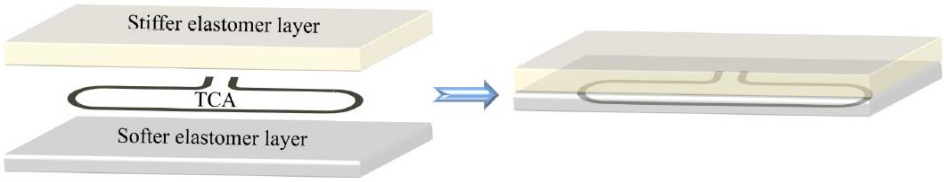

Figure 2.7. Manipulator for simultaneous droplet manipulation. A schematic illustrating the fabrication of manipulators for in-plane simultaneous droplet manipulation.

For simultaneous manipulation of droplets, our design consisted of a single heterochiral TCA in an elliptical shape with the stiffer elastomer layer facing upward (see Fig. 2.7) such that the two free ends of manipulator can bend upward simultaneously upon actuation. The manipulator was rendered superomniphobic by spray coating with fluorinated fumed silica particles.

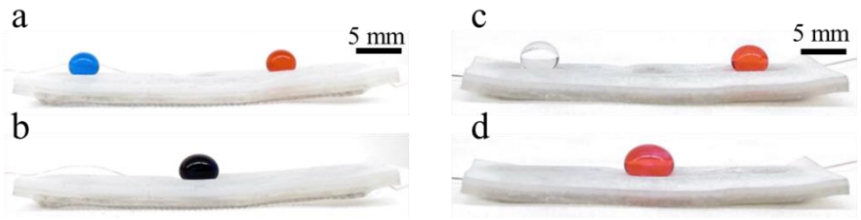

Figure 2.8. In-plane simultaneous droplet manipulation. (a)-(b) & (c)-(d) On-demand, remote and lossless, in-plane simultaneous manipulation of water droplets (dyed blue and red) and n-hexadecane droplets (colorless and dyed red), respectively, with our biofluid manipulator.

To demonstrate simultaneous manipulation of droplets, we placed two 25 μL water droplets (dyed red and blue) close to the free ends of the manipulator (initially horizontal; see Fig. 2.8a). Then, we actuated the manipulator to initiate its bending upward. When the tilt exceeded the roll off angle ω, the red and blue water droplets rolled simultaneously along the manipulator surface and mixed with each other (see Fig. 2.8b). In addition to handling high surface tension aqueous droplets, our manipulator allows handling of a wide variety of low

surface tension droplets, as evident from simultaneous manipulation and mixing of two n-hexadecane droplets (colorless and dyed red; see Figs. 2.8c & d).

2.4.2 In-plane sequential droplet manipulation

For sequential manipulation of droplets, our design consisted of three manipulators that can be actuated independently (see Fig. 2.9a). The three manipulators were arranged around a triangular-shaped domain. While the manipulators were rendered superomniphobic by spray coating with fluorinated fumed silica particles, the triangular-shaped domain was not super-repellent. In other words, liquid droplets displayed low adhesion on the biofluid manipulators and high adhesion on the triangular-shaped domain. This allowed the triangular-shaped domain to act as a site that traps droplets and enables interactions (e.g., mixing, reaction etc.).

To demonstrate sequential manipulation of droplets, we placed three 25 μL water droplets (dyed in red, yellow and blue) close to the free end of each of the three manipulators (initially horizontal, see Fig. 2.9b). Then, we actuated one of the manipulators (with the red water droplet) to initiate its bending. When the tilt exceeded the roll off angle ω, the red water droplet rolled down under gravity, along the manipulator surface and got trapped in the triangular-shaped domain (see Fig. 2.9c). Upon actuation of the second manipulator (with the yellow water droplet), the yellow water droplet rolled down and mixed with the red droplet in the triangular-shaped domain (see Fig. 2.9d). Similarly, actuation of the third manipulator (with the blue water droplet) allowed the blue water droplet to roll down and mix with the droplet in the triangular-shaped domain (see Fig. 2.9e). In this manner, droplets can be sequentially or simultaneously transported and mixed on-demand in a lossless manner with our manipulators.

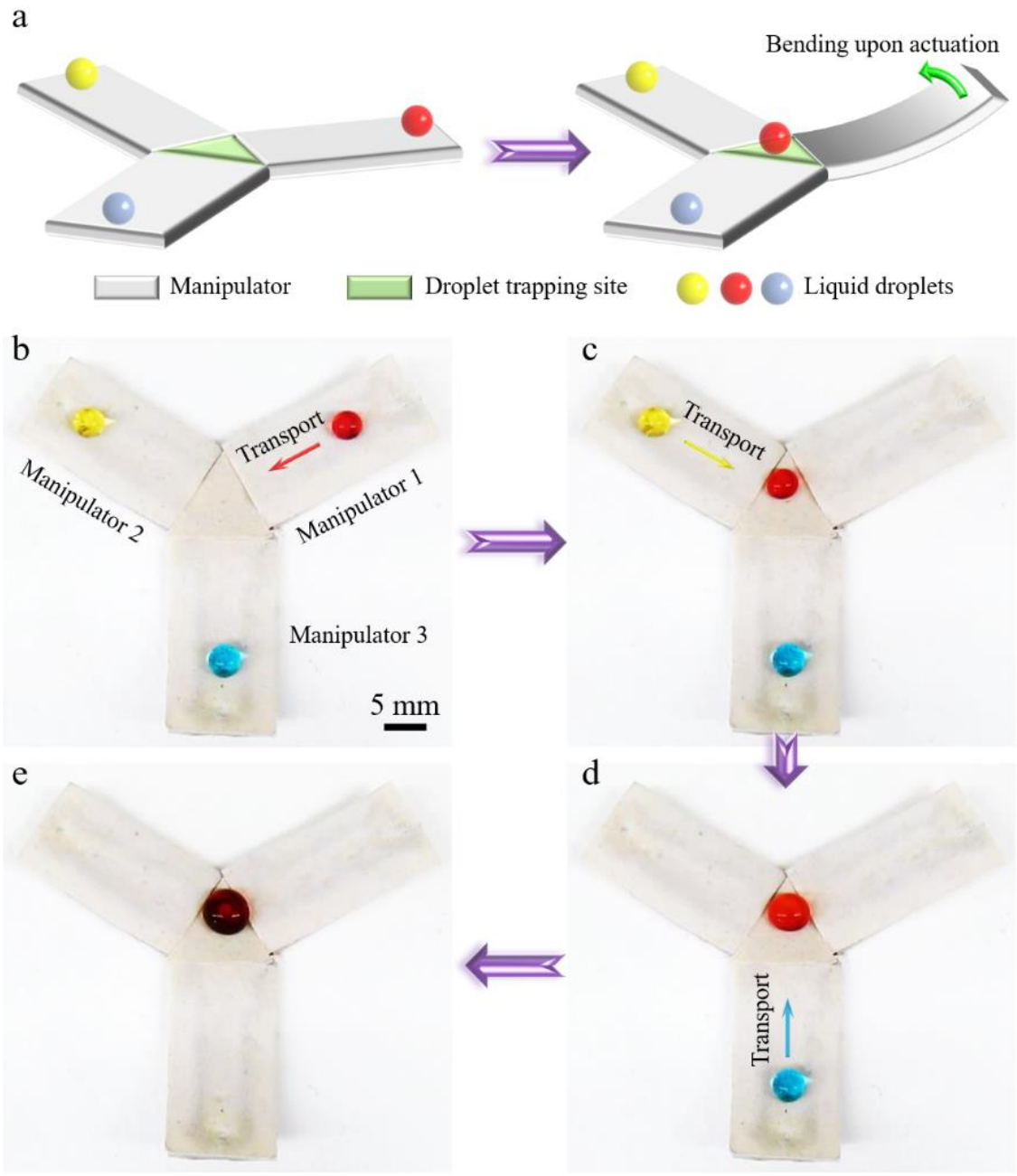

Figure 2.9. In-plane sequential droplet manipulation. Schematic depicting the design of three manipulators for in-plane sequential manipulation of liquid droplets. Each manipulator can be actuated independently. (b)-(e) On-demand, remote and lossless, in-plane sequential manipulation of water droplets. Upon actuation, each droplet is sequentially transported to the trapping site (i.e., triangular-shaped domain).

2.4.3 Out-of-plane droplet manipulation

To demonstrate on-demand, remote and lossless, out-of-plane manipulation of droplets with our manipulators, we designed a droplet gripper consisting of two vertical manipulators with folded stainless steel meshes attached to the free ends (see Fig. 2.10a). All manipulator surfaces were rendered superomniphobic by spray coating with fluorinated fumed silica particles. Two manipulators were aligned such that the stiffer elastomer layers faced each other so that the manipulators can bend towards each other upon actuation to initiate gripping action. The folded stainless steel meshes (similar to a ladle) provided the geometric constraint necessary to prevent undesired slip of the liquid droplets during the controlled pickup and release operations. When the two manipulators were actuated by applying 3 V, the asymmetric elongation induced by Joule heating caused them to bend towards each other and the distance between them decreased until they came in contact with each other (see Fig. 2.10b). When the voltage was turned off (i.e., 0 V), the two superomniphobic manipulators recovered their original shapes (see Fig. 2.10c). Utilizing our droplet gripper, we could generate sufficient force to hold a 3.6 g droplet of gallium-indium liquid metal (see Fig. 2.10d).

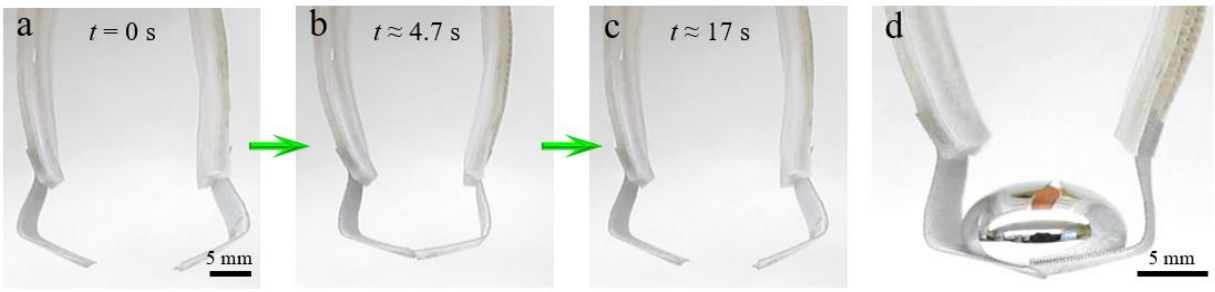

Figure 2.10. Droplet gripper. (a)-(c) Droplet gripper consisting of two manipulators. When the voltage was applied, distance between the manipulators decreased until they contacted each other. When the voltage was turned off, the gripper recovered its original shape. (d) Droplet gripper holding a 3.6 g gallium-indium liquid metal droplet.

Furthermore, utilizing our droplet gripper, we performed pick-and-place operations (i.e., droplets were gripped, lifted, transported, and released) to demonstrate out-of-plane droplet manipulation. Our droplet gripper can enable pick-and-place operations for a wide variety of liquid droplets. To demonstrate this, we placed two 40 μL droplets of water (a representative high surface tension liquid; one droplet dyed blue and another dyed yellow) on a superomniphobic surface (see Fig. 2.11a). The droplet gripper was initially positioned above the blue water droplet. Using a translation stage, the droplet gripper was lowered. Upon approaching the droplet, we actuated the two manipulators so that blue water droplet could be gripped (i.e., picked up out-of-plane from the surface) on-demand. Subsequently, using the translation stage, the blue water droplet was lifted, transported in the horizontal direction until it is positioned above the yellow water droplet, and then descended (see Fig. 2.11b). Subsequently, the voltage was turned off so that the blue droplet could be released (out-of-plane) on-demand, in a lossless manner (due to the low adhesion of the superomniphobic surfaces) and mixed with the yellow droplet (see Fig. 2.11c).

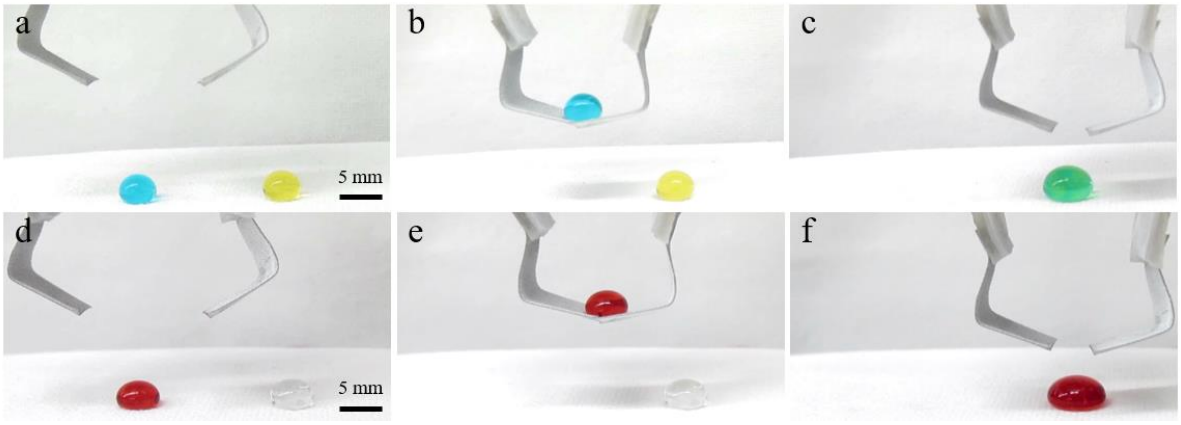

Figure 2.11. Out-of-plane droplet manipulation. (a)-(c) & (d)-(f) On-demand, remote and lossless, pick-and-place operations (i.e., out-of-plane manipulation) of water droplets (dyed blue and yellow) and n-hexadecane droplets (colorless and dyed red), respectively.

In addition to high surface tension aqueous droplets, our manipulators can also be used to perform on-demand and lossless pick-and-place operations with low surface tension liquid droplets. To demonstrate this, an n-hexadecane droplet dyed red was gripped, lifted, transported, and released on a colorless n-hexadecane droplet (see Figs. 2.11d, e and f). In this manner, droplets can be transported out-of-plane and mixed on-demand in a lossless manner with our manipulators. Due to the simplicity and versatility of our design, it is easy to fabricate a large array of manipulators for in-plane (i.e., simultaneous and sequential) and out-of-plane manipulations of multiple droplets and incorporate them into inexpensive, simple and potable robotic systems for point-of-care operations.

2.5 Practical utility of biofluid manipulators

In order to illustrate the practical utility of our manipulators in reducing the exposure of clinical laboratory personnel and healthcare workers to infectious specimens, we demonstrate on-demand, remote and lossless manipulation of biofluid droplets. While maneuvering of solids has been reported in prior studies,[68,69] to the best of our knowledge, on-demand, remote and lossless handling of biofluid droplets has never been demonstrated. Here, we demonstrate a simple in-plane simultaneous manipulation of biofluid droplets relevant to biological assays (e.g., colorimetric assays and blood coagulation assays).

2.5.1 Biofluid manipulators for colorimetric assays

For colorimetric assays, we demonstrate protein detection with Bradford reagent (Coomassie Blue G-250 dye). We placed 30 μL droplets of Bradford reagent (reddish brown) and liquids containing proteins (BSA, see Fig. 2.12a, b and c; milk, see Fig. 2.12d, e and f; virus replicon particle-laden solution, see Fig. 2.12g, h and i) on the free ends of our manipulators. Upon actuation, the droplets on either end rolled past the surface and started mixing with each

other at the center of the manipulator (see Fig. 2.12b, e and h). While mixing, the droplets displayed a color change to blue, indicating the presence of proteins (see Fig. 2.12c, f and i). This is because Bradford reagent forms a dye-protein complex, which leads to a shift in its absorption wavelength from ≈ 470 nm to ≈ 595 nm.[70-72] In this manner, our biofluid manipulators can be used to detect the presence of proteins in a wide range of biofluids commonly used in clinical settings.

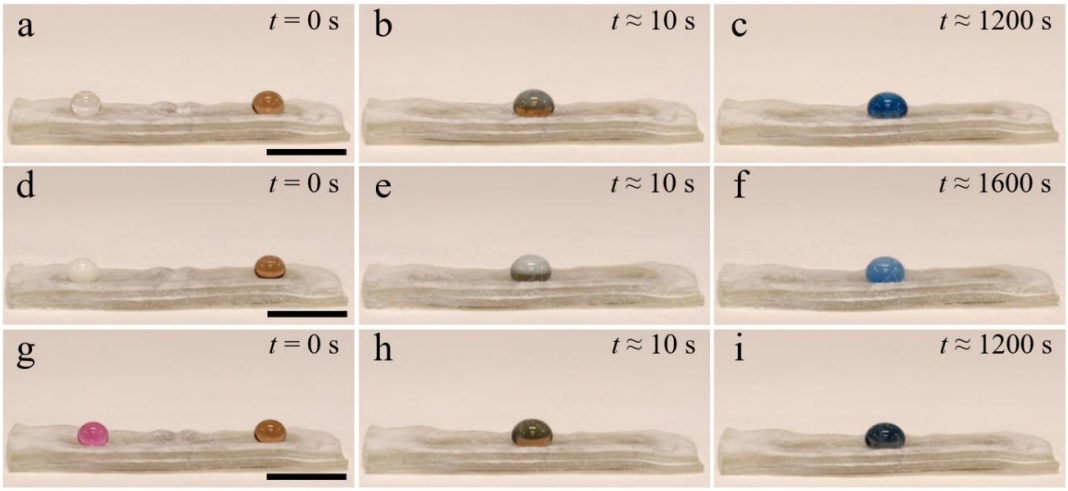

Figure 2.12. Biofluid manipulators for colorimetric assays. (a)-(c), (d)-(f) & (g)-(i) On-demand, remote and lossless, in-plane simultaneous mixing of BSA, milk and virus replicon particle-laden droplets, respectively, with Bradford reagent (right; reddish-brown) to demonstrate protein detection. The scale bar represents 10 mm.

2.5.2 Biofluid manipulators for blood coagulation assays

For blood coagulation assays, we demonstrate clotting of whole blood and blood components (e.g., PRP and fibrinogen) using thrombin. We placed 30 μL droplets of thrombin (colorless) and whole blood (red; see Fig. 2.13a), PRP (cloudy; see Fig. 2.13d) and fibrinogen (colorless; see Fig. 2.13g) on the free ends of our biofluid manipulators. Upon actuation, the droplets on either side rolled past the surface and merged with each other at the center of the

manipulator (see Fig. 2.13b, e and h). After merging with thrombin, the viscosity of whole blood, PRP and fibrinogen gradually increased to transition from a liquid to a gel, indicating clot formation within the droplets (see Fig. 2.13c, f and i). This is because thrombin, a serine protease, cleaves fibrinogen (a soluble coagulation protein present in blood plasma) into fibrin monomers, which further polymerize to form a fibrous network resulting in gelation/clotting.[73-75] In this manner, our biofluid manipulators can be used to study the clotting kinetics using very small quantities of blood and blood components.

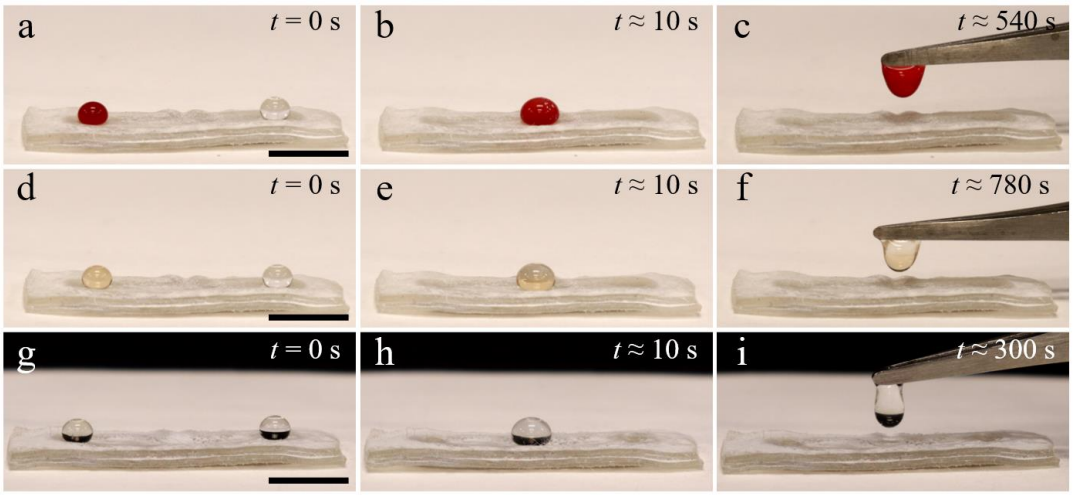

Figure 2.13. Biofluid manipulators for blood coagulation assays. (a)-(c), (d)-(f) & (g)-(i) On-demand, remote and lossless, in-plane simultaneous mixing of whole blood, PRP and fibrinogen droplets, respectively, with thrombin (right) to demonstrate clotting. The scale bar represents 10 mm.

While we demonstrated protein detection and blood coagulation qualitatively using our biofluid manipulators, the relevant quantitative parameters (e.g., protein, analyte or pathogen concentration in colorimetric assays and clotting time or coagulation factor in blood coagulation assays) can also be determined easily in conjunction with optical techniques (e.g., spectrophotometry, turbidometry etc.). Furthermore, unlike superhydrophobicity,

superomniphobicity of our manipulators allows droplet manipulation for a wide range of biofluids (water-based and lipid-based). Thus, on-demand, remote and lossless manipulation of wide range of biofluids (e.g., blood, saliva, urine etc.) can be performed utilizing our biofluid manipulators, thereby reducing the exposure of clinical laboratory personnel and healthcare workers to infectious specimens, especially during pandemics.

2.6 Conclusions

In this work, we developed biofluid manipulators, by combining twisted-and-coiled actuators embedded in a soft body with superomniphobic surfaces. Utilizing our manipulators, we demonstrated on-demand, remote and lossless manipulation of high surface tension and low surface tension liquid droplets, both in-plane (e.g., simultaneous and sequential transport) and out-of-plane (e.g., pickup and release). Furthermore, we demonstrated on-demand, remote and lossless manipulation of biofluid droplets to illustrate the utility of our manipulators in biological assays (e.g., colorimetric assays and blood coagulation assays). We envision that our biofluid manipulators will not only reduce manual operations and minimize exposure to infectious agents, but also pave the way for developing inexpensive, simple, and portable robotic systems, which can allow point-of-care operations, particularly in developing nations.

CHAPTER 3. SOFT ROBOTS WITH ENHANCED CHEMICAL RESISTANCE FOR CORROSIVE LIQUID ENVIRONMENTS

3.1 Introduction

Soft robots have gained significant attention for several applications in the food processing industry, oil & gas industry, healthcare, navigation, and disaster relief etc.[76-80] This is because they offer multiple advantages like flexibility, adaptability, stimuli-responsiveness, safety handling of fragile objects, mimicry of complex biological locomotion etc. compared to their rigid counterparts.[32,33,81] Several actuation technologies like pneumatic, magnetic, thermal etc. have been explored for soft robots using deformable materials like elastomers and gels.[82-84] Harsh liquids environments like the ones containing chemical spills of organic solvents (e.g., toluene), corrosive acids (e.g., sulfuric acid) or bases (e.g., aqueous sodium hydroxide solution) pose a severe threat to soft robots hindering them from performing their designated tasks and rendering them ineffective.[85] This is because most elastomers swell in the presence of organic solvents and display undesired structural changes within the soft robot disrupting the functionality of the soft robot.[86,87] Furthermore, acidic and alkaline liquid environments corrode the elastomer leading to physical damage to the soft robot.[88] Therefore, enhancing the chemical shielding of soft robots is highly desirable.

In this work, we developed bio-inspired soft robots with enhanced chemical shielding by imparting superomniphobicity to soft robots. We demonstrated excellent chemical shielding in the presence of different harsh and corrosive liquids consisting of acids like sulfuric acid and nitric acid and solvents like toluene and chloroform. Our soft robots with superomniphobic coatings demonstrated chemical shielding against concentrated sulfuric acid for timescales that at least an order of magnitude higher than those for soft robots without superomniphobicity. We

also demonstrated the grasp and release of solid objects and robots swimming under highly corrosive liquids (e.g., concentrated sulfuric acid and concentrated nitric acid) without showing any damage. We also demonstrated the enhanced chemical shielding on LCE and magnetic actuators in the presence of organic solvents (e.g., toluene and chloroform). We envision that our work will inspire developing novel soft robots that can survive and function effectively in harsh liquid environments for longer periods in applications related to food processing, healthcare, and chemical industries.

3.2 Superomniphobic soft actuators

In this work, we demonstrated enhanced chemical shielding on bio-inspired soft robots that are programmed for performing operations like grasp and release of solid objects under liquids, swimming under or on liquids by imparting super-repellency. To accomplish this, we fabricated bio-inspired soft robots (gripper, fish, and jellyfish) using pneumatic soft actuators and imparted superomniphobicity (see Fig. 3.1). Typically, superomniphobic coatings display extreme repellency to a wide range of liquids irrespective of their surface tension, viscosity, pH, toxicity etc. by trapping air pockets at solid-liquid interface and minimizing the solid-liquid contact.[6,12] We hypothesized that superomniphobic coatings will enhance chemical shielding on soft robots by protecting the underlying substrate from the surrounding harsh liquids (e.g., organic solvents and corrosive acids).

We fabricated pneumatic soft actuators by bonding a thinner elastomeric layer with embedded zig-zag channels on to a thicker elastomeric layer (courtesy Dr. Chi, Professor Yin's research group at North Carolina State University). We fabricated the elastomeric layers using Ecoflex 50 (Smooth-On Inc.) through well-established molding and demolding processes. Ecoflex 00-50 was poured into 3D printed molds (designed for top and bottom layers using

Ultimaker 3) and was peeled off after curing at 70°C for 1 hour. The top layer was then bonded to the pre-stretched bottom layer using uncured Ecoflex. Finally, the Ecoflex was let to cure at 70°C for 1 hour and the pre-strain was released to obtain the pneumatic actuator. Upon inflation with air, the pneumatic actuator bends towards the thicker layer due to its higher bending stiffness and the expansion of top layer due to pneumatic pressure, and on deflation, the pneumatic actuator recovers its original shape. In this manner, we can reversibly bend the pneumatic actuator by inflation and deflation.

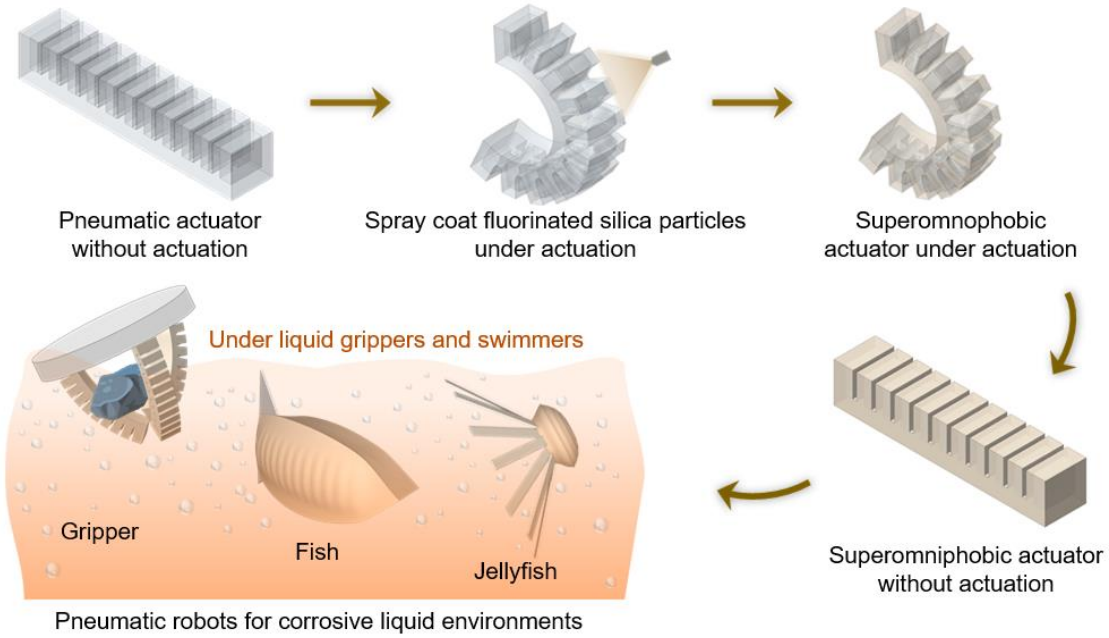

Figure 3.1. Soft robots for corrosive liquid environments. A Schematic depicting the fabrication of superomniphobic pneumatic robots (gripper, fish & jellyfish) to function in corrosive liquid environments.

We imparted superomniphobicity to the pneumatic actuator by spray coating fluorinated silica particles on an inflated actuator under maximum strain (see Fig. 3.1). The pneumatic actuators were spray coated under maximum strain to ensure that the superomniphobicity is robust under elongation/actuation. The fluorinated silica particles were prepared via liquid phase

silanization of fumed silica nanoparticles (7 nm; Sigma-Aldrich) with heptadecafluoro-1,1,2,2-tetrahydrodecyl trichlorosilane (Gelest Inc.) in hexane for 1 day. The solution was then spray coated on to an inflated actuator using an air brush held at 15 cm from the surface at a pressure of 30 psi. The actuator was then dried at room temperature and deflated before its use.

We characterized the surface morphology of our superomniphobic coating using a scanning electron microscope (JEOL JSM-6500F) at 10 kV. The superomniphobic surfaces (flat spray coated Ecoflex sheets) were sputter coated with gold/palladium target to make the surface conductive (to avoid charging) for SEM imaging. Low solid surface energy due to fluorination and appropriate texture (i.e., re-entrant morphology) due to the agglomerated silica particles rendered the surface superomniphobic (see Fig. 3.2).[89,90] The superomniphobicity was also evident from droplets of a wide variety of liquids (water, 98% sulfuric acid, hexadecane, and toluene) beading up on the surface (see Fig. 3.2).

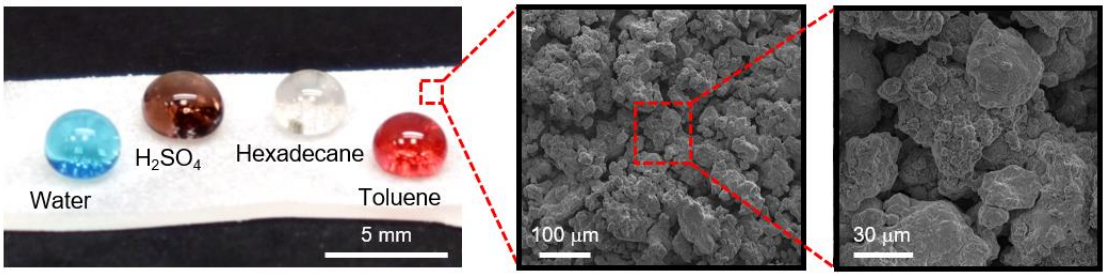

Figure 3.2. Surface morphology. Image (left) depicting the different liquid (i.e., high surface tension liquid like water, corrosive liquid like sulfuric acid, low surface tension liquid like hexadecane, organic solvent like toluene) droplets beading up on a superomniphobic Ecoflex sheet. SEM images depict the surface morphology of superomniphobic siloxane sheet.

We also characterized superomniphobicity by investigating surface wettability using multiple liquids having different surface tension and pH. We investigated surface wettability by measuring the advancing and receding contact angles and roll off angles of 20 μL liquid droplets

using contact angle goniometry. Based on our results, both low and high surface tension liquids (hexadecane, γ_{lv} = 27.5 mN m^{-1} & water γ_{lv} = 72.8 mN m^{-1}) displayed very high apparent contact angles (> 150°) and very low roll off angles (< 10°; see Fig. 3.3a). Our superomniphobic coating also displayed very high apparent contact angles (> 150°) and very low roll off angles (< 10°) with liquids with a wide range of pH values (1 – 13; see Fig. 3.3b). This demonstrates the extreme repellency of our superomniphobic coating to all liquids irrespective of surface tension and pH.

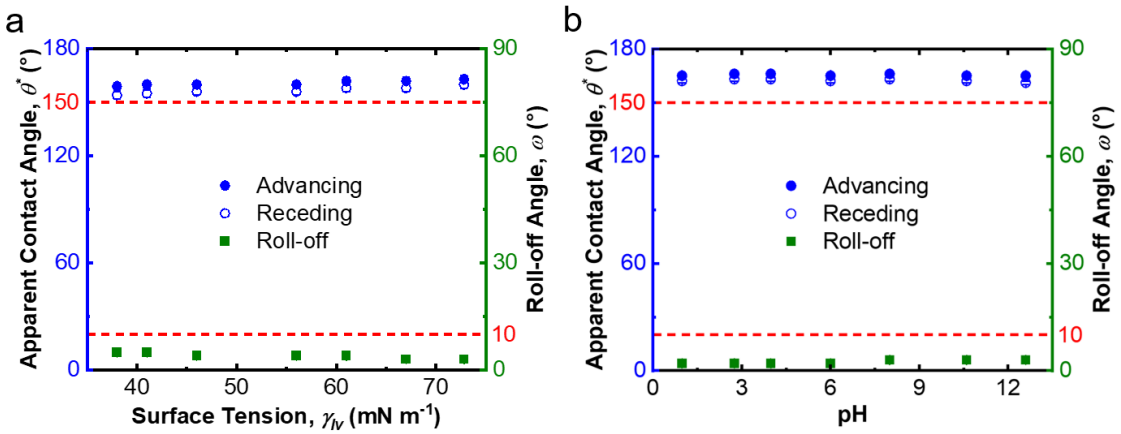

Figure 3.3. Superomniphobicity. (a) & (b) Apparent contact angles and roll off angles, respectively, of liquid droplets with different surface tensions and pH, respectively, on our superomniphobic coating. Roll off angles were measured with 20 μL droplets.

3.3 Chemical shielding with superomniphobicity

We investigated the chemical shielding of our superomniphobic coating by visually comparing the surface damage after placing droplets of harsh liquids (i.e., acids like concentrated sulfuric acid and solvents like toluene on bare and superomniphobic Ecoflex 00-50 sheets. While sulfuric acid disintegrates the material, toluene swells the Ecoflex 00-50 sheet producing undesired structural changes. When a 30 μL droplet of concentrated sulfuric acid was placed on bare Ecoflex 00-50 sheet, it displayed significant surface degradation in less than 15 minutes (see

Fig. 3.4a) while the superomniphobic siloxane sheet displayed no visible change in appearance or color (see Fig. 3.4b). Similarly, when a 30 μL droplet of toluene was placed on a bare Ecoflex 00-50 sheet, it started swelling immediately (in <2 minutes; see Fig. 3.4c) while the superomniphobic siloxane sheet displayed no visible swelling (see Fig. 3.4d). These results demonstrate that superomniphobic coatings can enhance chemical shielding by mitigating the surface degradation in presence of acids and by minimizing the undesired structural changes in the presence of solvents.

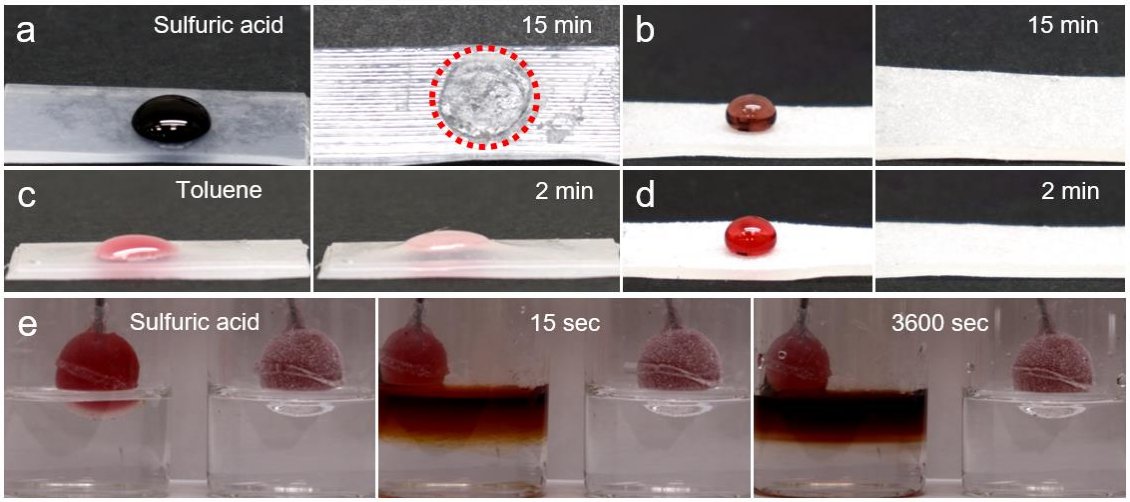

Figure 3.4. Damage in the presence of acids and solvents. (a) & (b) Images depicting the surface degradation on bare and superomniphobic Ecoflex 00-50 sheets, respectively, after contacting 30 μL concentrated sulfuric acid droplets. (c) & (d) Images depicting the swelling on bare and superomniphobic Ecoflex 00-50 sheets, respectively, after contacting 30 μL toluene droplets. (e) Time-lapse images depicting dyed water (red) leaking from uncoated (left) and superomniphobic (right) Ecoflex balloons due to damage propagation through the thickness in the presence of concentrated sulfuric acid. Superomniphobic Ecoflex balloon was able to hold water without leaking for at least for 1 hour indicating the enhanced chemical shielding on the balloon due to the coating.

To further understand the enhancement in chemical shielding on Ecoflex sheets due to superomniphobic coating, we investigated damage propagation by inspecting a water leak from an uncoated and superomniphobic Ecoflex balloon filled with dyed water immersed in concentrated sulfuric acid. Upon contacting sulfuric acid, the uncoated balloon displayed a water leak in <15 s indicating the propagation of damage through the thickness of balloon in the presence of acid (see Fig. 3.4e). However, the superomniphobic siloxane balloon did not display any water leak for at least 1 hour. These results further demonstrate the enhanced chemical shielding offered by superomniphobic coating even under inflation. To reaffirm the extreme repellency of our superomniphobic coating to harsh liquids, we also demonstrated droplet bouncing with concentrated acids like 98% sulfuric acid and 70% nitric acid and solvents like toluene and chloroform on superomniphobic Ecoflex sheets (see Fig. 3.5).

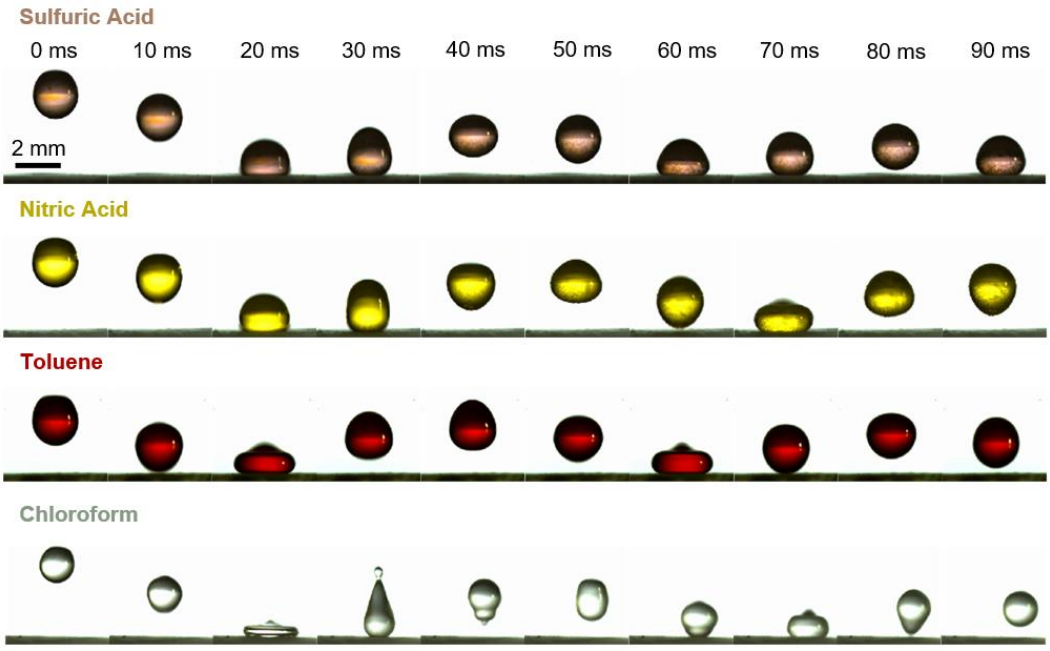

Figure 3.5. Droplet bouncing. Time-lapse images depicting the droplets of 98% sulfuric acid, 70% nitric acid, toluene, and chloroform bouncing on a superomniphobic Ecoflex sheet confirming the extreme repellency of the coating towards harsh liquids.

3.4 Superomniphobicity with strain

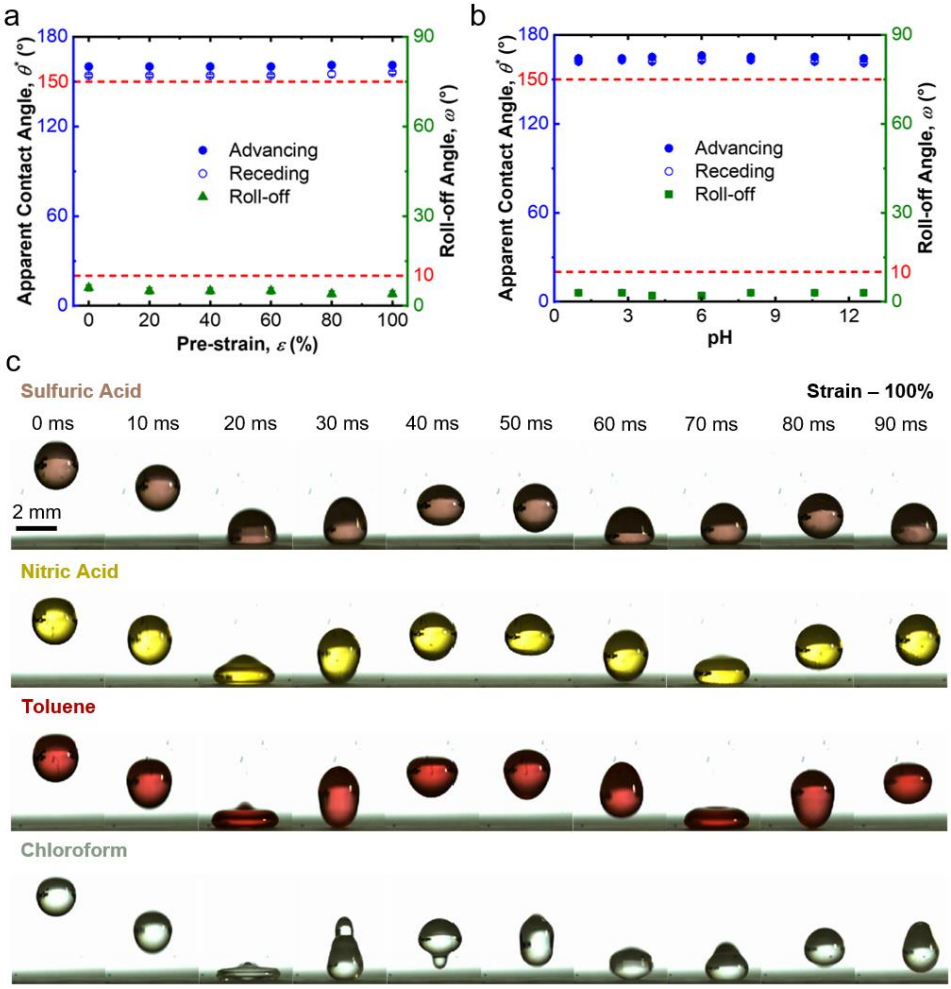

Figure 3.6. Superomniphobicity vs. strain. (a) Apparent contact angles and roll off angles of hexadecane on a superomniphobic siloxane sheet as a function of uniaxial strain. (b) Apparent contact angles and roll off angles of liquids with different pH values on a superomniphobic Ecoflex sheet at 100% uniaxial strain. (c) Time-lapse images depicting droplets of 98% sulfuric acid, 70% nitric acid, toluene, and chloroform bouncing on a superomniphobic Ecoflex sheet under 100% uniaxial strain.

We also investigated the influence of strain on the superomniphobicity of pneumatic soft actuator. This is important because the actuator must retain superomniphobicity throughout the actuation cycle under different strains and any loss in the repellency might expose the actuator to

corrosive liquid environments and result in surface damage or undesired structural changes in the actuator. To understand the influence of strain, we measured advancing and receding contact angles and roll off angles (of 20 μL droplets) of hexadecane and liquids with different pH on superomniphobic Ecoflex sheets under different uniaxial strains.

All tested liquids displayed very high contact angles (> 150°) and very low roll off angles (< 10°) up to 100% uniaxial strain, which is much higher than the maximum strain the pneumatic actuator experiences under actuation (see Fig. 3.6a). Furthermore, all tested liquids with different pH values (1 – 13) also displayed very high contact angles and low roll off angles (see Fig. 3.6b). These results indicate the robustness of superomniphobicity on the pneumatic actuator under actuation in harsh liquid environments. Such robustness can also be visualized from corrosive liquid (acids like sulfuric acid and nitric acid) and solvent (toluene and chloroform) droplets bouncing on a superomniphobic siloxane sheet at 100% uniaxial strain (see Fig. 3.6c).

3.5 Soft robots under corrosive liquid environments

To demonstrate practical utility, we fabricated superomniphobic soft robots using pneumatic actuators for performing simple grasp and release operations of solid objects in corrosive liquids and for swimming on and under corrosive liquids without any surface damage. To demonstrate the grasp and release of solid objects, we designed a gripper consisting of three superomniphobic pneumatic actuators.[91] The actuators were fixed in a 3D printed fixture in such a way that the bottom layers are facing each other. On inflation, all actuators curve toward the bottom layer and form a claw shape, which helps in holding and gripping the solid objects. On deflation, the actuators recover their original shape, and the solid object can be released. To demonstrate this, we showed grasp and release of a glass vial immersed in sulfuric acid using our gripper. First, we gradually lowered the gripper manually until it was immersed in sulfuric acid

and was on top of the glass vial. Later, we inflated all actuators of the gripper so that they bend around the sides of the glass gripping the object (see Fig. 3.7a). Once the grip is firm, we gradually ascended the gripper out of sulfuric acid while gripping the vial. In order to release the glass vial, we lowered the gripper again manually into sulfuric acid and deflated the actuators so that they recover their original shape releasing the glass vial in the solution (see Fig. 3.7). We did not observe any surface damage, discoloration, or any liquid residue on the gripper, which confirms the robustness of the coating in protecting the gripper from acid corrosion. In this manner, we can utilize our gripper to perform simple grasp and release operations in the practical applications that require soft robots to function in hazardous liquid environments.

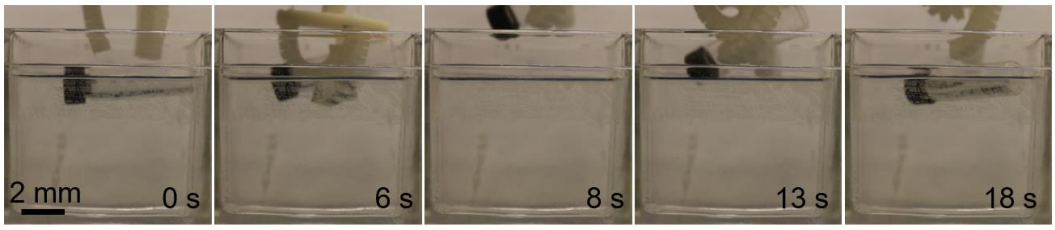

Figure 3.7. Gripper. Time-lapse images demonstrating grip and release of a glass vial from sulfuric acid solution.

We also designed soft robots that can swim under hazardous liquid environments to demonstrate the relevance of our work for a wide variety of soft robots that perform different types of tasks in practical applications. We demonstrated swimming of superomniphobic fish and jellyfish in acidic environments. We designed the fish by bonding two pneumatic actuators on their bottom so that exterior sides of fish consist of embedded zig-zag channels for inflation and deflation. We attached a plastic tail to generate enough thrust for the fish so that it can move forward. We also added a floating dead weight on the front side of the fish to facilitate swimming at a constant level from the liquid surface. By alternatively inflating and deflating the exterior sides of the fish, we can generate the yaw motion required for swimming. All the

exterior surfaces of fish and the components of dead weight were rendered superomniphobic by spray coating with fluorinated silica particles. By controlling the inflation/deflation cycles, we were able to propel the fish forward in a tank containing nitric acid without any damage (see Fig. 3.8a).

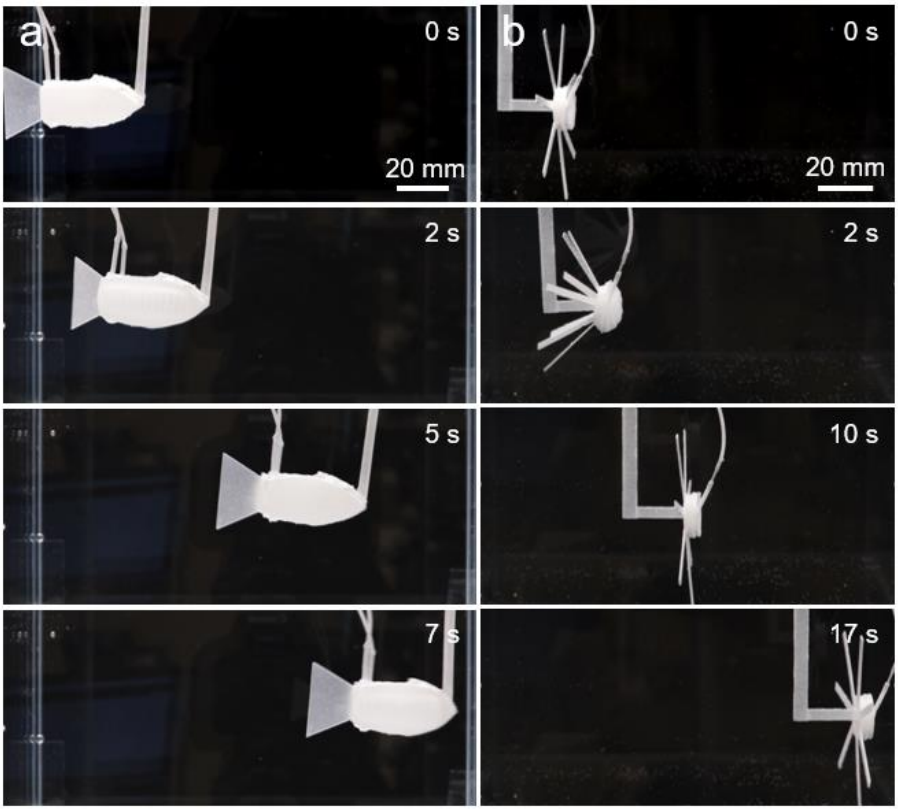

Figure 3.8. Fish and Jellyfish. (a) & (b) Time-lapse images demonstrating the swimming of fish and jellyfish, respectively, in a tank containing nitric acid solution.

We designed jellyfish by bonding a circular top layer with pneumatic channel in spiral shape on to a thinner bottom layer.[91] Thin plastic strips were also bonded between the layers to provide enough thrust to the forward motion. On inflation, the actuator forms a dome shape pushing the plastic strips backward (like jellyfish shape). On deflation, the actuator recovers its original shape. We added a floating dead weight on the backside side of the jellyfish to facilitate swimming at a constant level from the liquid surface. By controlling the inflation/deflation

cycles, we were able to propel the jellyfish forward in a tank containing nitric acid without any damage (see Fig. 3.8b).

3.6 Soft robots with other actuation mechanisms

To demonstrate the relevance of our approach to soft robots with other actuation mechanisms, we fabricated actuators that utilize heat and magnetic field as stimulus and demonstrated their actuation/locomotion in the presence of hazardous liquids. We used solvents (toluene & chloroform) as our hazardous liquids to demonstrate chemical shielding in liquid systems in addition to acidic systems. Typically, solvents swell the substrate and produce undesired structural changes unlike the material degradation seen with acids. We fabricated thin ribbons using liquid crystal elastomer (LCE) to represent actuators that work using heat as stimulus.[92] Typically, LCE actuators display a macroscopic deformation due to a phase change between the nematic and isotropic phases above or below the transition temperature.[93]

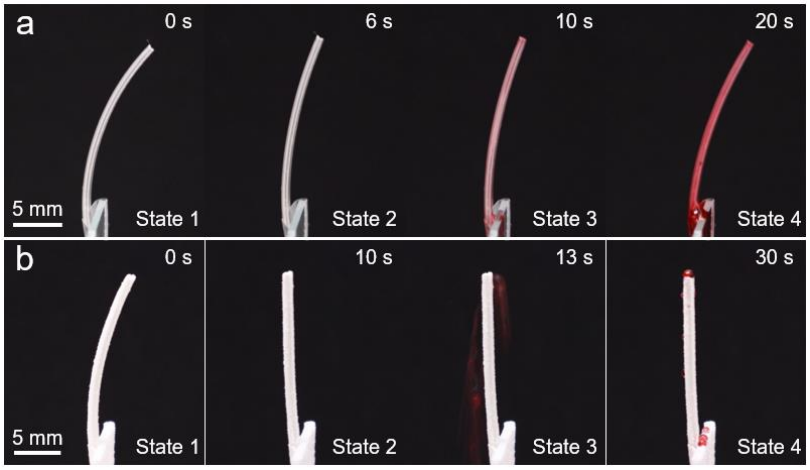

Figure 3.9. LCE actuators. (a) & (b) Time-lapse images illustrating the bending of uncoated and superomniphobic LCE ribbons, respectively, when exposed to a temperature of 100°C. State 1 represents the original shape of the ribbons. State 2 shows the bending of the ribbons at 100°C. State 3 shows the bending of the ribbons in the presence of toluene droplets. State 4 shows the bending after impaling with toluene droplets.

The LCE ribbons were synthesized using liquid crystal mesogenic monomer 1,4-bis-[4-(3-acryloyloxypropyloxy)benzoyloxy]-2-methylbenzene (RM 257; Wilshire Technologies) via thiol-acrylate Michael addition reaction method (courtesy Dr. Chi, Professor Yin's research group at North Carolina State University).[92] The nematic-isotropic phase transition temperature for the LCE is ≈ 80°C. By exposing the LCE ribbon to temperatures above 80°C, we can induce bending. We imparted superomniphobicity to the LCE ribbon by spray coating with fluorinated silica particles. To demonstrate chemical shielding on the LCE ribbon, we investigated the bending of uncoated and superomniphobic LCE ribbons in the presence of toluene droplets. The LCE ribbons were vertically mounted on a glass slide with the bottom fixed to surface and were exposed to a temperature of 100°C using a handheld infrared (IR) heater. The LCE actuators displayed contraction towards the heating direction because of nematic-isotropic phase transition (see Fig. 3.9a & b; state 1 and state 2). Once the LCE ribbons attained the maximum deformation, we impaled toluene droplets on the ribbons (see Fig. 3.9a & b; state 3). As soon as the toluene droplets contacted the uncoated LCE ribbon, it displayed swelling. Furthermore, the uncoated LCE ribbon started recovering its original shape because of drop in the surface temperature due to heat lost to toluene (see Fig. 3.9a, state 4). On the other hand, when the toluene droplets impinged on the superomniphobic LCE ribbon, the droplets started bouncing off from the surface due to superomniphobicity. Consequently, the superomniphobic LCE ribbon did not display any swelling or change in the bending (see 3.9b, state 4). These results indicate that superomniphobic coatings can retain the performance of the actuator in the presence of hazardous liquids.

To demonstrate the effect of chemical shielding on magnetic actuators, we fabricated the actuators by casting thin sheets of Ecoflex 00-50 with neodymium (NdFeB; permanent magnet)

particles (courtesy Dr. Chi, Professor Yin's research group at North Carolina State University) and investigated their locomotion in the presence of chloroform under magnetic field. We imparted superomniphobicity to the magnetic Ecoflex sheet by spray coating with fluorinated silica particles. We placed the uncoated and superomniphobic sheets in a petri dish containing chloroform and induced crawling motion using a magnet. The uncoated sheet displayed significant swelling and curling due to chloroform resulting in random movements making it difficult to control (see Fig. 3.10a). On the other hand, the superomniphobic sheet did not display any significant swelling in the presence of chloroform and the locomotion was controllable (see Fig. 3.19b). These results confirm the retention of performance due to the enhanced chemical shielding on soft actuators (irrespective of the actuation mechanism) in the presence of hazardous liquids.

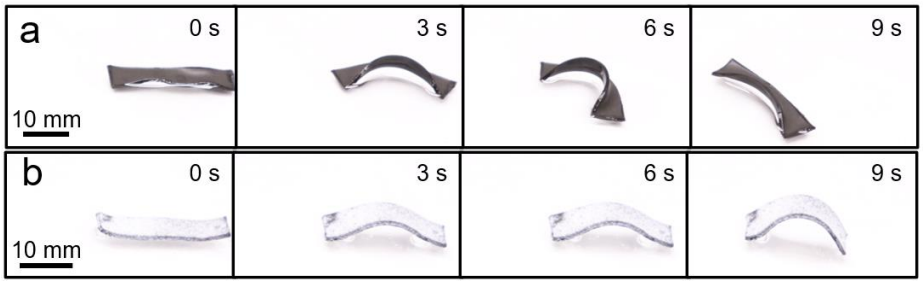

Figure 3.10. Magnetic actuators. (a) & (b) Time-lapse images illustrating the locomotion of magnetic uncoated and superomniphobic Ecoflex sheets using a magnet.

3.7 Conclusions

In summary, in this work, we developed bio-inspired soft robots using pneumatic actuators with enhanced chemical shielding so that they can survive and function under harsh liquid environments. We enhanced the chemical shielding by imparting superomniphobicity. We investigated chemical shielding due to superomniphobicity by inspecting any surface damage or swelling on uncoated and superomniphobic Ecoflex sheets in the presence of concentrated

sulfuric acid and toluene. We also investigated the surface damage under inflation in the presence of concentrated sulfuric acid by inspecting a dyed water leak from uncoated and superomniphobic Ecoflex balloon. Our results indicate that the superomniphobic Ecoflex balloon can retain the water without any leaking for at least 1 hour while the uncoated Ecoflex balloon displayed a water leak in < 15 s. We developed superomniphobic soft robots and demonstrated the grasp and release of solid objects in sulfuric acid and swimming on and under sulfuric acid and nitric acid environments without any visible surface damage. Furthermore, we demonstrated the actuation of soft actuator with magnetic field and heat as stimulus in solvents like chloroform and toluene without any visible swelling. Based on our results, we envision that our work will inspire developing novel soft robots that can survive and function efficiently in harsh liquid environments (acids, bases, or solvents) for longer periods in multiple applications related to food processing, healthcare, and chemical industries.

CHAPTER 4. DESIGNING NON-TEXTURED, ALL-SOLID, SLIPPERY HYDROPHILIC SURFACES

4.1 Introduction

Slippery surfaces (i.e., surfaces enabling high mobility of liquids) have received significant attention due to their wide range of applications in self-cleaning, drag reduction, enhanced condensation, biomedical implants etc.[1,2,8,94-96] In the past two decades, most slippery surfaces have been fabricated using two approaches, both of which rely on principles of fluid-film lubrication.[19] The first approach employs super-repellent surfaces,[20,90,97-99] which use texture to trap pockets of air at the solid surface. The trapped air acts as a gaseous lubricant, reducing the solid-liquid interfacial area and inducing slip at the liquid-air interface.[5,100] The second approach employs lubricant-infused surfaces,[21 101] which use texture to trap pockets of a liquid, immiscible with the contacting liquids, at the solid surface. The trapped immiscible liquid acts as a liquid lubricant, reducing the solid-liquid interfacial area and inducing slip at the liquid-liquid interface.[102] Despite the appeal of super-repellent surfaces and lubricant-infused surfaces, they lose slipperiness due to damage of texture, depletion of air via dissolution or external pressure, or depletion of lubricant via evaporation or repeated use.[22,23,103-105]

To circumvent these issues, non-textured, all-solid slippery surfaces have been developed by covalently grafting brushes to substrates (i.e., tethering oligomers or polymers to surfaces).[106,107] Since these surfaces are non-textured and all-solid, concerns related to damage of texture and depletion of fluid are greatly mitigated. Nearly all non-textured, all-solid slippery surfaces are hydrophobic.[106-110] There are very few reports of non-textured, all-solid slippery hydrophilic surfaces,[3,111-113] and no studies systematically investigated or elucidated the design of such surfaces. In this work, we demonstrate that non-textured, all-solid, slippery hydrophilic

surfaces can be designed by covalently binding high surface energy brushes to smooth substrates, only at sufficiently high grafting densities, resulting in both physical and chemical homogeneity. Furthermore, we postulate a plateau in slipperiness above a critical grafting density, which occurs when the tethered brush size (i.e., twice the Flory radius[114]) is equal to the inter-tether distance. This plateau in slipperiness occurs because, at or above the critical grafting density, water molecules tend to move past the tethered brushes primarily via in-plane motion, with negligible penetration between the brushes, resulting in maximum and constant slipperiness.

Building on this understanding, we fabricated slippery hydrophilic (SLIC) surfaces by covalently binding polyethylene glycol (PEG) brushes to smooth substrates with a rapid (< 10 min) grafting-to approach. Our SLIC surfaces demonstrate exceptional performance in condensation and fouling-resistance compared to conventional (i.e., non-slippery) hydrophilic surfaces and slippery hydrophobic surfaces. Based on these results, non-textured, all-solid, slippery hydrophilic surfaces (e.g., SLIC surfaces) constitute an emerging class of surfaces with the potential to benefit multiple technological landscapes ranging from thermofluidics to biofluidics.

4.2 Designing SLIC surfaces

Hydrophilic surfaces can be fabricated by covalently attaching high surface energy oligomeric brushes (e.g., PEG brushes) to a solid surface.[115] Such hydrophilic surfaces can display slipperiness when contact angle hysteresis $\Delta\theta$ (i.e., the difference between advancing contact angle θ_{adv} and receding contact angle θ_{rec}) is low. Low contact angle hysteresis can be achieved when a surface has low physical and chemical inhomogeneities.[13,14] Non-textured (i.e., smooth) surfaces with very low surface roughness display low physical inhomogeneity. High grafting density σ leads to low chemical inhomogeneity. When hydrophilic PEG brushes are

grafted to smooth surfaces, slipperiness increases with increasing grafting density. This is because, at lower grafting densities, water molecules tend to penetrate the space between the PEG brushes (see Fig. 4.1a), resulting in pinning and higher hindrance to lateral mobility of water droplets, which in turn leads to lower slipperiness (i.e., higher $\Delta\theta$). As grafting density increases, the penetration of water molecules between the PEG brushes decreases, resulting in lower pinning and lower hindrance to lateral mobility of water droplets, which in turn leads to increasing slipperiness (i.e., decreasing $\Delta\theta$).

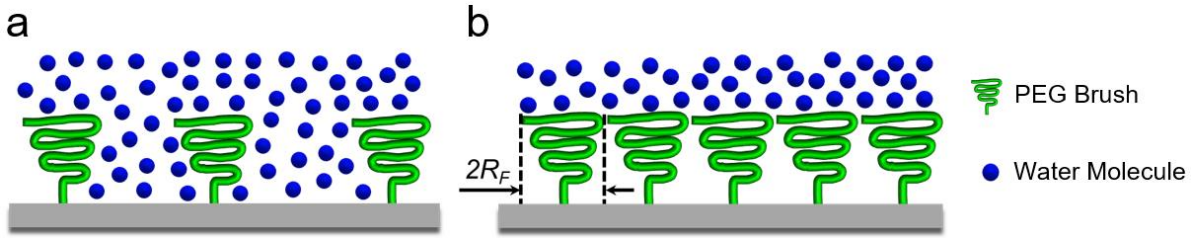

Figure 4.1. Designing SLIC surfaces. (a) A schematic depicting significant penetration of water molecules between PEG brushes at low grafting densities. (b) Schematic depicting negligible penetration of water molecules between PEG brushes at critical grafting density.

Here, we postulate that at or above a critical grafting density (i.e., $\sigma \geq \sigma_{crit}$), where the brush size (i.e., twice the Flory radius, $2R_F$) is equal to the inter-tether distance, slipperiness is maximum (i.e., $\Delta\theta$ is minimum) and constant. This is because, at or above the critical grafting density, water molecules tend to move past the oligomeric brushes primarily via in-plane motion with negligible penetration (see Fig. 4.1b), possibly due to an ice-like hydration layer.[116-118] These physical insights can be conveniently expressed in terms of the non-dimensional slipperiness factor $\sigma^* = \sigma/\sigma_{crit}$. When $\sigma^* < 1$, it signifies a regime where slipperiness increases with increasing grafting density, and when $\sigma^* \geq 1$, it signifies a regime of maximum and constant slipperiness. So, $\sigma^* > 1$ is a prudent criterion for designing non-textured, all-solid, slippery hydrophilic surfaces.

4.3 Fabricating SLIC surfaces

Building on this understanding, in this work, we fabricated SLIC surfaces by covalently grafting PEG brushes (molecular weight, $M \approx 330$ Da) to silicon wafers using a rapid grafting-to approach (see Fig. 4.2). We chose silicon wafers as substrates to minimize physical inhomogeneities (i.e., surface roughness, R_{rms}). We chose PEG functional groups to render high solid surface energy, which makes the surfaces hydrophilic. We used a simple and rapid liquid phase silanization[119] to covalently graft PEG brushes to hydroxylated silicon wafers, while maintaining low surface roughness (R_{rms} < 1 nm).

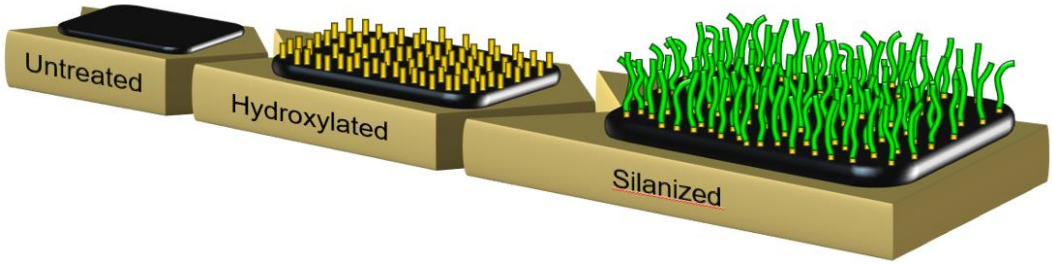

Figure 4.2. Fabricating SLIC surfaces. Schematic depicting the fabrication of SLIC surfaces via hydroxylation and silanization; hydroxyl groups (yellow), PEG brushes (green). Schematics are not to the scale and do not depict the precise molecular conformation of PEG brushes.

To covalently graft PEG brushes on to silicon wafers, first, the silicon wafers (<1 0 0> orientation; University Wafers) were cleaned by rinsing thoroughly with acetone (Fisher) and DI water, and then dried with nitrogen. The cleaned substrates were exposed to oxygen plasma (Plasma Etch PE-25) for 10 min for hydroxylation. To prepare hydrophilic surfaces, the hydroxylated samples were immersed in a solution consisting of 2 μL of 2-methoxy polyethyleneoxy (6-9) propyl trimethoxysilane (Gelest) and 12 μL hydrochloric acid (Fisher) in 45 mL of anhydrous toluene (Fisher) for the desired time at room temperature. We chose low molecular weight PEG silane to reduce steric hindrance and obtain higher grafting densities.

Finally, the silanized samples were cleaned by rinsing thoroughly with anhydrous toluene, DI water and ethanol (Fisher) sequentially, and then dried with nitrogen.

We characterized the surface chemistry on SLIC surfaces using XPS (Physical Electronics PHI-5800 spectrometer). XPS was conducted using a monochromatic Al Ka x-ray source operated at 15 kV, and photoelectrons were collected at a takeoff angle of 45° relative to the sample surface. XPS data was acquired from at least 5 spatially different locations on the surface and the spectral analysis was conducted using PHI Multipak software. The high resolution C1s XPS spectra on SLIC surfaces shows a C-O peak (at 286.5 eV) indicating the presence of PEG brushes (see Fig. 4.3a). The C-C peak (at 285 eV) on untreated silicon is due to the presence of adventitious carbon.

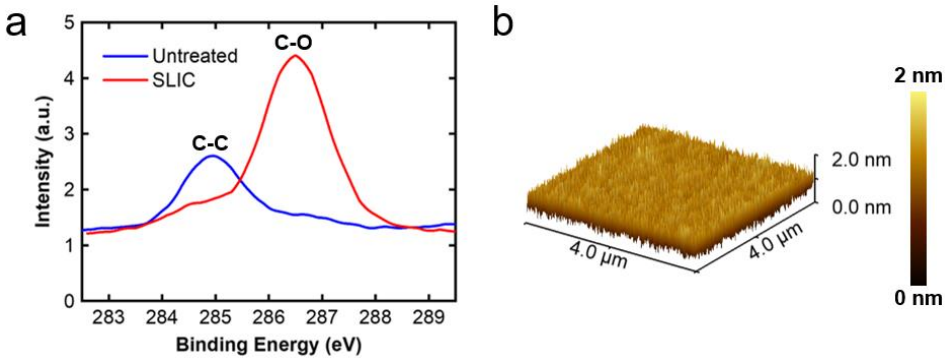

Figure 4.3. Surface chemistry and surface topography on SLIC surfaces. (a) High resolution C1s spectra of untreated silicon and SLIC surfaces. (b) AFM image depicting the topography of SLIC with root mean surface roughness R_{rms} < 1 nm.

4.4 Influence of PEG grafting density on wettability and slipperiness

To understand the influence of PEG grafting density on wettability and slipperiness, we systematically tuned the non-dimensional slipperiness factor σ^* by tailoring the silanization time t_{sil}. The non-dimensional slipperiness factor σ^* at different silanization times t_{sil} is defined as $\sigma^* = \sigma/\sigma_{crit}$. Grafting density σ (in chains nm^{-2}) on SLIC surfaces was estimated using $\sigma =$

$(h\rho N_A \text{ x } 10^{-21})/M$;[1] here, h is the thickness of the PEG layer (in nm) estimated using ellipsometry, ρ = 1.075 g cm^{-3} is the density of PEG, N_A = 6.023 x 10^{23} is Avogadro's number, and M = 330 Da is the average molecular weight of PEG with 6 to 9 monomers. Ellipsometry on SLIC surfaces was conducted at different t_{sil} using a variable angle spectroscopic ellipsometer (VASE-VB-250) to measure the thickness of PEG layer h. A spectral scan of the surface was collected between 500 nm and 900 nm for an incident angle between 55° and 75° with an increment of 5°. The thickness of PEG layer (refractive index = 1.45) was determined using a three-layer planar model (air/PEG/silica) of the solid surface from the collected spectra. At least five measurements were conducted at different locations on each surface.

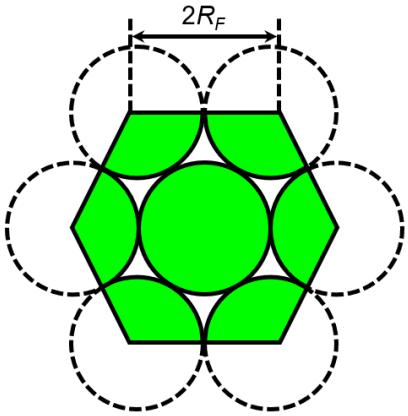

Figure 4.4. Hexagonal packing. A schematic depicting the hexagonal packing of PEG brushes (green) at critical grafting density σ_{crit}. Schematic is not to the scale.

We estimated the critical grafting density $\sigma_{crit} = 1/\left(2\sqrt{3}R_F^2\right)$ (i.e., the grafting density σ when the tethered brush size is equal to the inter-tether distance), assuming hexagonal packing with a grafting density σ. In order to estimate the critical grafting density σ_{crit}, we chose hexagonal packing of PEG brushes (because it is a preferred geometry in nature, and it provides a constant inter-brush spacing making the analysis simpler). With a hexagonal packing of PEG brushes (see Fig. 4.4), we estimated the critical grafting density using Eq. 4.1.

$$\sigma_{crit} = \frac{Chains\ per\ unit\ cell}{Area\ of\ unit\ cell} = \frac{3}{\left(6\sqrt{3}R_F^2\right)} = \frac{1}{2\sqrt{3}R_F^2} \quad (4.1)$$

The average Flory radius[2] $R_F = lN^{1/3} \approx 0.58$ nm for PEG brushes with monomer length[3], l = 0.3 nm and number of monomers, N = 6 to 9. The non-dimensional slipperiness factor σ^* at different silanization times t_{sil} are reported in Table 4.1.

Table 4.1. Non-dimensional slipperiness factor σ^* with PEG (6-9 repeating units) at different silanization times t_{sil}.

t_{sil} (min)	h (nm)	σ (chains nm^{-2})	σ^*
0.5	0.15 ± 0.03	0.29	0.34
1	0.19 ± 0.01	0.38	0.44
2	0.33 ± 0.13	0.65	0.77
5	0.43 ± 0.01	0.84	0.99
7	0.59 ± 0.21	1.16	1.37
10	0.65 ± 0.05	1.28	1.51
15	0.84 ± 0.15	1.65	1.95
30	0.93 ± 0.06	1.82	2.15
60	1.01 ± 0.06	1.98	2.34

We characterized surface wettability and slipperiness on SLIC surfaces by measuring contact angles and sliding angles with 20 μL sessile water droplets using a contact angle goniometer/tensiometer (Rame-Hart 260). At least six measurements were performed on each surface at spatially distinct locations. The standard deviation is reported as error with all measurements.

At t_{sil} = 0 min, water droplets completely spread (static contact angle, θ = 0°) and did not slide on hydroxylated silicon wafers. As t_{sil} increased, the dynamic contact angles (i.e., θ_{adv} and θ_{rec}) of water increased (see Fig. 4.5a), indicating increasing covalent grafting of PEG brushes, resulting in increasing σ^*. In addition, as t_{sil} increased, $\Delta\theta$ decreased (see Fig. 4.5b), indicating a decrease in inhomogeneities on the surface as $\sigma^* \rightarrow 1$. At t_{sil} = 7 min, we estimated that $\sigma^* > 1$ for PEG brushes, indicating the onset of maximum and constant slipperiness regime with θ_{adv} = 39°, θ_{rec} = 36°, and $\Delta\theta$ = 3°. For $t_{sil} \geq 7$ min, we obtained SLIC surfaces (see Fig. 4.5c) with nearly constant contact angles and contact angle hysteresis, confirming that $\sigma^* > 1$ signifies a regime of maximum and constant slipperiness.

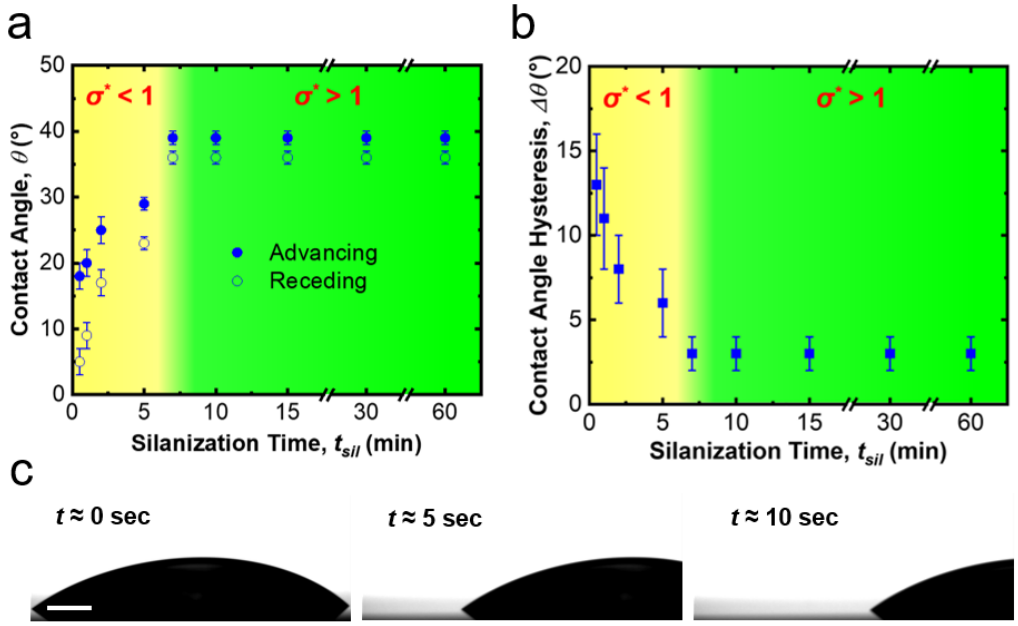

Figure 4.5. Wettability and slipperiness on SLIC surfaces. (a) Advancing and receding contact angles of water on PEG functionalized surfaces at different silanization times, t_{sil}. (b) Contact angle hysteresis of water on PEG functionalized surfaces at different silanization times, t_{sil}. (c) Time-lapse images showing a 20 µl water droplet sliding easily on a titled SLIC surface. The scale bar represents 1 mm.

4.5 Designing SLIC surfaces with $PEG_{9\text{-}12}$

To validate our design criteria for SLIC surfaces, we designed SLIC surfaces using PEG brushes with 9-12 repeating units ($PEG_{9\text{-}12}$, average molecular weight $M \approx 462$ Da), in addition to PEG brushes with 6-9 repeating units ($PEG_{6\text{-}9}$, average molecular weight $M \approx 330$ Da). We fabricated SLIC surfaces by covalently grafting $PEG_{9\text{-}12}$ brushes to hydroxylated smooth silicon wafers using liquid phase silanization (see section 4.3). We systematically tuned the non-dimensional slipperiness factor σ^* by tailoring the silanization time t_{sil} (see Table 4.2). At different t_{sil}, we estimated σ using the PEG layer thickness h obtained from ellipsometry (see section 4.4). Assuming hexagonal packing, we estimated σ_{crit} for $PEG_{9\text{-}12}$ (see section 4.4).

Table 4.2. Non-dimensional slipperiness factor σ^* with PEG (9-12 repeating units) at different silanization times t_{sil}.

t_{sil} (min)	h (nm)	σ (chains nm^{-2})	σ^*
0.5	0.15 ± 0.01	0.21	0.31
1	0.17 ± 0.01	0.24	0.35
2	0.25 ± 0.04	0.35	0.52
5	0.38 ± 0.03	0.53	0.79
7	0.52 ± 0.02	0.73	1.08
10	0.76 ± 0.31	1.06	1.58
15	1.09 ± 0.05	1.53	2.27
30	1.34 ± 0.12	1.88	2.79
60	1.62 ± 0.14	2.27	3.37

As anticipated, at t_{sil} = 0 min, water droplets completely spread and did not slide on hydroxylated silicon wafers. As t_{sil} increased, the dynamic contact angles (θ_{adv} and θ_{rec}) of

water increased (see Fig. 4.6a), indicating increasing covalent grafting of $PEG_{9\text{-}12}$ brushes, resulting in increasing σ^*. Simultaneously, as t_{sil} increased, $\Delta\theta$ decreased (see Fig. 4.6b), indicating a decrease in inhomogeneities on the surface as $\sigma^* \rightarrow 1$. At t_{sil} = 7 min, we estimated $\sigma^* > 1$ for $PEG_{9\text{-}12}$ brushes, indicating the onset of maximum and constant slipperiness regime with θ_{adv} = 39°, θ_{rec} = 36°, and $\Delta\theta$ = 3°. For t_{sil} > 7 min, we obtained SLIC surfaces with nearly constant contact angles and contact angle hysteresis (see Figs. 4.6a & b). Here, it is noteworthy that while the onset of slipperiness did not change between $PEG_{9\text{-}12}$ and $PEG_{6\text{-}9}$, σ^* and σ for $PEG_{9\text{-}12}$ and $PEG_{6\text{-}9}$ are different (see Table S1 and Table S2). This further reaffirms our design criteria for SLIC surfaces ($\sigma^* > 1$).

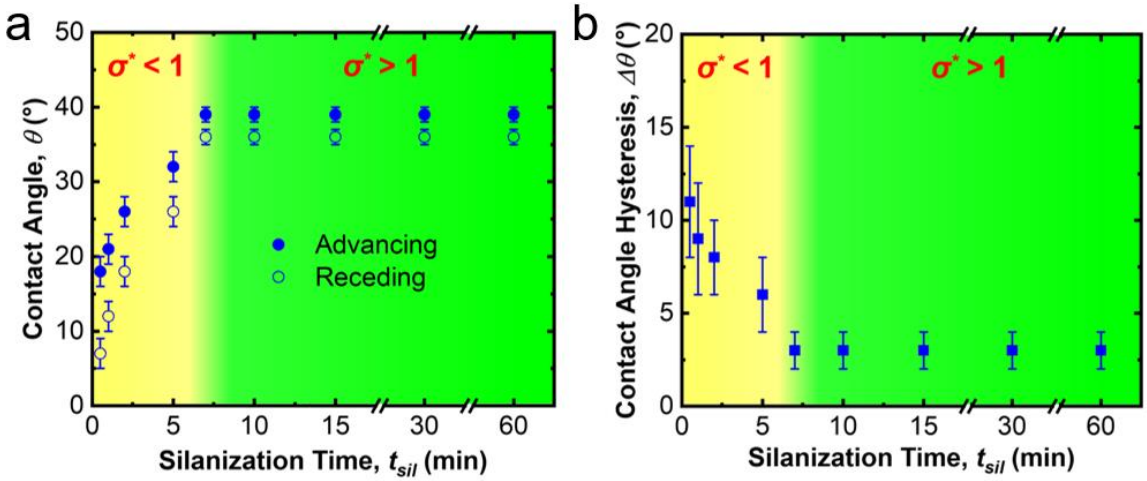

Figure 4.6. Wettability and slipperiness on $PEG_{9\text{-}12}$ functionalized surfaces. (a) Advancing and receding contact angles of water on $PEG_{9\text{-}12}$ functionalized surfaces at different silanization times, t_{sil}. (b) Contact angle hysteresis of water on $PEG_{9\text{-}12}$ functionalized surfaces at different silanization times, t_{sil}.

4.6 SLIC surfaces for thermofluidic applications

In addition to elucidating the underlying design principles and fabricating SLIC surfaces, we evaluated the performance of our SLIC surfaces in relevant thermofluidic applications.

Specifically, our SLIC surfaces are ideal for enhancing condensation heat transfer of aqueous liquids because they simultaneously offer low static contact angle θ and low sliding angle ω (i.e., minimum tilt angle for a droplet to slide on a surface) for aqueous liquids. Low contact angle θ promotes high nucleation rates and low conduction resistance, both of which enhance condensation heat transfer.[3,4,120] Low sliding angle ω (due to low contact angle hysteresis $\Delta\theta$) promotes rapid and efficient removal of the condensate droplets, thereby enabling sustained dropwise condensation with significantly higher heat transfer coefficient compared to filmwise condensation.[3,4,120]

To demonstrate such enhanced condensation heat transfer resulting, we qualitatively compared the condensation of water on our SLIC surfaces ($\theta \approx 37°$, $\omega \approx 3°$ for 20 μL water droplets) with condensation on non-slippery hydrophilic surfaces (having low contact angle, but higher sliding angle) and slippery hydrophobic surfaces (having low sliding angle, but higher contact angle). We used untreated silicon wafers as non-slippery hydrophilic surfaces ($\theta \approx 45°$, $\omega \approx 20°$ for 20 μL water droplets) and 1,3-dichlorotetramethyldisiloxane-treated silicon wafers as slippery hydrophobic surfaces ($\theta \approx 103°$, $\theta_{adv} \approx 104°$, $\theta_{rec} \approx 101°$, $\omega \approx 3°$ for 20 μL water droplets; see experimental procedures). We fabricated slippery hydrophobic surfaces by exposing hydroxylated silicon wafers to the vapors of 150 μL of 1,3-dichlorotetramethyldisiloxane (Gelest) in an enclosed chamber for 15 min at room temperature. Subsequently, the silanized samples were cleaned by rinsing thoroughly with anhydrous toluene, DI water and ethanol (Fisher) sequentially, and then dried with nitrogen.

Water condensation experiments were conducted in a custom-built insulated enclosed chamber equipped with an inlet for steam and a transparent glass window. Steam (at 100°C and 1 atm) was generated by boiling water in a conical flask and was directed to the inlet of enclosed

chamber through insulated pipes for condensation. The substrate was vertically mounted on a Peltier plate set to ambient temperature (≈ 20°C), opposite to the glass window and was exposed to steam inside the enclosed chamber (see Figs. 4.7a, b and c). The condensation process was monitored and recorded through the glass window using a camera.

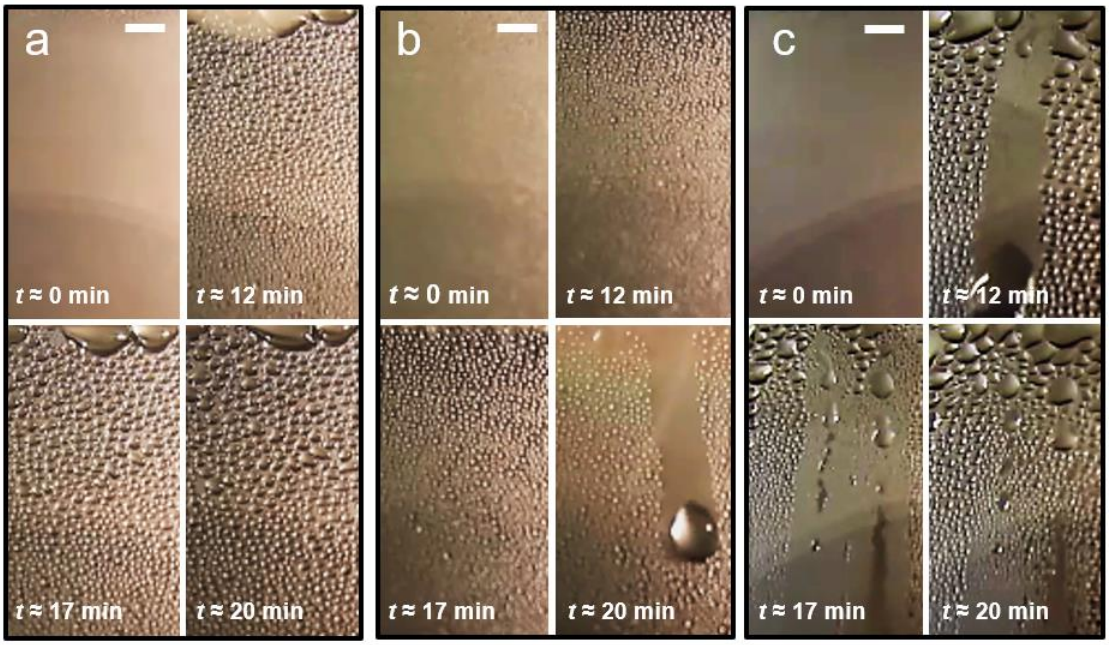

Figure 4.7. Water condensation on SLIC surfaces. (a)-(c) Water droplet nucleation, growth, and coalescence on vertically oriented non-slippery surface, slippery hydrophobic surface and SLIC surface, respectively. The scale bar represents 2 mm on all images.

Our results indicate that the non-slippery hydrophilic surface and SLIC surface displayed faster droplet coalescence and growth due to their higher nucleation rate compared to the hydrophobic slippery surface. Condensate droplets attained a critical size (≈ 1.4 mm; see Fig. 4.7c) and slid down our SLIC surface at a faster rate compared to the hydrophobic slippery surface and the non-slippery hydrophilic surface. This rapid droplet shedding indicates that our SLIC surfaces not only facilitate high nucleation rates due to their hydrophilicity, but also facilitate rapid condensate removal due to their high slipperiness (i.e., low ω). After removal of a

condensate droplet, the nucleation, coalescence, growth, and removal of additional condensate droplets continued on our SLIC surface indicating the potential for sustained dropwise condensation and enhanced condensation heat transfer.

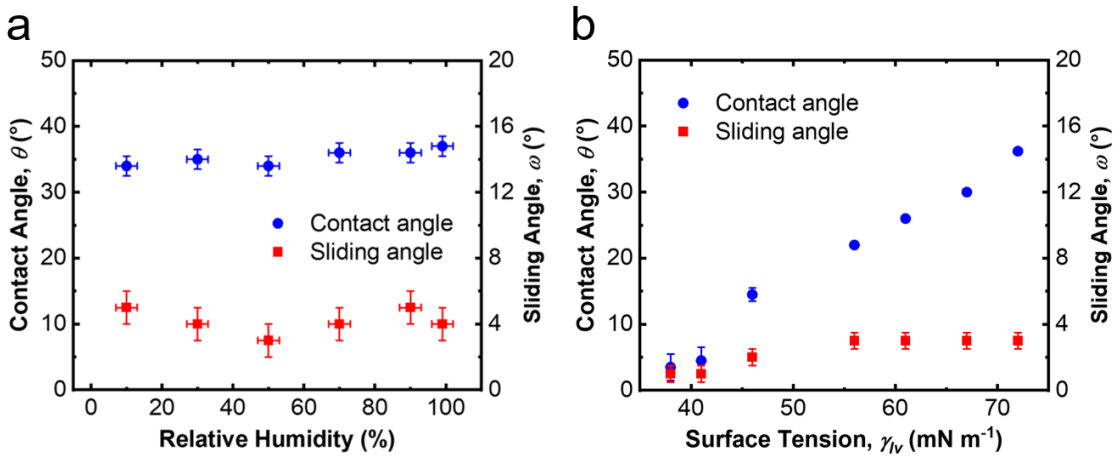

Figure 4.8. Influence of relative humidity and surface tension on SLIC surfaces. (a) Static contact angles and sliding angles of water on SLIC surfaces for different relative humidities. (b) Static contact angles and sliding angles of aqueous liquid droplets with different surface tensions on SLIC surfaces.

In practice, condensation can occur at different relative humidities for a wide range of aqueous liquids. To ensure that our SLIC surfaces retain their hydrophilicity and slipperiness, we characterized their contact angles and sliding angles for water at different relative humidities and for aqueous liquids (solutions of sodium dodecyl sulfate in water) with a wide range of surface tensions (γ_{lv} = 40 mN m^{-1} to 72 mN m^{-1}). Contact angles and sliding angles were measured with 20 μL sessile droplets and surface tension was measured with pendant droplets, using a contact angle goniometer/tensiometer (Rame-Hart 260). A custom-built humidity chamber was used to control the humidity. At least six measurements were performed on each surface at spatially distinct locations. The standard deviation is reported as error with all measurements.

Our SLIC surfaces displayed negligible change in static contact angles and sliding angles of water at relative humidities ranging from 10% to 100% (see Fig. 4.8a). As the surface tension of aqueous liquids decreased from 72 mN m^{-1} to 40 mN m^{-1}, our SLIC surfaces displayed an expected decrease in static contact angles and sliding angles (see Fig. 4.8b). In addition to experimentally measuring the sliding angles of different aqueous liquid droplets on SLIC surfaces, we also estimated the sliding angles ω based on a balance between work done by gravitational force and work expended due to adhesion as:[4]

$$\sin\omega \approx \frac{\gamma_{lv} D_{TCL}(\cos\theta_{rec} - \cos\theta_{adv})}{\rho g V} \tag{4.2}$$

Here, γ_{lv}, ρ and V are surface tension, density, and volume of the liquid droplet, respectively, g is the acceleration due to gravity, θ_{adv} and θ_{rec} are the advancing and receding contact angles, respectively, and D_{TCL} is the width of the triple phase contact line perpendicular to the droplet sliding direction. Assuming the droplet is a spherical cap, width of the triple phase contact line was calculated as:

$$D_{TCL} = 2\sin\bar{\theta}\left[\frac{3V}{\pi(2 - 3\cos\bar{\theta} + \cos^3\bar{\theta})}\right]^{\frac{1}{3}} \tag{4.3}$$

Here, $\bar{\theta}$ is the average contact angle, given as:

$$\cos\bar{\theta} = \frac{(\cos\theta_{adv} + \cos\theta_{rec})}{2} \tag{4.4}$$

The estimated sliding angles for 20 μL droplets of SDS in water solutions on SLIC surfaces were obtained using Eq. 4.2-4.4 and reported in Table 4.3. These results demonstrate the retention of hydrophilicity and slipperiness of our SLIC surfaces and their potential for condensation applications.

Table 4.3. Estimated and measured sliding angles of SDS solutions on SLIC surfaces.

γ_{lv} (mN m^{-1})	$\omega_{\text{estimated}}$ (°)	ω_{measured} (°)
72	4.4	3
67	3.6	3
61	3.1	3
56	2.5	3
46	2.2	2
41	1.2	1
38	1.1	1

In addition, we investigated the durability (i.e., retention of hydrophilicity and slipperiness) of our SLIC surfaces after prolonged exposure to air, immersion in water, exposure to steam (at 100°C and 1 atm), and water droplets (30 μL) sliding past the surface. We measured the advancing and receding contact angles as well as the sliding angles periodically to assess the hydrophilicity and slipperiness.

Our results indicated no change in advancing and receding contact angles and sliding angles on SLIC surfaces even after exposure to air for 20 days (see Fig. 4.9a), immersion in water for 20 days (see Fig. 4.9b), exposure to steam for a cumulative time of 48 hours (see Fig. 4.9c) with dropwise condensation and 100,000 water droplets sliding past the surface (see Fig. 4.9d). While these results demonstrate the potential of SLIC surfaces, a more comprehensive and application-specific determination of durability is needed for lasting use in themofluidic and biofluidic applications.

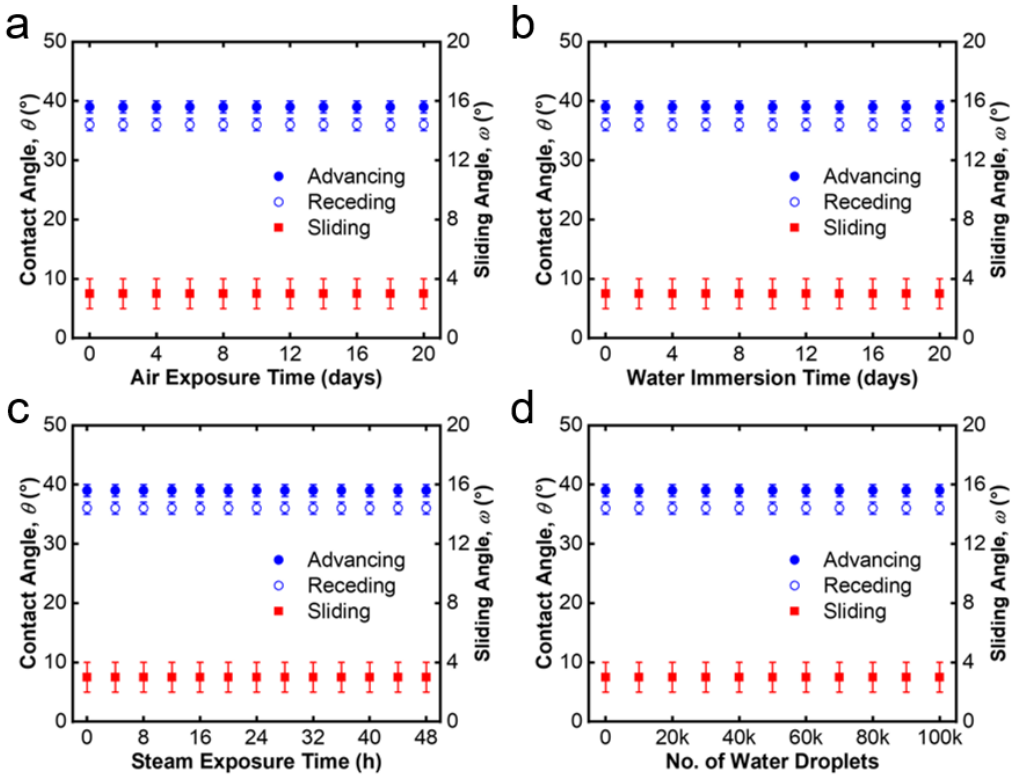

Figure 4.9. Durability of SLIC surfaces. (a), (b), (c) and (d) Advancing and receding contact angles and sliding angles of water on a SLIC surface as a function of air exposure time, water immersion time, steam exposure time and number of water droplets sliding past the surface, respectively.

4.7 SLIC surfaces for biofluidic applications

In addition to thermofluidic applications, we also evaluated the performance of our SLIC surfaces in biofluidic applications. Specifically, our SLIC surfaces are ideal for fouling-resistant lab-on-a-chip miniature platforms because they simultaneously offer hydrophilicity and slipperiness for aqueous liquids. Hydrophilicity imparted by the PEG brushes allows improved resistance to fouling by proteins because of the hydration layer and the steric hindrance.[121-124] To demonstrate the fouling-resistance of our SLIC surfaces, we compared them with that of non-slippery hydrophilic surfaces and slippery hydrophobic surfaces. We used untreated glass

coverslips as non-slippery hydrophilic surfaces ($\theta \approx 53°$, $\omega \approx 47°$ for 20 μL water droplets), 1,3-dichlorotetramethyldisiloxane-treated glass coverslips as slippery hydrophobic surfaces ($\theta \approx 103°$, $\omega \approx 4°$ for 20 μL water droplets) and glass coverslips with covalently grafted PEG brushes as our SLIC surfaces ($\theta \approx 37°$, $\omega \approx 5°$ for 20 μL water droplets). We used glass coverslips because they are smooth (allowing low physical inhomogeneity) and transparent (allowing light microscopy).

We exposed the surfaces to fibrinogen solution and studied protein adsorption in-situ using total internal reflection fluorescence (TIRF) microscopy. TIRF microscopy was conducted using time-lapse imaging with fibrinogen from human plasma conjugated to Alexa Fluor 647 (Fisher). The time-lapse imaging was conducted using a custom-built microscope[48] equipped with Olympus IX71 body, 100x objective and a CRISP ASI autofocus system. The excitation was conducted using a 638 nm laser (DL638-328 050, CrystaLaser, Reno, NV). Emission was collected using the appropriate Semrock bandpass filters and the images were acquired in a water-cooled, back-illuminated EMCCD camera (iXon DU-888, Andor, Belfast, UK) liquid-cooled to -70°C with an electronic gain of 60. An enzymatic oxygen scavenging system was used in the imaging buffer to reduce photobleaching.[49] Imaging buffer consisted of 50 mM Tris-HCl (pH 8.0), 10 mM NaCl, 0.15 mg ml^{-1} glucose oxidase, 34 mg ml^{-1} catalase, 0.8% (w/v) glucose and 1% (v/v) b-mercaptoethanol. On SLIC surfaces, time-lapse imaging was conducted at a frame rate of 30 frames hr^{-1}. On other surfaces, the time-lapse imaging was conducted at a frame rate of 10 frames s^{-1}. During imaging, the concentration of fibrinogen was maintained at 5 nM for all experiments.

Our results from TIRF microscopy indicate that the fibrinogen adsorbed within 1 min on both the non-slippery hydrophilic surfaces and slippery hydrophobic surfaces (see Figs. 4.10a

and 4.10b). In contrast, our SLIC surfaces displayed exceptional fouling-resistance by preventing adsorption of fibrinogen even at 1800 min (see Fig. 4.10c).[125,126] The exceptional fouling-resistance is possibly due to an ice-like hydration layer,[117,118,122] but a comprehensive study is needed to develop a mechanistic understanding.

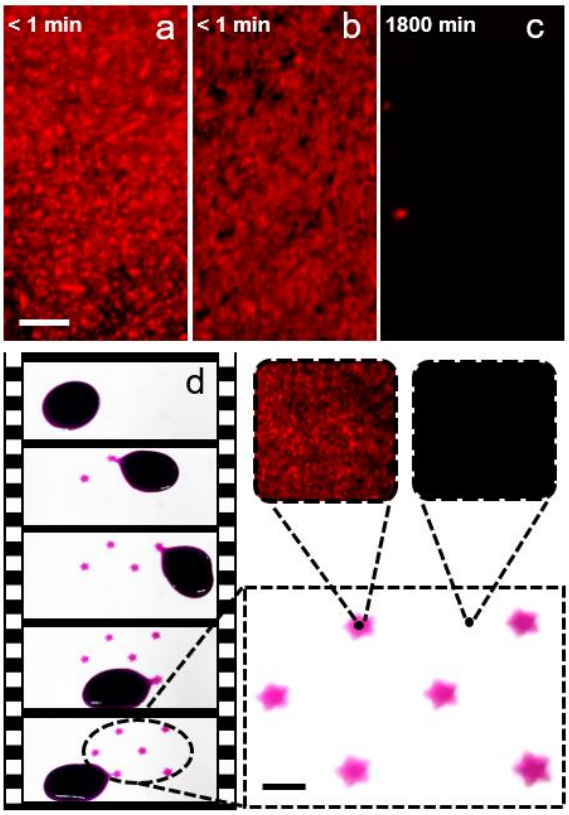

Figure 4.10. Fouling resistance on SLIC surfaces. (a) Fluorescent microscopy image showing significant adsorption of fibrinogen (red) on non-slippery hydrophilic surface (surface coverage ≈ 96%) within 1 min. The scale bar on represents 5 μm on all fluorescent images. (b) Fluorescent microscopy image showing significant adsorption of fibrinogen (red) on slippery hydrophobic surface (surface coverage ≈ 93%) within 1 min. (c) Fluorescent microscopy image showing negligible adsorption of fibrinogen (red) on SLIC surface (surface coverage ≈ 0.2%) even at 1800 min. (d) Time-lapse images showing tiny volumes of water (pink) trapped in non-slippery domains (star-shaped) domains on the SLIC surface. The scale bar represents 1 mm.

In addition to the outstanding fouling-resistance, the slipperiness of our SLIC surfaces allows aqueous droplets to slide easily (see Fig. 4.10d), allowing manipulation of aqueous droplets. To demonstrate the utility of slipperiness in lab-on-a-chip miniature platforms, we fabricated SLIC surfaces patterned with an array of non-slippery domains. Star-shaped non-slippery domains were fabricated on SLIC surfaces via laser ablation with a commercially available, quasi-continuous CO_2 laser system with a central wavelength of 10.6 mm (Epilog Legend 36EXT). Laser ablation increased the roughness (i.e., physical inhomogeneity) resulting in loss of slipperiness in the domains. When an aqueous droplet (e.g., protein solution) slides past such patterned SLIC surfaces, tiny volumes of the droplet are trapped in the non-slippery domains due to higher adhesion (see Fig. 4.10d). In this manner, on patterned SLIC surfaces, biological analytes (e.g., proteins, nucleic acids, cells, microorganisms etc.) can be trapped in targeted domains, while ensuring that the remaining areas fouling-free (see Fig. 4.10d).

Furthermore, while aqueous droplets slide easily, oil droplets adhere to our SLIC surfaces. This can further facilitate oil (lipid)-water separations on SLIC surfaces. When a compound droplet, consisting of water and oil, is placed on a tilted SLIC surface, water displaces oil and slides away while the oil remains adhered (see Figs. 4.11a, b & c), indicating the potential of SLIC surfaces for biofluidic separations.

In addition, we conducted energy analysis for a compound droplet on SLIC surfaces to ensure that water displaces oil on SLIC surfaces for an efficient oil-water separation. For this, we determined the surface energy $\gamma_{sv} = \gamma_{sv}^{p} + \gamma_{sv}^{d}$ = 22 mN m^{-1} + 44 mN m^{-1} = 66 mN m^{-1} using the Owens-Wendt analysis[5], with water (polar liquid) and methylene iodide (non-polar liquid) as probe liquids.

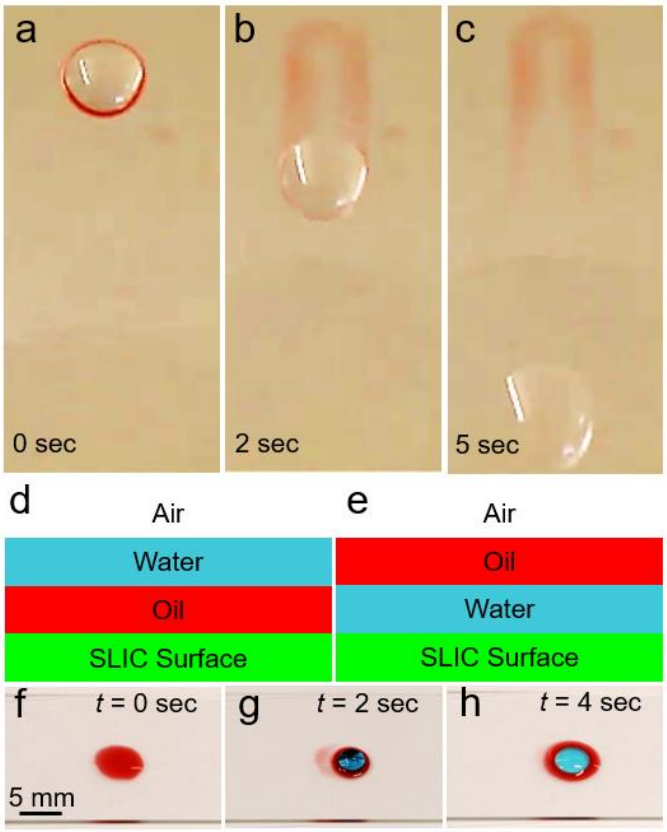

Figure 4.11. Oil-water separation on SLIC surfaces. (a)-(c) Time-lapse images showing the separation of water (colorless) from hexadecane (red) using a compound (water + hexadecane) droplet. (d) & (e) Schematics showing the configurations of a SLIC surface with oil displacing water and water displacing oil, respectively. (f)-(h) Time-lapse images showing water (blue) displacing hexadecane (red) on a SLIC surface.

To separate a compound droplet of water and oil using our SLIC surfaces, water must displace oil from the SLIC surface so that it can slide away while leaving the oil adhered. To determine whether or not water displaces oil from the SLIC surface, we compared the energy of two configurations (see Figs. 4.11d & e) – oil displacing water on a SLIC surface (with energy $E_1 = \gamma_{so} + \gamma_{ow} + \gamma_{wv}$) and water displacing oil on a SLIC surface (with energy $E_2 = \gamma_{sw} + \gamma_{ow} + \gamma_{ov}$). Here, water surface tension $\gamma_{wv} = \gamma_{wv}^{p} + \gamma_{wv}^{d}$ = 51 mN m^{-1} + 21 mN m^{-1} = 72 mN m^{-1} and hexadecane (oil) surface tension $\gamma_{ov} = \gamma_{ov}^{d}$ = 27.5 mN m^{-1}. As postulated by Fowkes[6], we

estimated $\gamma_{so} = \gamma_{sv} + \gamma_{ov} - 2\sqrt{\gamma_{sv}^{d}\,\gamma_{ov}^{d}}$ = 24 mN m^{-1} and $\gamma_{ow} = \gamma_{ov} + \gamma_{wv} - 2\sqrt{\gamma_{ov}^{d}\,\gamma_{wv}^{d}}$ = 51 mN m^{-1}. As postulated by Owens and Wendt[5], we estimated $\gamma_{sw} = \gamma_{sv} + \gamma_{wv} - 2\sqrt{\gamma_{sv}^{d}\,\gamma_{wv}^{d}} - 2\sqrt{\gamma_{sv}^{p}\,\gamma_{wv}^{p}}$ = 10 mN m^{-1}. This energy analysis shows E_2 = 89 mN m^{-1} < E_1 = 133 mN m^{-1}, indicating water indeed displaces oil from SLIC surfaces (see Figs. 4.11f, g & h).

4.8 Conclusions

In this work, we elucidated the design of non-textured, all-solid, slippery hydrophilic surfaces. We demonstrated two distinct regimes of slipperiness: $\sigma^* < 1$, where slipperiness increases with increasing grafting density, and $\sigma^* \geq 1$, where slipperiness is maximum and constant. We postulate that $\sigma^* > 1$ is a prudent criterion for the design of non-textured, all-solid, slippery hydrophilic surfaces. Building on this design criterion, we fabricated slippery hydrophilic (SLIC) surfaces by covalently grafting PEG brushes to silicon wafers and glass coverslips. We demonstrated the exceptional performance of our SLIC surfaces in condensation and fouling-resistance compared to non-slippery hydrophilic and slippery hydrophobic surfaces. While a comprehensive study (on processing-structure relationships with a wide variety of chemistries and substrates and the role of ice-like hydration layers) is needed to develop a thorough understanding of this emerging class of surfaces, our results indicate that SLIC surfaces have the potential to positively transform the technological landscape of thermofluidic and biofluidic devices.

CHAPTER 5. INTERACTION OF BLOOD WITH SLIPPERY SURFACES

5.1 Introduction

Blood-material interactions on slippery surfaces (i.e., surfaces that display high liquid droplet mobility) have received significant attention because of their advantages in multiple biofluidic applications.[127-131] Particularly, in blood-contacting biomedical devices, blood coagulation on the device leads to thrombosis and inflammation.[132-135] These can further disrupt the functionality of the device resulting in either lower performance or failure of the device.[7,136] In our prior work, we emphasized that non-textured, all-solid slippery hydrophilic (SLIC) surfaces are an emerging class of slippery surfaces and demonstrated that SLIC surfaces can significantly reduce fibrinogen adsorption (i.e., one of the first steps in the blood-coagulation cascade) compared to non-textured non-slippery hydrophilic surfaces and non-textured slippery hydrophobic surfaces using TIRF microscopy.[137] Building on our prior work, in this study, we investigated the interactions of blood components (i.e., fibrinogen, platelets & leukocytes) with slippery surfaces using glass and PDMS substrates.

Based on our results, slippery surfaces demonstrate lower fibrinogen adsorption and platelet and leukocyte adhesion compared to non-slippery surfaces. Specifically, SLIC surfaces display significantly lower fibrinogen adsorption (99.5% lower surface coverage) and platelet and leukocyte adhesion (91.8% and 99.4% lower surface coverage, respectively) compared to untreated glass slides. SLIC surfaces also display lower fibrinogen adsorption (47% lower surface coverage) and platelet and leukocyte adhesion (86.2% and 97.5% lower surface coverage, respectively) compared to slippery PDMS. While a comprehensive study (on blood-material interactions with different proteins and blood cells at longer incubation times with a wide variety of chemistries and substrates) is needed to develop a thorough understanding of the

influence of slipperiness, our results indicate that SLIC surfaces can reduce protein adsorption (i.e., fibrinogen) and blood cell (platelets & leukocytes) adhesion. We envision that our study will encourage more investigations on blood-material interactions on slippery surfaces for developing improved biomedical devices with reduced risk of thrombosis.

5.2 Blood-material interactions

Blood-contacting medical devices (e.g., body implants, catheters, heart valves, stents, ventricular assist devices etc.) have saved millions of patients improving health and quality of human lives.[8,138,139] Despite their extensive use, these devices are prone to thrombosis and infections causing inflammation, pain, and discomfort to the patient.[73,134,140] This results in further complications with the device function, leading to its failure imposing a severe risk to the patient.[8,135] The common practices to reduce thrombosis on medical devices include coating the device with anti-coagulant materials like heparin and antiplatelet therapies.[141-143] However, these practices increase the risk and cost to the patient.[144,145] Moreover, such antiplatelet therapies can underperform in dynamic blood flow conditions and increase the risk of bleeding to the patient.[146,147] Therefore, it is important to understand the mechanisms of blood-material interactions on solid surfaces for designing novel coatings for biomedical devices that can reduce thrombosis and inflammation.

When blood comes in contact with a foreign solid surface, blood plasma proteins like fibrinogen and von Willebrand Factor (VWF) start adsorbing on the surface.[73] These proteins further facilitate the adhesion of platelets, which are inert cells that travel through blood circulation.[134] Typically, fibrinogen acts as a primary protein leading to platelet adhesion at lower wall shear rates ($< 600\ s^{-1}$) whereas VWF plays a major role at higher wall shear rates.[8] On the other hand, human serum albumin, the most abundant protein in blood plasma that is

relatively inert to platelets, competes with fibrinogen and VWF in adsorbing on to the substrate and lowers platelet adhesion.[148,149] However, once platelets adhere to the surface, they can be activated by the surrounding proteins depending on their configuration. Platelet activation can be characterized by the distorted shape of platelets from discoid to an spherical form with protrusions.[150,151] This may also change the conformation of integrins on platelets, which increases their affinity to bind with fibrinogen.[152] Furthermore, the release of α-granules from platelets exposes the membrane-bound proteins releasing other agents (e.g., platelet activation agonists, VWF etc.) from platelets activating the platelets in the surroundings.[153] This enhanced platelet activation is amplified by platelet-platelet binding resulting in platelet aggregation. This prothrombotic state can also further escalate to procoagulant state with enough platelet activation and aggregation.

At low shear rates, the coagulation cascade occurs simultaneously with fibrin formation.[154] Thrombin, an enzyme that is generated on activated platelets, can form fibrin monomers by cleaving fibrinogen.[74] These fibrin monomers assemble to form protofibrils, which further polymerize to form a cross-linked network of fibrin gel.[154] Here, it is important to note that the fibrin formation is a more complicated process, which depends on the mass transport and other conditions like coagulant state, cellular activity, and fibrinolysis.[155] Nonetheless, fibrin formation assists thrombosis and the consequent inflammation.

Once the platelets adhere to the surface, they can trigger immune response by recruiting leukocytes (e.g., neutrophils, monocytes, lymphocytes etc.), which act against foreign bodies inside the human body.[140] This can further lead to leukocyte migration and activation resulting in inflammation. A toll-like receptor 4 found on platelets can trigger the formation of neutrophil extracellular traps (NETs) that consists of a network of DNA fibers, which can trap microbes.[156]

NETs can also stimulate thrombus formation by capturing platelets within their DNA fiber mesh.[157] Monocytes (the largest leukocytes) can provide signals for other cells promoting their activation and adhesion on the surface by releasing inflammatory cytokines and chemokines.[158] This further results in acute inflammation, which can develop into chronic inflammation and consequently, promoting monocyte differentiation into macrophages and intercellular communication leading to cell apoptosis.[159] These events can also lead to the infiltration of lymphocytes and fibroblasts from the surrounding tissue.[160] In addition, the cytokines can also enhance or retard intracellular function, intercellular communication, and extracellular matrix deposition by binding themselves to cell surface receptors.[161] This can further trigger a foreign body reaction and fibrosis isolating the foreign body through fibrous encapsulation. This response further impedes the tissue integration with the foreign body, consequently, can result in an undesirable rejection of the foreign body.

In our prior work, we demonstrated significantly delayed fibrinogen adsorption (i.e., one of the first steps in blood-coagulation cascade) on an emerging class of SLIC surfaces compared non-slippery hydrophilic and slippery hydrophobic surfaces. Inspired by these results, in this work, we attempted to understand the blood-material interactions by investigating platelet and leukocyte adhesion, in addition to fibrinogen adsorption on slippery surfaces. Based on our prior results, we anticipate that the slippery surfaces have the potential to minimize the blood-surface interactions by hindering the subsequent steps in the blood-coagulation cascade (due to their lower fibrinogen adsorption), possibly resulting in lower thrombosis.

5.3 Fabrication of slippery surfaces

In this work, we fabricated slippery substrates using glass slides and polydimethylsiloxane (PDMS). We chose glass and PDMS as our substrates because they are

used in several biomedical applications. Moreover, they are transparent and allow light (fluorescence) microscopy. We imparted slipperiness to the glass slides by covalently attaching short chain PEG brushes (9-12 repeating units) onto hydroxylated glass slides via liquid phase silanization.[137] To covalently graft PEG brushes, first, the glass slides (Fisher Scientific) were cleaned by rinsing thoroughly with acetone (Fisher Scientific) and DI water, and then dried with nitrogen. The cleaned glass slides were exposed to oxygen plasma (Plasma Etch PE-25) for 10 min for hydroxylation. Subsequently, the hydroxylated samples were immersed in a solution consisting of 2 μL of 2-methoxy polyethyleneoxy (9-12) propyl trimethoxysilane (Gelest) and 12 μL hydrochloric acid (Fisher Scientific) in 45 mL of anhydrous toluene (Fisher Scientific) overnight at room temperature. Finally, the silanized samples were cleaned by rinsing thoroughly with anhydrous toluene, DI water and ethanol (Fisher Scientific) sequentially, and then dried with nitrogen.

We fabricated PDMS substrates by casting PDMS (Silicones, Inc.) with base and curing agents in the ratio of 10:1. The PDMS was then degassed and cured at 70°C for 1 hour in a vacuum oven. The cured PDMS was then peeled off and cut into the desired size for biological experiments. Slippery PDMS was fabricated by adding 50% silicone oil (trimethyl terminated PDMS) by weight to the PDMS base and curing agent mixture. The polymer solution was mixed thoroughly before casting and degassing. The PDMS+50% silicone oil solution was later cured at 70°C for 1 hour before its use.

We characterized the surface wettability and slipperiness of our substrates by measuring advancing and receding contact angles and sliding angles using a contact angle goniometer (Rame-Hart 260). All sliding angles were measured with 20 μL liquid droplets. At least three measurements were performed on each substrate and the average value is reported. The error

with all contact angles and sliding angles is ± 2°. As anticipated, both glass slides and SLIC coating on glass slides displayed advancing contact angles < 90° indicating their hydrophilic nature and the PDMS and slippery PDMS displayed advancing contact angles > 90° indicating their hydrophobic nature (see Table 5.1). SLIC coating and PDMS+50% silicone oil also displayed low sliding angles (i.e., < 10°) indicating their slipperiness.

Table 5.1. Contact angles and sliding angles of water on our surfaces.

Substrate	Advancing contact angle (°)	Receding contact angle (°)	Sliding angle (°)
Glass slide	55	30	24
SLIC on glass	41	35	4
PDMS	121	82	43
Slippery PDMS	106	97	8

5.4 Characterizing fibrinogen adsorption and platelet and leukocyte adhesion

We characterized fibrinogen adsorption and platelet and leukocyte adhesion by quantifying the area of adhesion on our surfaces (i.e., surface coverage) using fluorescent microscopy. Fibrinogen labeled with Alexa Fluor 488 (20 mg ml^{-1}, Fib3 Fibrinogen with fibronectin, von Willebrand Factor, and Factor XIII depleted, Enzyme Research Laboratories) was diluted to 2 mg ml^{-1} for protein adsorption studies. Platelet-rich plasma (PRP) was obtained by centrifuging whole blood to remove erythrocytes. Platelets were stained with Vybrant Dil 546 stain and leukocytes were stained using 4,6–diamidino–2–phenylindole (DAPI) for platelet and leukocyte adhesion studies (courtesy Dr. Nellenbach, Professor Brown's research group at North Carolina State University).

Firstly, the substrates were cleaned using ethanol and dried using air. 100 μL of the desired solution (i.e., fibrinogen and PRP) was placed on the substrate and incubated in dark for 1 hour at room temperature. Subsequently, 500 μL of phosphate buffered saline (PBS) was added to fibrinogen/PRP and aspirated after every 5 minutes two times with a subsequent addition of PBS. The substrates were rinsed gently by running 1 mL PBS down the surface to remove any non-adherent proteins/cells. The adhered proteins/cells were fixed with 10 μL of hydromount and imaged using a fluorescence microscope. All fluorescent images were processed using ImageJ software and the reported surface coverage is the average value from at least 3 different locations on the substrate.

5.5 Fibrinogen adsorption on glass & PDMS substrates

We characterized fibrinogen adsorption on glass and PDMS substrates by incubating fibrinogen labeled with Alexa Fluor 488 (green dye) for 1 hour and imaging using a fluorescence microscope. Subsequently, using the fluorescent images, we determined the surface area covered with fibrinogen using ImageJ. Our fluorescent images on glass substrates qualitatively showed lower fibrinogen adsorption on SLIC coating compared to the untreated glass slide (see Fig. 5.1a & b). Similarly, our fluorescent images on PDMS substrates qualitatively indicated lower fibrinogen adsorption on slippery PDMS (i.e., PDMS+50% silicone oil) compared to the neat PDMS (see Figs. 5.1c & d). However, the difference in fibrinogen adsorption on PDMS substrates is not as significant as that on glass substrates at 1 hour incubation time. Correspondingly, our quantitative analysis using ImageJ on glass substrates indicated a 99.5% lower fibrinogen adsorption (i.e., surface coverage) on SLIC coating compared to the untreated glass slide (see Fig. 5.1e). Similarly, our quantitative analysis using ImageJ on PDMS substrates indicated a 90.3% lower fibrinogen adsorption on slippery PDMS compared to neat PDMS (see

Fig. 5.1f). Furthermore, compared to the slippery PDMS, the SLIC coating showed a 47% lower fibrinogen adsorption.

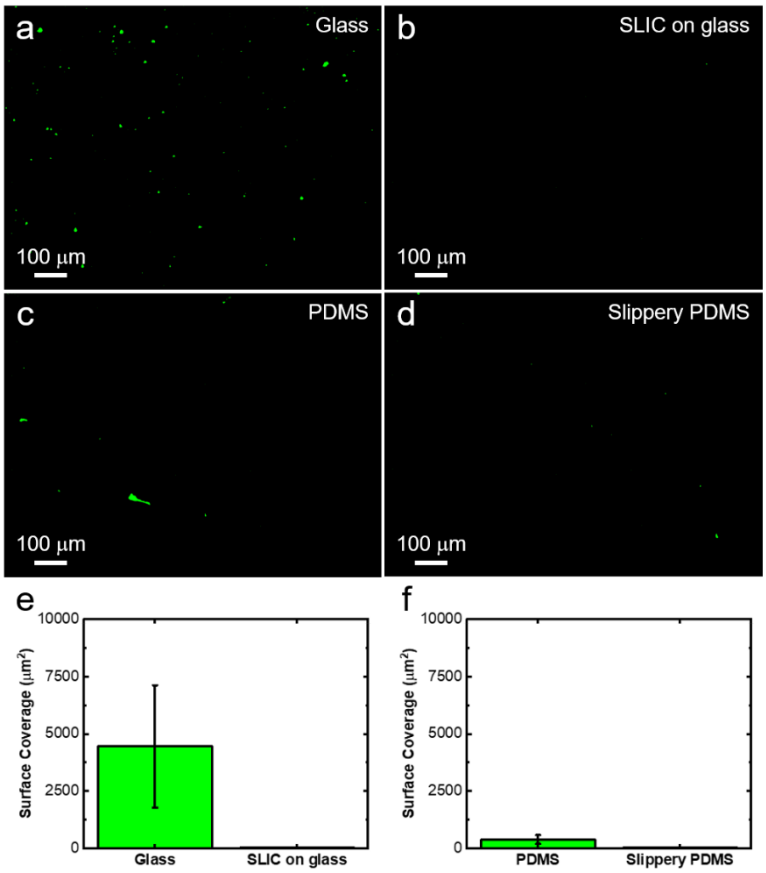

Figure 5.1. Fibrinogen adsorption on glass & PDMS substrates. (a)-(d) False-colored fluorescent images showing adsorbed fibrinogen (green) on glass, slippery glass (SLIC), PDMS and slippery PDMS surfaces, respectively, after 1 hour incubation. (e)-(f) Plots showing lower fibrinogen adsorption (i.e., lower surface coverage) on SLIC coating and slippery PDMS.

We also performed statistical analysis on our surface coverage data for fibrinogen adsorption on all our samples (glass, SLIC on glass, PDMS & slippery PDMS) using one-way analysis of variance (ANOVA) with a 95% confidence interval and our analysis indicated that the sample means are significantly different with a p-value of 0.02. These results further confirm that the slippery substrates can display higher fouling resistance with fibrinogen compared to

their non-slippery counterparts. Specifically, SLIC surfaces can display a significantly lower fibrinogen adsorption. However, more experiments for fibrinogen adsorption on slippery surfaces (SLIC and slippery PDMS surfaces) at longer incubation times are necessary to better understand the fouling resistance, which is crucial for reducing thrombosis. Furthermore, additional experiments for fibrinogen adsorption on slippery surfaces with other surface chemistries will help in understanding the influence of slipperiness and surface chemistry on fouling resistance.

5.6 Platelet & leukocyte adhesion on glass & PDMS substrates

We characterized platelet adhesion on glass and PDMS substrates by incubating PRP for 1 hour and imaging using a fluorescence microscope. Platelets were stained with Vybrant Dil 546 (red dye) for fluorescence imaging. Subsequently, using the fluorescent images, we determined the surface area covered with adhered platelets using ImageJ. Our fluorescent images on glass substrates qualitatively showed lower platelet adhesion on SLIC coating compared to the untreated glass slide (see Figs. 5.2a & b). Our fluorescent images on PDMS substrates qualitatively indicated lower platelet adhesion on slippery PDMS (i.e., PDMS+50% silicone oil) compared to the neat PDMS (see Figs. 5.2c & d). Correspondingly, our quantitative analysis using ImageJ on glass substrates indicated a 91.8% lower platelet adhesion (i.e., surface coverage) on SLIC coating compared to the untreated glass slide (see Fig. 5.2e). Similarly, our quantitative analysis using ImageJ on PDMS substrates indicated a 68.7% lower platelet adhesion on slippery PDMS compared to the neat PDMS (see Fig. 5.2f). However, the PDMS substrates also displayed a large error (i.e., standard deviation) in platelet adhesion. Furthermore, compared to slippery PDMS, SLIC coating showed an 86.2% lower platelet adhesion.

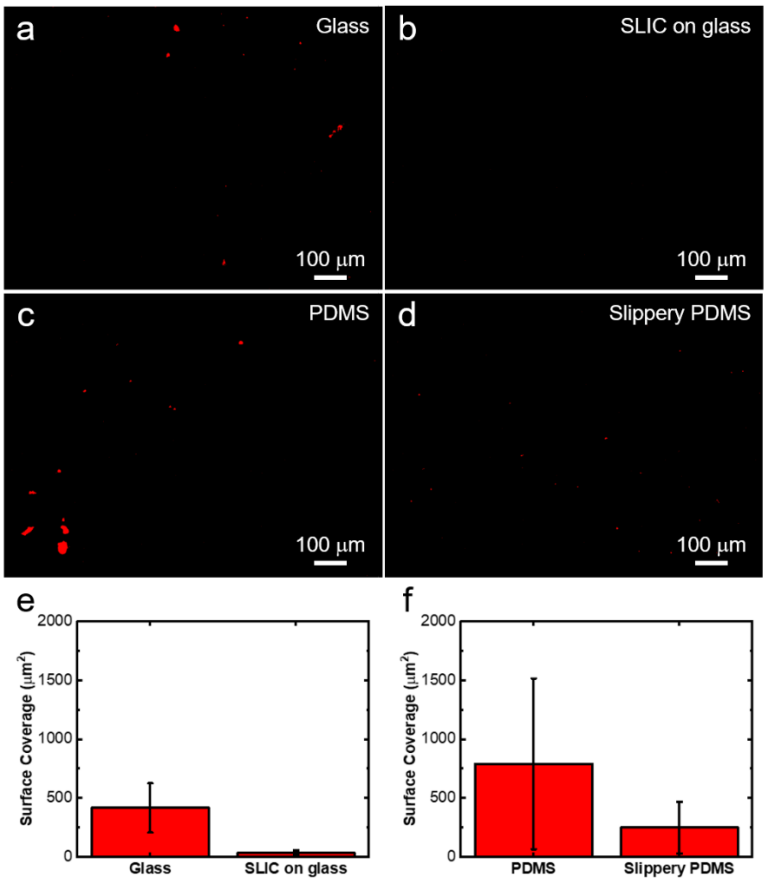

Figure 5.2. Platelet adhesion on glass & PDMS substrates. (a)-(d) False-colored fluorescent images showing adsorbed platelets (red) on glass, slippery glass (SLIC), PDMS and slippery PDMS surfaces, respectively, after 1 hour incubation. (e)-(f) Plots showing lower platelet adhesion (i.e., lower surface coverage) on SLIC coating and slippery PDMS.

We also performed statistical analysis on our surface coverage data for platelet adhesion on all our samples (glass, SLIC on glass, PDMS & slippery PDMS) using one-way ANOVA with a 95% confidence interval and our analysis indicated that the sample means are not significantly different with a p-value of 0.33. Even though the mean values of platelet adhesion for slippery substrates are lower compared to their non-slippery counterparts, our statistical analysis indicated that they are not significantly different. This could be due to the large error in platelet adhesion, especially on PDMS substrates and small sample sizes (n = 3). This implies

that more experiments for platelet adhesion, especially on PDMS substrates, are required to make any logical conclusion about differences in platelet adhesion on slippery vs. non-slippery substrates. Moreover, additional experiments on slippery surfaces with longer incubation times and other surface chemistries will help in understanding the influence of slipperiness and surface chemistry on platelet adhesion, which is crucial for reducing thrombosis.

We characterized leukocyte adhesion on glass and PDMS substrates by incubating PRP for 1 hour and imaging using a fluorescence microscope. Leukocytes were stained with DAPI (blue dye) for fluorescence imaging. Subsequently, using the fluorescent images, we determined the surface area covered with adhered leukocytes using ImageJ. Our fluorescent images on glass substrates qualitatively showed lower platelet adhesion on SLIC coating compared to the untreated glass slide (see Figs. 5.3a & b). Similarly, our fluorescent images on PDMS substrates qualitatively indicated lower platelet adhesion on slippery PDMS (i.e., PDMS+50% silicone oil) compared to neat PDMS (see Figs. 5.3c & d). Correspondingly, our quantitative analysis using ImageJ on glass substrates indicated a 99.4% lower leukocyte adhesion (i.e., surface coverage) on SLIC coating compared to the untreated glass slide (see Fig. 5.3e). Similarly, our quantitative analysis using ImageJ on PDMS substrates indicated a 71.8% lower leukocyte adhesion on slippery PDMS compared to the neat PDMS (see Fig. 5.3f). Furthermore, compared to slippery PDMS, SLIC coating showed a 97.5% lower leukocyte adhesion. We also performed statistical analysis on our surface coverage data for leukocyte adhesion on all our samples (glass, SLIC on glass, PDMS & slippery PDMS) using one-way ANOVA with a 95% confidence interval and our analysis indicated that the sample means are significantly different with a p-value of 0.0005. These results demonstrate that the slippery substrates can display lower leukocyte adhesion compared to their non-slippery counterparts while simultaneously highlighting the performance

of SLIC surfaces in reducing leukocyte adhesion. However, more experiments for leukocyte adhesion on slippery surfaces with other surface chemistries and at longer incubation times are required to better understand the leukocyte adhesion, which is crucial for reducing thrombosis.

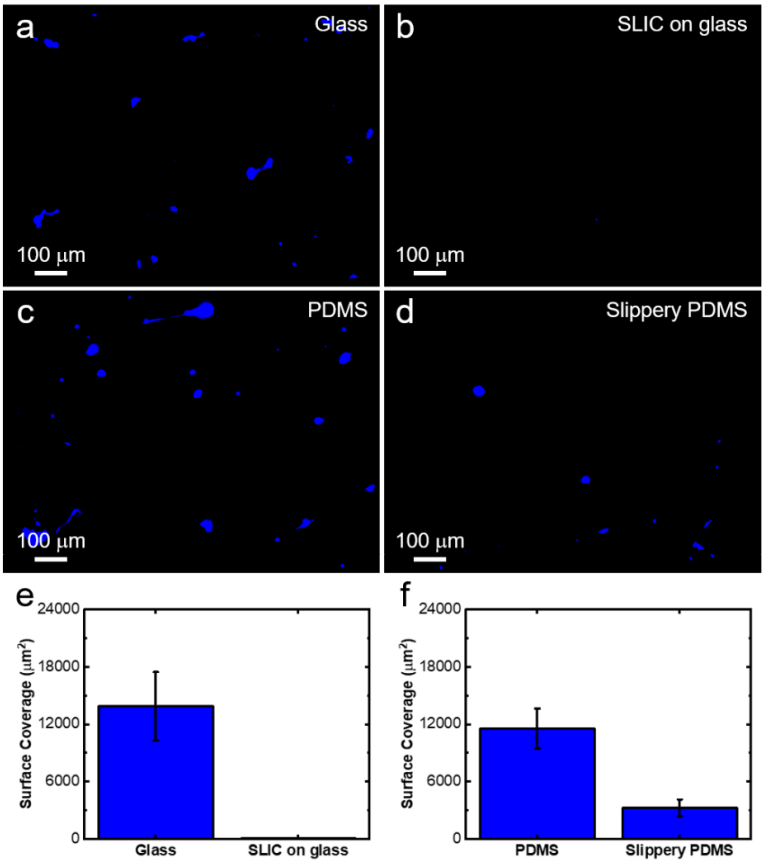

Figure 5.3. Leukocyte adhesion on glass & PDMS substrates. (a)-(d) False-colored fluorescent images showing adsorbed leukocytes (blue) on glass, slippery glass (SLIC), PDMS and slippery PDMS surfaces, respectively, after 1 hour incubation. (e)-(f) Plots showing lower leukocyte adhesion (i.e., lower surface coverage) on SLIC coating and slippery PDMS.

While a comprehensive study (on blood-material interactions with different proteins and blood cells at longer incubation times with a wide variety of chemistries and substrates) is needed to develop a thorough understanding of the influence of slipperiness, our results indicate that SLIC surfaces can reduce protein adsorption (i.e., fibrinogen) and blood cell (platelets &

leukocytes) adhesion. Furthermore, this demonstrates the potential of SLIC surfaces for reducing thrombosis and highlights their scope for practical blood-contacting devices.

5.7 Conclusions

In this study, building on our prior work, we investigated the interactions of blood components (i.e., fibrinogen, platelets & leukocytes) on slippery surfaces using glass and PDMS substrates. We imparted slipperiness on glass by covalently attaching PEG brushes on hydroxylated glass slides. We imparted slipperiness to PDMS by mixing PDMS with 50% silicone oil by weight to the PDMS base and curing agent mixture. We investigated blood-material interactions by studying fibrinogen adsorption and platelet & leukocyte adhesion using fluorescence microscopy. Based on our results, slippery surfaces demonstrate lower fibrinogen adsorption and platelet and leukocyte adhesion compared to non-slippery surfaces. Specifically, SLIC surfaces demonstrate significantly lower fibrinogen adsorption (99.5% lower surface coverage) and platelet and leukocyte adhesion (91.8% and 99.4% lower surface coverage, respectively) compared to untreated glass slides. SLIC surfaces also demonstrate lower fibrinogen adsorption (47% lower surface coverage) and platelet and leukocyte adhesion (86.2% and 97.5% lower surface coverage, respectively) compared to slippery PDMS. While a comprehensive study (on blood-material interactions with different proteins and blood cells at longer incubation times with a wide variety of chemistries and substrates) is needed to develop a thorough understanding of the influence of slipperiness, our results indicate that SLIC surfaces can reduce protein adsorption (i.e., fibrinogen) and blood cell (platelets & leukocytes) adhesion. We envision that our study will encourage more investigations on blood-material interactions on slippery surfaces for developing improved biomedical devices with reduced risk of thrombosis.

CHAPTER 6. CONCLUSIONS AND FUTURE WORK

6.1 Introduction

Slippery surfaces (i.e., surfaces that display high mobility with liquid droplets) have gained significant attention for their advantages in a wide variety of applications like self-cleaning, drag reduction, enhanced condensation, fouling resistance, biomedical implants etc.[1,5,104] This is because slippery surfaces enable easy droplet sliding (i.e., high droplet mobility) due to low surface adhesion, which is highly desirable in several applications in thermofluidic and biofluidic devices. Depending on the surface wettability (i.e., hydrophilicity or hydrophobicity), slippery surfaces can prove to be extremely beneficial in specific practical applications. Slippery surfaces can be broadly classified as: i) textured slippery surfaces, wherein the underlying substrate is rough (both surface texture and surface chemistry play a critical role in obtaining slipperiness); and ii) non-textured slippery surfaces, wherein the underlying substrate is non-textured (surface homogeneity plays a critical role in obtaining slipperiness).

In this dissertation, we discuss the design principles of textured and non-textured slippery surfaces and demonstrate their applications for several thermofluidic and biofluidic applications (i.e., lossless droplet manipulation, enhanced chemical shielding, enhanced condensation heat transfer and enhanced fouling resistance). While we demonstrated an excellent performance of slippery surfaces in multiple novel applications, we strongly believe that what we revealed is just the tip of the iceberg and there is yet a lot more to explore and exploit the slipperiness on solid surfaces to open new avenues in thermofluidic and biofluidic applications.

6.2 Textured slippery surfaces

Textured slippery surfaces can be broadly classified as: i) super-repellent surfaces, which use texture to trap pockets of gas or air at the solid surface and ii) lubricant-infused surfaces,

which use texture to trap pockets of a liquid, immiscible with the contacting liquids at the solid surface.[2,6] In the first part of our work, we utilized super-repellent surfaces and demonstrated two specific applications: i) on-demand, remote and lossless droplet manipulation for handling infectious biofluids in order to minimize the risk of exposure to healthcare workers and clinical laboratory personnel and ii) enhanced chemical shielding on soft robots to survive and function in corrosive and harsh liquid environments. We chose super-repellent surfaces because they offer ultra-low adhesion by minimizing solid-liquid contact and facilitate lossless droplet manipulation. In the first application, we developed biofluid manipulators by integrating thermo-responsive soft actuators with superomniphobic surfaces (i.e., surfaces that are extremely repellent to virtually all liquids) through a simple and versatile multi-layer design. Utilizing our biofluid manipulators, we demonstrate in-plane (simultaneous and sequential) transport and mixing of liquid droplets, as well as out-of-plane grip, transport, and release of liquid droplets. We also emphasized the practical utility of our biofluid manipulators by demonstrating on-demand, remote and lossless manipulation of biofluid droplets, including blood and virus replicons for colorimetric assays and blood coagulation assays. We envision that our biofluid manipulators will not only reduce manual operations and minimize exposure to infectious agents, but also pave the way for developing inexpensive, simple, and portable robotic systems, which can allow point-of-care operations, particularly in developing nations.

For the second application, we demonstrated enhanced chemical shielding on soft robots (gripper, fish, and jellyfish) in acids (sulfuric acid and nitric acid) and solvents (toluene and chloroform). We designed soft robots using pneumatic actuators and imparted superomniphobicity by spray coating with fluorinated silica particles. Using our superomniphobic coatings, we demonstrated enhanced protection for at least 1 hour in

concentrated sulfuric acid while the surface without superomniphobic coating displayed a visible surface damage in <5 minutes. We also developed superomniphobic soft robots and demonstrated the grasp and release of solid objects in sulfuric acid and swimming on and under sulfuric acid and nitric acid environments without any visible surface damage. Furthermore, we demonstrated the actuation of soft actuator with magnetic field and heat as stimulus in solvents like chloroform and toluene without any visible swelling. Based on our results, we envision that our work will inspire developing novel soft robots that can survive and function efficiently in harsh liquid environments (acids, bases, or solvents) for longer periods in multiple applications related to food processing, healthcare, and chemical industries.

In our work on super-repellent surfaces, even though we focused on lossless droplet manipulation and enhancing chemical shielding, there are a few other aspects that require attention to realize and/or improve these applications in practice. One common problem that super-repellent surfaces suffer from is durability. Durability is highly dependent on the specific application. For the applications we demonstrated here, more detailed studies are required for robustness of the superomniphobic coating on soft robots under liquid pressure, liquid drag, mechanical abrasion, substrate actuation cycles and in the presence of corrosive liquids and sunlight with time. Surface chemistry is another aspect that requires more investigation. Here, we developed superomniphobic coatings using long chain fluorocarbons, which are deemed to be carcinogenic and bioaccumulation. More studies in developing super-repellent coatings with environment-friendly alternatives like short chain fluorocarbons and hydrocarbons are necessary. More studies are required in improving the precision and speed of droplet manipulation using soft robots with superomniphobicity. More studies to understand the influence of superomniphobic coating on mixing kinetics and blood coagulation kinetics compared to

traditional surfaces are necessary in order to employ these coatings in practical colorimetric and blood-coagulation assays.

6.3 Non-textured slippery surfaces

Despite the appeal of textured slippery surfaces, they lose slipperiness due to damage of texture, depletion of air via dissolution or external pressure, or depletion of lubricant via evaporation or repeated use.[22,23,103-105] To circumvent these issues, non-textured, all-solid slippery surfaces have been developed by covalently grafting brushes to substrates (i.e., tethering oligomers or polymers to surfaces).[106,107] Nearly all non-textured, all-solid slippery surfaces are hydrophobic.[106-110] There are very few reports of non-textured, all-solid slippery hydrophilic surfaces,[3,111-113] and no studies systematically investigated or elucidated the design of such surfaces. In the second part of our work, we revealed the underlying design principles for fabricating an emerging class of non-textured, all-solid, slippery hydrophilic (SLIC) surfaces by minimizing surface inhomogeneity. We demonstrated that SLIC surfaces can be designed by covalently binding high surface energy brushes to smooth substrates, only at sufficiently high grafting densities, resulting in both physical and chemical homogeneity. Utilizing our SLIC surfaces, we demonstrated exceptional performance in condensation and fouling-resistance compared to conventional (i.e., non-slippery) hydrophilic surfaces and slippery hydrophobic surfaces. Based on our results, we believe that SLIC surfaces have the potential to positively transform the technological landscape of thermofluidic and biofluidic devices.

To demonstrate the practical relevance of slippery surfaces for blood-contacting medical devices, we investigated the interactions of blood components (i.e., fibrinogen, platelets & leukocytes) on slippery surfaces using glass and PDMS substrates. We imparted slipperiness on glass by covalently attaching PEG brushes on hydroxylated glass slides. We imparted

slipperiness to PDMS by mixing PDMS with 50% silicone oil by weight to the PDMS base and curing agent mixture. We investigated blood-material interactions by studying fibrinogen adsorption and platelet & leukocyte adhesion using fluorescence microscopy. Based on our results, slippery surfaces demonstrate lower fibrinogen adsorption and platelet and leukocyte adhesion compared to non-slippery surfaces. Specifically, SLIC surfaces demonstrate significantly lower fibrinogen adsorption (99.5% lower surface coverage) and platelet and leukocyte adhesion (91.8% and 99.4% lower surface coverage, respectively) compared to untreated glass slides. SLIC surfaces also demonstrate lower fibrinogen adsorption (47% lower surface coverage) and platelet and leukocyte adhesion (86.2% and 97.5% lower surface coverage, respectively) compared to slippery PDMS. While a comprehensive study (on blood-material interactions with different proteins and blood cells at longer incubation times with a wide variety of chemistries and substrates) is needed to develop a thorough understanding of the influence of slipperiness, our results indicate that SLIC surfaces can reduce protein adsorption (i.e., fibrinogen) and blood cell (platelets & leukocytes) adhesion. We envision that our study will encourage more investigations on blood-material interactions on slippery surfaces for developing improved biomedical devices with reduced risk of thrombosis.

Unlike super-repellent surfaces, SLIC surfaces are in the rudimentary stages of development in terms of underlying physics and applications and have a lot more space for exploration. This is because SLIC surfaces are challenging to fabricate. So far, slipperiness along with hydrophilicity was achieved only using PEG chemistry. It is still unclear if other hydrophilic chemistries can result in slipperiness. More studies for developing SLIC surfaces with chemistries other than PEG like ionic polymers, polymers consisting of thiol, amino or carboxylic groups are necessary. More studies for a thorough molecular level understanding on

water dynamics at PEG-water interface are necessary. More studies on investigating the degradation (change in wettability and slipperiness) of SLIC coatings with temperature, liquid drag, and sunlight are necessary to employ them for industrial applications in thermofluidics and biofluidics. More studies on understanding the blood-material interactions with slipperiness using whole blood and different blood proteins and blood cells (platelets, leukocytes etc.) for longer incubation times on different substrates are required. More studies on exploring SLIC surfaces for novel applications like open miniaturized lab-on-a-chip platforms are necessary to commercialize SLIC coatings for biological and biomedical assays.

REFERENCES

1 Zhang, P. & Lv, F. A review of the recent advances in superhydrophobic surfaces and the emerging energy-related applications. *Energy* **82**, 1068-1087 (2015).

2 Li, J., Ueda, E., Paulssen, D. & Levkin, P. A. Slippery lubricant-infused surfaces: properties and emerging applications. *Advanced Functional Materials* **29**, 1802317 (2019).

3 Cha, H. *et al.* Dropwise condensation on solid hydrophilic surfaces. *Science advances* **6**, eaax0746 (2020).

4 El Fil, B., Kini, G. & Garimella, S. A review of dropwise condensation: Theory, modeling, experiments, and applications. *International Journal of Heat and Mass Transfer* **160**, 120172 (2020).

5 Lee, C., Choi, C.-H. & Kim, C.-J. Superhydrophobic drag reduction in laminar flows: a critical review. *Experiments in Fluids* **57**, 1-20 (2016).

6 Kota, A. K., Kwon, G. & Tuteja, A. The design and applications of superomniphobic surfaces. *NPG Asia Materials* **6**, e109-e109 (2014).

7 Manivasagam, V. K., Sabino, R. M., Kantam, P. & Popat, K. C. Surface modification strategies to improve titanium hemocompatibility: A comprehensive review. *Materials Advances* **2**, 5824-5842 (2021).

8 Movafaghi, S. *et al.* Hemocompatibility of super-repellent surfaces: current and future. *Materials horizons* **6**, 1596-1610 (2019).

9 Young, T. III. An essay on the cohesion of fluids. *Philosophical transactions of the royal society of London*, 65-87 (1805).

10 Wenzel, R. N. Resistance of solid surfaces to wetting by water. *Industrial & Engineering Chemistry* **28**, 988-994 (1936).

11 Cassie, A. & Baxter, S. Wettability of porous surfaces. *Transactions of the Faraday society* **40**, 546-551 (1944).

12 Wang, W. *et al.* Metamorphic superomniphobic surfaces. *Adv. Mater.* **29**, 1700295 (2017).

13 Dettre, R. H. & Johnson Jr, R. E. (ACS Publications, 1964).

14 Johnson Jr, R. E. & Dettre, R. H. (ACS Publications, 1964).

15 Eral, H. B., 't Mannetje, D. & Oh, J. M. Contact angle hysteresis: a review of fundamentals and applications. *Colloid and polymer science* **291**, 247-260 (2013).

16 Extrand, C. A thermodynamic model for contact angle hysteresis. *Journal of Colloid and interface Science* **207**, 11-19 (1998).

17 Makkonen, L. A thermodynamic model of contact angle hysteresis. *The Journal of chemical physics* **147**, 064703 (2017).

18 Furmidge, C. Studies at phase interfaces. I. The sliding of liquid drops on solid surfaces and a theory for spray retention. *Journal of colloid science* **17**, 309-324 (1962).

19 Hamrock, B. J., Schmid, S. R. & Jacobson, B. O. *Fundamentals of fluid film lubrication*. (CRC press, 2004).

20 Tuteja, A. *et al.* Designing superoleophobic surfaces. *Science* **318**, 1618-1622 (2007).

21 Epstein, A. K., Wong, T.-S., Belisle, R. A., Boggs, E. M. & Aizenberg, J. Liquid-infused structured surfaces with exceptional anti-biofouling performance. *Proceedings of the National Academy of Sciences* **109**, 13182-13187 (2012).

22 Tian, X., Verho, T. & Ras, R. H. Moving superhydrophobic surfaces toward real-world applications. *Science* **352**, 142-143 (2016).

23 Peppou-Chapman, S., Hong, J. K., Waterhouse, A. & Neto, C. Life and death of liquid-infused surfaces: a review on the choice, analysis and fate of the infused liquid layer. *Chemical Society Reviews* **49**, 3688-3715 (2020).

24 Weinstein, R. A. & Singh, K. Laboratory-acquired infections. *Clin. Infect. Dis.* **49**, 142-147 (2009).

25 Sewell, D. L. Laboratory-associated infections and biosafety. *Clin. Microbiol. Rev.* **8**, 389-405 (1995).

26 Nienhaus, A., Kesavachandran, C., Wendeler, D., Haamann, F. & Dulon, M. Infectious diseases in healthcare workers–an analysis of the standardised data set of a German compensation board. *J. Occup. Med. Toxicol.* **7**, 8 (2012).

27 Pike, R. M. Laboratory-associated infections: incidence, fatalities, causes, and prevention. *Annu. Rev. Microbiol.* **33**, 41-66 (1979).

28 Organization, W. H. Health care-associated infections fact sheet. *World Health Organization* **4** (2015).

29 Haque, M., Sartelli, M., McKimm, J. & Bakar, M. A. Health care-associated infections–an overview. *Infection and drug resistance* **11**, 2321 (2018).

30 Miller, K. W. *et al.* A Semi-Automated Tuberculosis Testing Workflow Reduces Manual Hazardous Sample Handling and Hands-On Time: A Proof-of-Concept Study. *SLAS Technol.*, 2472630319884519 (2019).

31 Ince, J. & McNally, A. Development of rapid, automated diagnostics for infectious disease: advances and challenges. *Expert Rev. Med. Devices* **6**, 641-651 (2009).

32 Rus, D. & Tolley, M. T. Design, fabrication and control of soft robots. *Nature* **521**, 467-475 (2015).

33 Wang, H., Totaro, M. & Beccai, L. Toward perceptive soft robots: Progress and challenges. *Advanced Science* **5**, 1800541 (2018).

34 Gossweiler, G. R. *et al.* Mechanochemically active soft robots. *ACS applied materials & interfaces* **7**, 22431-22435 (2015).

35 Sun, L. *et al.* Bioinspired programmable wettability arrays for droplets manipulation. *Proceedings of the National Academy of Sciences* **117**, 4527-4532 (2020).

36 Liu, C., Sun, Y., Huanng, J., Guo, Z. & Liu, W. External-field-induced directional droplet transport: A review. *Advances in Colloid and Interface Science* **295**, 102502 (2021).

37 Feng, W., Ueda, E. & Levkin, P. A. Droplet Microarrays: From Surface Patterning to High-Throughput Applications. *Advanced materials* **30**, 1706111 (2018).

38 Malinowski, R., Parkin, I. P. & Volpe, G. Advances towards programmable droplet transport on solid surfaces and its applications. *Chemical Society Reviews* **49**, 7879-7892 (2020).

39 Movafaghi, S. *et al.* Tunable superomniphobic surfaces for sorting droplets by surface tension. *Lab on a Chip* **16**, 3204-3209 (2016).

40 Zhu, L., Shao, C., Chen, H., Chen, Z. & Zhao, Y. Hierarchical Hydrogels with Ordered Micro-Nano Structures for Cancer-on-a-Chip Construction. *Research* **2021** (2021).

41 Baudoin, M. & Thomas, J.-L. Acoustic tweezers for particle and fluid micromanipulation. *Annual Review of Fluid Mechanics* **52**, 205-234 (2020).

42 Lee, J. & Kim, C.-J. Surface-tension-driven microactuation based on continuous electrowetting. *Journal of Microelectromechanical Systems* **9**, 171-180 (2000).

43 Li, Q. *et al.* Reversible structure engineering of bioinspired anisotropic surface for droplet recognition and transportation. *Advanced Science* **7**, 2001650 (2020).

44 Lin, Y. *et al.* Magnetically induced low adhesive direction of nano/micropillar arrays for microdroplet transport. *Advanced Functional Materials* **28**, 1800163 (2018).

45 Timonen, J. V., Latikka, M., Leibler, L., Ras, R. H. & Ikkala, O. Switchable static and dynamic self-assembly of magnetic droplets on superhydrophobic surfaces. *Science* **341**, 253-257 (2013).

46 Kwon, G. *et al.* Visible light guided manipulation of liquid wettability on photoresponsive surfaces. *Nature Communications* **8**, 14968 (2017).

47 Kavokine, N. *et al.* Light-Driven Transport of a Liquid Marble with and against Surface Flows. *Angewandte Chemie International Edition* **55**, 11183-11187 (2016).

48 Huang, S. *et al.* Directional transport of droplets on wettability patterns at high temperature. *Applied Surface Science* **428**, 432-438 (2018).

49 Ozcelik, A. *et al.* Acoustic tweezers for the life sciences. *Nature methods* **15**, 1021-1028 (2018).

50 Haines, C. S. *et al.* New twist on artificial muscles. *Proc. Natl. Acad. Sci. U.S.A.* **113**, 11709-11716 (2016).

51 Haines, C. S. *et al.* Artificial muscles from fishing line and sewing thread. *Science* **343**, 868-872 (2014).

52 Abbas, A. & Zhao, J. in *2017 IEEE International Conference on Robotics and Automation (ICRA).* 6121-6126 (IEEE).

53 Huang, X. *et al.* Highly Dynamic Shape Memory Alloy Actuator for Fast Moving Soft Robots. *Adv. Mater. Technol.*, 1800540 (2019).

54 Trivedi, D., Rahn, C. D., Kier, W. M. & Walker, I. D. Soft robotics: Biological inspiration, state of the art, and future research. *Appl. Bionics Biomech.* **5**, 99-117 (2008).

55 Marchese, A. D., Katzschmann, R. K. & Rus, D. A recipe for soft fluidic elastomer robots. *Soft Robot.* **2**, 7-25 (2015).

56 Wang, J. *et al.* Programmable wettability on photocontrolled graphene film. *Science Advances* **4**, eaat7392 (2018).

57 Zhang, H. *et al.* Microfluidic printing of slippery textiles for medical drainage around wounds. *Advanced Science* **7**, 2000789 (2020).

58 Lafuma, A. & Quéré, D. Superhydrophobic states. *Nat. Mater.* **2**, 457-460 (2003).

59 Pan, S., Kota, A. K., Mabry, J. M. & Tuteja, A. Superomniphobic surfaces for effective chemical shielding. *J. Am. Chem. Soc.* **135**, 578-581 (2012).

60 Vahabi, H., Wang, W., Mabry, J. M. & Kota, A. K. Coalescence-induced jumping of droplets on superomniphobic surfaces with macrotexture. *Sci. Adv.* **4**, eaau3488 (2018).

61 Deng, X., Mammen, L., Butt, H.-J. & Vollmer, D. Candle soot as a template for a transparent robust superamphiphobic coating. *Science* **335**, 67-70 (2012).

62 Su, B., Tian, Y. & Jiang, L. Bioinspired interfaces with superwettability: from materials to chemistry. *J. Am. Chem. Soc.* **138**, 1727-1748 (2016).

63 Darmanin, T. & Guittard, F. Superhydrophobic and superoleophobic properties in nature. *Mater. Today* **18**, 273-285 (2015).

64 Yong, J., Chen, F., Yang, Q., Huo, J. & Hou, X. Superoleophobic surfaces. *Chem. Soc. Rev.* **46**, 4168-4217 (2017).

65 Chu, Z. & Seeger, S. Superamphiphobic surfaces. *Chem. Soc. Rev.* **43**, 2784-2798 (2014).

66 Fayzulin, R., Scholle, F., Petrakova, O., Frolov, I. & Mason, P. W. Evaluation of replicative capacity and genetic stability of West Nile virus replicons using highly efficient packaging cell lines. *Virology* **351**, 196-209 (2006).

67 Widman, D. G. *et al.* RepliVAX WN, a single-cycle flavivirus vaccine to prevent West Nile disease, elicits durable protective immunity in hamsters. *Vaccine* **27**, 5550-5553 (2009).

68 Brown, E. *et al.* Universal robotic gripper based on the jamming of granular material. *Proc. Natl. Acad. Sci. U.S.A.* **107**, 18809-18814 (2010).

69 Shintake, J., Cacucciolo, V., Floreano, D. & Shea, H. Soft Robotic Grippers. *Adv. Mater.* **30**, 1707035 (2018).

70 Sapan, C. V., Lundblad, R. L. & Price, N. C. Colorimetric protein assay techniques. *Biotechnology and applied Biochemistry* **29**, 99-108 (1999).

71 Kruger, N. J. The Bradford method for protein quantitation. *The protein protocols handbook*, 17-24 (2009).

72 Compton, S. J. & Jones, C. G. Mechanism of dye response and interference in the Bradford protein assay. *Analytical biochemistry* **151**, 369-374 (1985).

73 Göbel, K. *et al.* The coagulation factors fibrinogen, thrombin, and factor XII in inflammatory disorders—a systematic review. *Frontiers in immunology* **9**, 1731 (2018).

74 Kawase, T., Okuda, K., Wolff, L. F. & Yoshie, H. Platelet-rich plasma-derived fibrin clot formation stimulates collagen synthesis in periodontal ligament and osteoblastic cells in vitro. *Journal of periodontology* **74**, 858-864 (2003).

75 Gubala, V., Harris, L. F., Ricco, A. J., Tan, M. X. & Williams, D. E. Point of care diagnostics: status and future. *Analytical chemistry* **84**, 487-515 (2012).

76 Cianchetti, M., Laschi, C., Menciassi, A. & Dario, P. Biomedical applications of soft robotics. *Nature Reviews Materials* **3**, 143-153 (2018).

77 Fernando, Y., Mathath, A. & Murshid, M. A. Improving productivity: A review of robotic applications in food industry. *International Journal of Robotics Applications and Technologies (IJRAT)* **4**, 43-62 (2016).

78 Hall, A. K. *et al.* Acceptance and perceived usefulness of robots to assist with activities of daily living and healthcare tasks. *Assistive Technology* **31**, 133-140 (2019).

79 Chowdhary, G., Gazzola, M., Krishnan, G., Soman, C. & Lovell, S. Soft robotics as an enabling technology for agroforestry practice and research. *Sustainability* **11**, 6751 (2019).

80 Majidi, C. Soft robotics: a perspective—current trends and prospects for the future. *Soft robotics* **1**, 5-11 (2014).

81 Sitti, M. Miniature soft robots—road to the clinic. *Nature Reviews Materials* **3**, 74-75 (2018).

82 Chi, Y. *et al.* Bistable and multistable actuators for soft robots: Structures, materials, and functionalities. *Advanced Materials* **34**, 2110384 (2022).

83 El-Atab, N. *et al.* Soft actuators for soft robotic applications: a review. *Advanced Intelligent Systems* **2**, 2000128 (2020).

84 Ebrahimi, N. *et al.* Magnetic actuation methods in bio/soft robotics. *Advanced Functional Materials* **31**, 2005137 (2021).

85 Yu, K. *et al.* Robust Jumping Actuator with a Shrimp-Shell Architecture. *Advanced Materials* **33**, 2104558 (2021).

86 Kappert, E. J. *et al.* Swelling of 9 polymers commonly employed for solvent-resistant nanofiltration membranes: A comprehensive dataset. *Journal of membrane science* **569**, 177-199 (2019).

87 Abu-Abdeen, M. & Elamer, I. Mechanical and swelling properties of thermoplastic elastomer blends. *Materials & Design* **31**, 808-815 (2010).

88 Brook, M. A. New control over silicone synthesis using sih chemistry: the piers–rubinsztajn reaction. *Chemistry–A European Journal* **24**, 8458-8469 (2018).

89 Wang, W. *et al.* On-demand, remote and lossless manipulation of biofluid droplets. *Materials Horizons* **9**, 2863-2871 (2022).

90 Movafaghi, S. *et al.* Superomniphobic Papers for On-Paper pH Sensors. *Advanced Materials Interfaces* **6**, 1900232 (2019).

91 Chi, Y., Tang, Y., Liu, H. & Yin, J. Leveraging monostable and bistable pre-curved bilayer actuators for high-performance multitask soft robots. *Advanced Materials Technologies* **5**, 2000370 (2020).

92 Zhao, Y. *et al.* Twisting for soft intelligent autonomous robot in unstructured environments. *Proceedings of the National Academy of Sciences* **119**, e2200265119 (2022).

93 Jiang, H., Li, C. & Huang, X. Actuators based on liquid crystalline elastomer materials. *Nanoscale* **5**, 5225-5240 (2013).

94 Chen, Y., Lu, K. J. & Chung, T.-S. An omniphobic slippery membrane with simultaneous anti-wetting and anti-scaling properties for robust membrane distillation. *Journal of Membrane Science* **595**, 117572 (2020).

95 Lu, K. J., Zhao, D., Chen, Y., Chang, J. & Chung, T.-S. Rheologically controlled design of nature-inspired superhydrophobic and self-cleaning membranes for clean water production. *NPJ Clean Water* **3**, 1-10 (2020).

96 Lu, K.-J., Liang, C. Z., Chen, Y. & Chung, T.-S. Unlock the secret of air blowing in developing high strength and superhydrophobic membranes for membrane distillation. *Desalination* **527**, 115579 (2022).

97 Vallabhuneni, S., Movafaghi, S., Wang, W. & Kota, A. K. Superhydrophobic coatings for improved performance of electrical insulators. *Macromolecular Materials and Engineering* **303**, 1800313 (2018).

98 Wang, W., Vahabi, H., Movafaghi, S. & Kota, A. K. Superomniphobic surfaces with improved mechanical durability: Synergy of hierarchical texture and mechanical interlocking. *Advanced materials interfaces* **6**, 1900538 (2019).

99 Vahabi, H. *et al.* Metallic superhydrophobic surfaces via thermal sensitization. *Applied Physics Letters* **110**, 251602 (2017).

100 Rothstein, J. P. Slip on superhydrophobic surfaces. *Annual review of fluid mechanics* **42**, 89-109 (2010).

101 Irajizad, P., Hasnain, M., Farokhnia, N., Sajadi, S. M. & Ghasemi, H. Magnetic slippery extreme icephobic surfaces. *Nature communications* **7**, 1-7 (2016).

102 Solomon, B. R., Khalil, K. S. & Varanasi, K. K. Drag reduction using lubricant-impregnated surfaces in viscous laminar flow. *Langmuir* **30**, 10970-10976 (2014).

103 Hoque, M. J. *et al.* Life Span of Slippery Lubricant Infused Surfaces. *ACS Applied Materials & Interfaces* (2022).

104 Sett, S. *et al.* Lubricant-Infused Surfaces for Low-Surface-Tension Fluids: The Extent of Lubricant Miscibility. *ACS Applied Materials & Interfaces* **13**, 23121-23133 (2021).

105 Ma, J., Sett, S., Cha, H., Yan, X. & Miljkovic, N. Recent developments, challenges, and pathways to stable dropwise condensation: a perspective. *Applied Physics Letters* **116**, 260501 (2020).

106 Buddingh, J. V., Hozumi, A. & Liu, G. Liquid and liquid-like surfaces/coatings that readily slide fluids. *Progress in Polymer Science* **123**, 101468 (2021).

107 Wang, L. & McCarthy, T. J. Covalently attached liquids: instant omniphobic surfaces with unprecedented repellency. *Angewandte Chemie International Edition* **55**, 244-248 (2016).

108 Wang, X., Wang, Z., Heng, L. & Jiang, L. Stable omniphobic anisotropic covalently grafted slippery surfaces for directional transportation of drops and bubbles. *Advanced Functional Materials* **30**, 1902686 (2020).

109 Zhao, H. *et al.* Extreme antiscaling performance of slippery omniphobic covalently attached liquids. *ACS Applied Materials & Interfaces* **12**, 12054-12067 (2020).

110 Zhao, H. *et al.* Scalable slippery omniphobic covalently attached liquid coatings for flow fouling reduction. *ACS Applied Materials & Interfaces* **13**, 38666-38679 (2021).

111 Nakamura, S., Archer, R. J., Dunderdale, G. J. & Hozumi, A. Perfluorinated compounds are not necessary: pegylated organosilanes can endow good water sliding/removal properties. *Journal of Hazardous Materials* **398**, 122625 (2020).

112 Becher-Nienhaus, B., Liu, G., Archer, R. J. & Hozumi, A. Surprising Lack of Influence on Water Droplet Motion by Hydrophilic Microdomains on Checkerboard-like Surfaces with Matched Contact Angle Hysteresis. *Langmuir* **36**, 7835-7843 (2020).

113 Papra, A., Gadegaard, N. & Larsen, N. B. Characterization of ultrathin poly (ethylene glycol) monolayers on silicon substrates. *Langmuir* **17**, 1457-1460 (2001).

114 Rubinstein, M. & Colby, R. H. *Polymer physics*. Vol. 23 (Oxford university press New York, 2003).

115 Ulman, A. Formation and structure of self-assembled monolayers. *Chemical reviews* **96**, 1533-1554 (1996).

116 Ho, T. A., Papavassiliou, D. V., Lee, L. L. & Striolo, A. Liquid water can slip on a hydrophilic surface. *Proceedings of the National Academy of Sciences* **108**, 16170-16175 (2011).

117 Ma, L., Gaisinskaya-Kipnis, A., Kampf, N. & Klein, J. Origins of hydration lubrication. *Nature communications* **6**, 1-6 (2015).

118 Pertsin, A. J. & Grunze, M. Computer simulation of water near the surface of oligo (ethylene glycol)-terminated alkanethiol self-assembled monolayers. *Langmuir* **16**, 8829-8841 (2000).

119 Brzoska, J., Azouz, I. B. & Rondelez, F. Silanization of solid substrates: a step toward reproducibility. *Langmuir* **10**, 4367-4373 (1994).

120 Ho, J. Y. *et al.* Opportunities in Nanoengineered Surface Designs for Enhanced Condensation Heat and Mass Transfer. *Journal of Heat Transfer* (2022).

121 Jeon, S., Lee, J., Andrade, J. & De Gennes, P. Protein—surface interactions in the presence of polyethylene oxide: I. Simplified theory. *Journal of colloid and interface science* **142**, 149-158 (1991).

122 Sayin, M., Nefedov, A. & Zharnikov, M. Interaction of water with oligo (ethylene glycol) terminated monolayers: wetting versus hydration. *Physical Chemistry Chemical Physics* **22**, 8088-8095 (2020).

123 Hedayati, M., Krapf, D. & Kipper, M. J. Dynamics of long-term protein aggregation on low-fouling surfaces. *Journal of Colloid and Interface Science* **589**, 356-366 (2021).

124 Hedayati, M., Kipper, M. J. & Krapf, D. Anomalous protein kinetics on low-fouling surfaces. *Physical Chemistry Chemical Physics* **22**, 5264-5271 (2020).

125 Wörz, A., Berchtold, B., Moosmann, K., Prucker, O. & Rühe, J. Protein-resistant polymer surfaces. *Journal of Materials Chemistry* **22**, 19547-19561 (2012).

126 Chen, S., Li, L., Zhao, C. & Zheng, J. Surface hydration: Principles and applications toward low-fouling/nonfouling biomaterials. *Polymer* **51**, 5283-5293 (2010).

127 Ham, H. O. *et al.* A rechargeable anti-thrombotic coating for blood-contacting devices. *Biomaterials* **276**, 121011 (2021).

128 Hong, J. K., Ruhoff, A. M., Mathur, K., Neto, C. & Waterhouse, A. Mechanisms for Reduced Fibrin Clot Formation on Liquid-Infused Surfaces. *Advanced Healthcare Materials* **11**, 2201360 (2022).

129 Hong, J. K. *et al.* Design Optimization of Perfluorinated Liquid-Infused Surfaces for Blood-Contacting Applications. *Advanced Materials Interfaces* **9**, 2102214 (2022).

130 Zhang, M. *et al.* Anti-thrombogenic surface coatings for extracorporeal membrane oxygenation: a narrative review. *ACS Biomaterials Science & Engineering* **7**, 4402-4419 (2021).

131 Mackie, G., Gao, L., Yau, S., Leslie, D. C. & Waterhouse, A. Clinical potential of immobilized liquid interfaces: perspectives on biological interactions. *Trends in biotechnology* **37**, 268-280 (2019).

132 Damodaran, V. B. & Murthy, N. S. Bio-inspired strategies for designing antifouling biomaterials. *Biomaterials research* **20**, 1-11 (2016).

133 Anderson, J. M., Rodriguez, A. & Chang, D. T. in *Seminars in immunology.* 86-100 (Elsevier).

134 Gorbet, M. B. & Sefton, M. V. Biomaterial-associated thrombosis: roles of coagulation factors, complement, platelets and leukocytes. *Biomaterials* **25**, 5681-5703 (2004).

135 Jaffer, I., Fredenburgh, J., Hirsh, J. & Weitz, J. Medical device-induced thrombosis: what causes it and how can we prevent it? *Journal of Thrombosis and Haemostasis* **13**, S72-S81 (2015).

136 Manivasagam, V. K. & Popat, K. C. In vitro investigation of hemocompatibility of hydrothermally treated titanium and titanium alloy surfaces. *ACS omega* **5**, 8108-8120 (2020).

137 Vahabi, H. *et al.* Designing non-textured, all-solid, slippery hydrophilic surfaces. *Matter* **5**, 4502-4512 (2022).

138 Hong, J. K. *et al.* Evaluating medical device and material thrombosis under flow: current and emerging technologies. *Biomaterials Science* **8**, 5824-5845 (2020).

139 Gbyli, R., Mercaldi, A., Sundaram, H. & Amoako, K. A. Achieving totally local anticoagulation on blood contacting devices. *Advanced Materials Interfaces* **5**, 1700954 (2018).

140 Labarrere, C. A., Dabiri, A. E. & Kassab, G. S. Thrombogenic and inflammatory reactions to biomaterials in medical devices. *Frontiers in Bioengineering and biotechnology* **8**, 123 (2020).

141 Metharom, P., Berndt, M. C., Baker, R. I. & Andrews, R. K. Current state and novel approaches of antiplatelet therapy. *Arteriosclerosis, thrombosis, and vascular biology* **35**, 1327-1338 (2015).

142 Michelson, A. D. Antiplatelet therapies for the treatment of cardiovascular disease. *Nature Reviews Drug Discovery* **9**, 154-169 (2010).

143 Wahl, W. L., Brandt, M.-M., Thompson, B. G., Taheri, P. A. & Greenfield, L. J. Antiplatelet therapy: an alternative to heparin for blunt carotid injury. *Journal of Trauma and Acute Care Surgery* **52**, 896-901 (2002).

144 Price, M. J. Bedside evaluation of thienopyridine antiplatelet therapy. *Circulation* **119**, 2625-2632 (2009).

145 Popma, J. J. *et al.* Antithrombotic therapy during percutaneous coronary intervention: the Seventh ACCP Conference on Antithrombotic and Thrombolytic Therapy. *Chest* **126**, 576S-599S (2004).

146 Nathan, A. S., Sen, S. & Yeh, R. W. The risk of bleeding with the use of antiplatelet agents for the treatment of cardiovascular disease. *Expert Opinion on Drug Safety* **16**, 561-572 (2017).

147 Andrade, J. G. *et al.* Risk of bleeding on triple antithrombotic therapy after percutaneous coronary intervention/stenting: a systematic review and meta-analysis. *Canadian Journal of Cardiology* **29**, 204-212 (2013).

148 Mikhailidis, D. & Ganotakis, E. Plasma albumin and platelet function: relevance to atherogenesis and thrombosis. *Platelets* **7**, 125-137 (1996).

149 Mulvihill, J. N., Faradji, A., Oberling, F. & Cazenave, J. P. Surface passivation by human albumin of plasmaperesis circuits reduces platelet accumulation and thrombus formation. Experimental and clinical studies. *Journal of biomedical materials research* **24**, 155-163 (1990).

150 Zucker, M. & Nachmias, V. Platelet activation. *Arteriosclerosis: An Official Journal of the American Heart Association, Inc.* **5**, 2-18 (1985).

151 Aslan, J. E. Platelet shape change. *Platelets in thrombotic and non-thrombotic disorders: Pathophysiology, pharmacology and therapeutics: An update*, 321-336 (2017).

152 Ni, H. & Freedman, J. Platelets in hemostasis and thrombosis: role of integrins and their ligands. *Transfusion and Apheresis Science* **28**, 257-264 (2003).

153 Kim, D. A., Ashworth, K. J., Di Paola, J. & Ku, D. N. Platelet α-granules are required for occlusive high-shear-rate thrombosis. *Blood advances* **4**, 3258-3267 (2020).

154 Guy, R. D., Fogelson, A. L. & Keener, J. P. Fibrin gel formation in a shear flow. *Mathematical Medicine and Biology* **24**, 111-130 (2007).

155 Weisel, J. W. & Litvinov, R. I. Fibrin formation, structure and properties. *Fibrous proteins: structures and mechanisms*, 405-456 (2017).

156 Kimball, A. S., Obi, A. T., Diaz, J. A. & Henke, P. K. The emerging role of NETs in venous thrombosis and immunothrombosis. *Frontiers in immunology* **7**, 236 (2016).

157 Martinod, K. & Wagner, D. D. Thrombosis: tangled up in NETs. *Blood, The Journal of the American Society of Hematology* **123**, 2768-2776 (2014).

158 Joseph, L., Fink, L. & Hauer-Jensen, M. Cytokines in coagulation and thrombosis: a preclinical and clinical review. *Blood coagulation & fibrinolysis* **13**, 105-116 (2002).

159 Esmon, C. T. Molecular circuits in thrombosis and inflammation. *Thrombosis and haemostasis* **109**, 416-420 (2013).

160 Barrientos, S., Stojadinovic, O., Golinko, M. S., Brem, H. & Tomic-Canic, M. Growth factors and cytokines in wound healing. *Wound repair and regeneration* **16**, 585-601 (2008).

161 Oppenheim, J. J. Cytokines: past, present, and future. *International journal of hematology* **74**, 3-8 (2001).